Doctoral Dissertation

博士論文

History of the great Kanto earthquakes deduced from the Holocene marine terraces:
Development and application of new quantitative methods for
the geological and geomorphological analyses
（完新世海岸段丘を用いた関東地震発生履歴の解明：
地形学・地質学的データへの新たな定量的解析手法の開発と応用）

A Dissertation Submitted for the Degree of Doctor of Philosophy
December 2020

令和２年１２月博士（理学）申請

Department of Earth and Planetary Science,
The University of Tokyo

東京大学理学系研究科地球惑星科学専攻

Junki Komori

小森　純希

Abstract

I reevaluated recurrence history of the Kanto earthquakes in the past 7,000 years, which are the subduction earthquakes along the Sagami Trough, central Japan, by reinvestigating middle to late Holocene uplifted marine terraces in the southernmost part of the Boso Peninsula, named Numa terraces. Previous paleoseismological studies have interpreted the Numa terraces to be uplifted due to the largest type of earthquake along the Sagami Trough, named Genroku-type earthquakes. However, long-term crustal deformation process has not been sufficiently examined by kinematically or mechanically supported methods, and thus rupture patterns of the past Kanto earthquakes is unclear.

In this study, I first reinvestigated present distributions and formation ages of the Numa terraces by new quantitative analysis methods for geomorphological and geological surveys. The geomorphological investigation provided objective and quantitative elevation distributions of the Numa terraces by statistical detection and classification methods using 0.5-m-grid digital elevation model. We also applied Bayesian method to radiocarbon dating analysis via geological investigations to estimate the terrace formation ages with well-constrained confidence intervals. The newly compiled comprehensive sediment age dataset of the Numa terraces improved the reliability of the estimation. Results of geomorphological and geological investigations calibrated with my statistical analyses revealed that the Numa terraces have similar relative height distributions up to 7 m and different formation interval times from 1,300 to 2,500 years.

Furthermore, I developed a mechanical model for the plate subduction and earthquake recurrence to relate the present marine terrace heights to the past Kanto earthquakes. This model reproduces long-term deformation due to plate subduction by adopting a mechanical boundary condition on the plate interface. I proposed a rupture scenario of the Kanto earthquakes in the past 7,000 years to reproduce the present distributions of the Numa terraces. This model was also consistent with the previous results of geological and geodetic studies outside of this study region.

This study constructed a mechanically supported scenario for the formation of the uplifted marine terrace sequence due to the subduction earthquakes for the first time, which has been opposed by the previous models employing kinematic boundary conditions. The proposed rupture scenario in this study indicated that the Numa terraces, which have been regarded to be formed due to similar Genroku-type earthquakes, were likely formed due to the different source earthquakes and that the Kanto earthquakes possibly had more variability than the previous assumption.

i

Contents

Abbreviations

AMS .... Accelerator Mass Spectrometry

BSM .... Back-Slip Model

DEM .... Digital Elevation Model

ESPM .... Elastic Subducting Plate Model

GNSS .... Global Navigation Satellite System

LiDAR .... Laser Imaging Detection and Ranging

MCMC .... Markov Chain Monte Carlo

PDF .... Probability Density Function

PHS .... Philippine Sea Plate

yBP .... years before present

1. Introduction

The recurrence pattern of the earthquake is one of the most important issues that seismology is dealing with. Specifically, the large earthquakes of Mw 7–9 that severely affect human society have a lower frequency of once every a hundred to a thousand years, which is beyond the range of instrumental measurement. Therefore, the paleoseismological study has been developed to estimate the occurrence history of the past large earthquakes by investigating the historical and archaeological records, coastal sediments (tsunami deposits), and the tectonic landforms. The early paleoseismological studies had often proposed that the large earthquakes periodically occur as 'characteristic earthquakes.' However, many recent studies indicate the complexity of the mechanisms of the earthquake recurrences. In conventional studies, an oversimplified extrapolation of the recent observations is often seen, possibly affected by a small number of geological and geomorphological datasets, leading to less objective estimation of the occurrence age and the source area. Moreover, previous paleoseismological studies are not always verified with kinematic or mechanical models. Paleoseismological studies can be updated to discuss the occurrence pattern more objectively with quantitative and statistical methods for the geological and geomorphological surveys and kinematic verification. This study aims to eliminate the subjectivity in estimating the earthquake recurrence, targeting the M8 class interplate earthquakes that occur along the Sagami Trough subduction zone (the Kanto earthquakes) by a comprehensive study of geological and geomorphological re-investigations and the rupture scenario constructed with a mechanical plate subduction model.

1.1 Review of the Kanto earthquakes

The Sagami Trough marks the plate margin where the Philippine Sea Plate (PHS) subducts northwestward beneath the continental plate of northeast Japan (Figure 1-1a). Historical documents record two interplate earthquakes, the 1703 M8.2 Genroku Kanto earthquake and the 1923 M7.9 Taisho Kanto earthquake (hereafter, the 1703 Genroku earthquake and the 1923 Taisho earthquake, respectively), there and accompanied coastal uplifts (Usami et al., 2013). Such Sagami Trough subduction earthquakes, named the Kanto earthquakes, are anticipated to cause devastating damage to the adjacent region, including the Tokyo metropolitan area, in the future. Thus, they are subjected to scientific
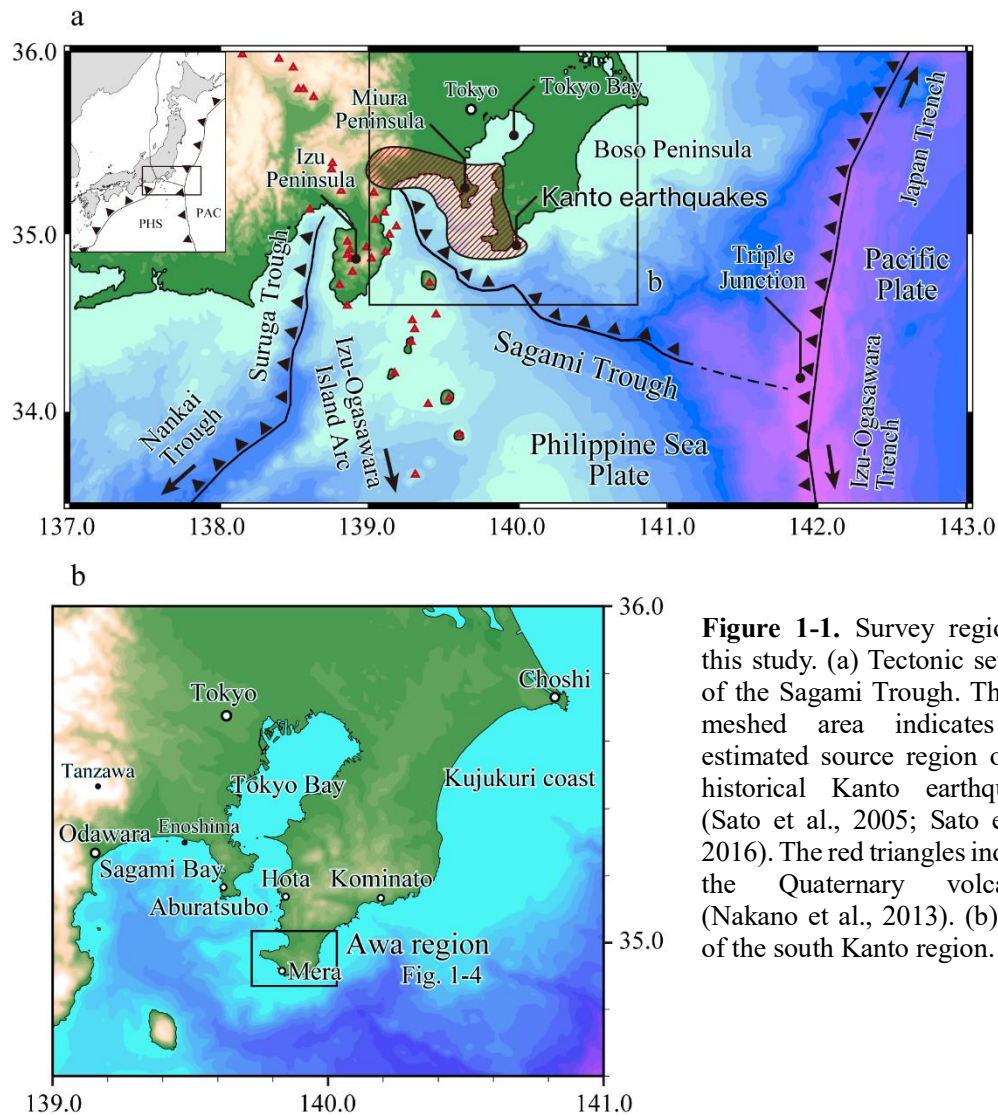
Figure 1-1. Survey region of this study. (a) Tectonic settings of the Sagami Trough. The red meshed area indicates the estimated source region of the historical Kanto earthquakes (Sato et al., 2005; Sato et al., 2016). The red triangles indicate the Quaternary volcanoes (Nakano et al., 2013). (b) Map of the south Kanto region.

investigations and future hazard assessment. Besides the historical documents, the geological investigations have revealed the coastal tectonic landforms and sediments that imply the prehistoric Kanto earthquake events. The previous surveys have estimated the recurrent patterns of the Kanto earthquakes and evaluated the future hazards by extrapolating these datasets via the empirical assessment of earthquake recurrence. However, the previous studies have still contained several open questions, and thus further comprehensive understanding of the history of the past Sagami Trough event is required.

1.1.1 1923 Taisho Kanto earthquake

The latest large (>M7) subduction earthquake along the Sagami Trough occurred on Sep. 1, 1923, called the Taisho earthquake, named after the era name at the time. The
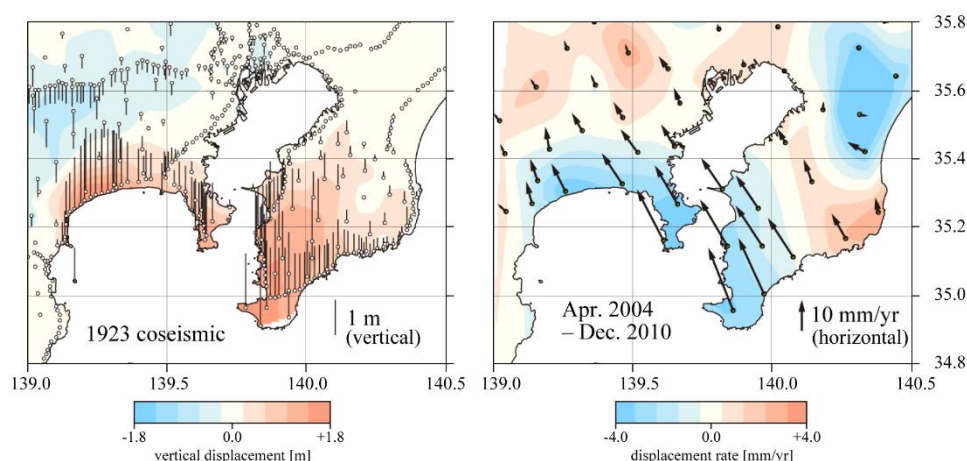
Figure 1-2. Surface displacements in the south Kanto region observed by geodetic measurements. (a) Coseismic vertical displacement due to the 1923 Taisho earthquake deduced by the campaign leveling surveys by Land survey department (1926; 1930) (Miyabe, 1931). Circles are the observation points. (b) Present surface deformation rate observed by the continuous GNSS measurement. The arrows indicate the horizontal displacements. The color contour is the interpolated vertical displacement distribution.

casualties of this event are more than 105,000, which is the worst record among the natural disasters in Japan's history (Usami et al., 2013). Thanks to the modernized observation since the few decades before the event, the early instruments recorded various seismic and tectonic phenomena of this event and revealed characteristics of the coseismic rupture.

The geodetic measurements recorded significant crustal movements due to the 1923 Taisho earthquake. The land survey department (1926; 1930) (predecessor of Geospatial Information Authority of Japan (GSI)) was conducting a campaign leveling survey of benchmarks and triangular points. Before and after the 1923 event, the re-leveling was undertaken in 1883–1918 and 1923–1925, respectively (Miyabe, 1931; Nyst et al., 2006), and revealed the coseismic displacement in the Kanto plain. The highest displacement occurred in the south Kanto region, with approximately 2 m uplift and 3 m southeastward horizontal movement (Sato and Ichihara, 1971; Nyst et al., 2006) (Figure 1-2a). Moreover, the tide gauge equipped in the southernmost tip of the Miura Peninsula (Aburatsubo station, Figure 1-1b) also recorded >1 m coseismic uplift (Kodama et al., 1980). Yamasaki (1926) and Imamura (1930) reported several minor inland displacements whose vertical movements were less than 1–2 meters. However, it is difficult to judge if they are the accompanied fault slip branching from the main fault or a secondary linear surface rupture, like as detected in the recent earthquakes (e.g., Fujiwara et al., 2016).

The 1923 event also caused huge tsunamis damaging the coastal towns and villages. Hatori et al. (1973) evaluated the tsunami heights by compiling the damage and inundation reports. The tsunami associated with the 1923 event outstands in the coastal areas surrounding Sagami bay, whose height was up to 12 m. On the other hand, in the Tokyo Bay and on the Boso peninsula facing the Pacific Ocean, the observed sea-level changes were much smaller and less than 2 m.

The strong motion data and teleseismic data are also recorded. Kanamori and Miyamura (1970) and Kanamori (1971) collected the seismogram records in domestic and worldwide stations. At that time, the Japan Meteorological Agency and the universities in Japan were operating seismometers at more than 60 stations nationwide. Although the seismograms at most of the nearby stations went off due to severe strong motion, the arrival times and first motions of P waves are well recovered (Kanamori, 1971). Most of the seismograms at that time are less reliable due to uncertain instrumental response and time record, but several stations had a sufficient quality of seismograms and were retrieved and digitized (Yokota et al., 1989; Takemura et al., 1994). Likewise, as for the teleseismic data, some records have low quality but can be recovered for the first motions of P waves (Kanamori, 1971), and the other records provide a high quality of seismograms (Wald and Somerville, 1995).

From these geodetic and seismological data, the characteristics of the source of the 1923 event have been evaluated. Right after the occurrence, based on the relationship between the arrival times and focal distance (Omori formula), the epicenter of the mainshock was roughly estimated to be located off Sagami bay (Imamura, 1925). After the establishment of the elastic dislocation theories and computational methodology, the detailed feature of the 1923 event was investigated. Kanamori (1971) inverted the focal mechanisms of the slip from the domestic strong-motion and teleseismic datasets. Along with the collected source distribution of the aftershocks, he estimated that the strike of the source fault is ESE direction, ranging from Tanzawa to the east off Boso Peninsula. Meanwhile, Ando (1971; 1974) reproduced the coseismic surface displacement obtained by the geodetic survey via the dislocation model (Maruyama, 1964). The Ando's fault model approximately overlaps the solution by Kanamori (1971) and matches the geological setting of the strike direction of the Sagami Trough. These coincidences strongly supported the idea that the 1923 Taisho earthquake was the interplate faulting caused by the subduction of PHS (Ando, 1974).

The source estimation of the 1923 event has been developed until the present. Matsu'ura et al. (1980) and Matsu'ura and Iwasaki (1983) developed the static inversion
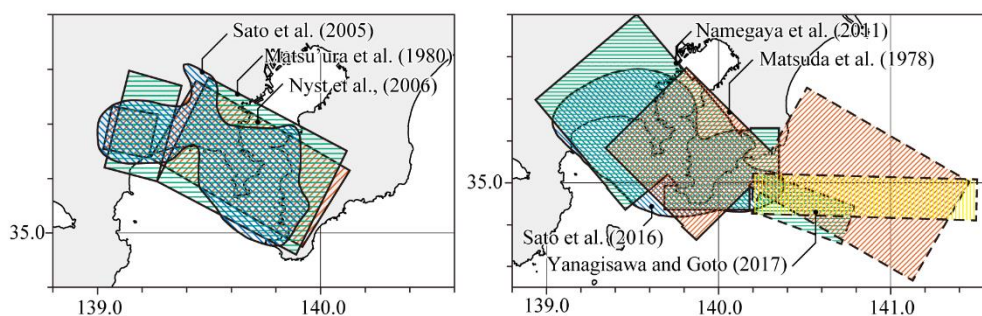
Figure 1-3. Estimated source areas of the historical Kanto earthquakes. (a) Source area of the 1923 Taisho earthquake estimated by Matsu'ura et al. (1980), Sato et al. (2005), and Nyst et al. (2006). (b) Source area of the 1703 Genroku earthquake estimated by Matsuda et al. (1978), Namegaya et al. (2011), Sato et al. (2016), and Yanagisawa and Goto (2017). The areas surrounded by dashed lines are estimated for the tsunami source faults.

method and evaluated the coseismic slip with single or two rectangle fault planes (Figure 1-3a). They furthermore synthesized the dynamic ground displacement at the nearby station (Matsu'ura et al., 1980) and the postseismic viscoelastic relaxation observed in the southern Kanto region (Matsu'ura and Iwasaki, 1983) using the optimal fault model and well reproduced the observation. Several source fault models have been proposed via the static inversion after that. Pollitz et al. (1996) pointed out the possible strike-slip fault crossing the Miura and Boso peninsulas implied by the inland and ocean floor geology and proposed it was the source fault of the largest aftershock that occurred a day after the mainshock (Takemura, 1994). Nyst et al. (2006) reevaluated the observation errors in the leveling survey and calculated the optimal fault slip with two rectangular fault planes based on the dislocation theory (Okada, 1985; 1992). Matsu'ura et al. (2007) developed the Bayesian inversion method for the static slip and proposed smoother coseismic slip distribution on the plate interface. On the other hand, the dynamic datasets, i.e., the waveform data of regional strong-motion and teleseismic stations, have also been utilized to constrain the coseismic slip distribution. Wald and Somerville (1995), Kobayashi and Koketsu (2005), and Sato et al. (2006) conducted the joint inversion of the geodetic data, teleseismic data, and the regional strong-motion data (Figure 1-3a). They estimated the temporal rupture propagation along with the total slip distribution in the event.

The overall characteristics of the 1923 event are getting consensus among most of the recent source inversion studies (Figure 1-3a). Almost all of the geodetic inversion results (Wald and Somerville, 1995; Kobayashi and Koketsu, 2005; Sato et al., 2006; Matsu'ura et al., 2007) agree that the coseismic slip of the 1923 event has two peaks; one is beneath Odawara, and the other is beneath from the Miura Peninsula to the south of the Boso Peninsula, whose slip amounts are up to 10–12 meters. The temporal slip inversion

results from the waveform data (Wald and Somerville, 1995; Kobayashi and Koketsu, 2005; Sato et al., 2006) suggest that the rupture started from the western slip patch (Odawara patch) and propagated toward the eastern patch, which agrees with a pioneering study (Imamura, 1925) and the descriptions of the suffered people (Takemura and Ikeura, 1994b). The total seismic moment released by the mainshock of the 1923 event is estimated to be 6.08×10^{20} (Nm) (Nyst et al., 2006) to 1.10×10^{21} (Nm) (Kobayashi and Koketsu, 2005) (Mw = 7.8–8.0).

1.1.2 1703 Genroku Kanto earthquake

The other historical earthquake on the Sagami Trough subduction earthquake interface occurred on Dec. 31, 1703, called the Genroku earthquake after the era name at the time. The observation data is significantly limited compared to the 1923 event so that the source estimation has relied on the descriptions in the historical documents and the geological investigations. Notably, the uplifted shoreline due to this event remains in the coastal region of the south Boso Peninsula and Miura Peninsula. The estimation of coseismic surface displacement by tracing the uplifted coast and other available datasets, such as the tsunami heights and historical documents, enabled us to investigate the coseismic slip distribution of the 1703 event.

The marine terrace landform developed in the southernmost part of the Boso Peninsula (the Awa region) (Figure 1-4) had long been known by geologists (Watanabe, 1929) and was documented to have emerged at the 1703 event (Genroku terrace). After the shock of the 1923 event, which caused significant crustal uplift in the south Kanto region (Figure 1-2a), the marine terraces got attention as the record of the past earthquakes. Imamura (1925) measured the elevation change at the southernmost tip of the Awa region, approximately 6 meters, referring to the old map drawn before 1703. Matsuda et al. (1974;
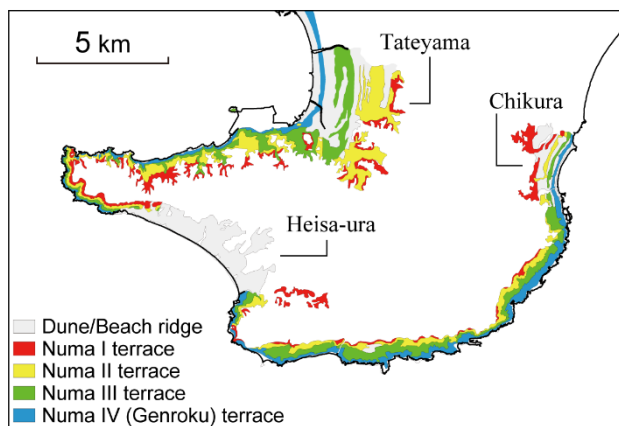
Figure 1-4. Detailed map of the Awa region. Colors indicate the conventional Numa terrace classification from Kawakami and Shishikura (2006).

1978) investigated the height distribution of the Genroku terrace and pointed out that the uplift amount of the 1703 event was prominent in the Awa region, which was significantly different from the 1923 uplift both in pattern and amplitude (Figure 1-4). Subsequent geological investigations (Nakata et al., 1980; Shishikura, 2000) conducted more detailed terrace classification and measurement and showed that the elevation of the Genroku terrace reaches the highest at the southernmost tip of the Awa region up to 7.5 meters and gradually decrease toward the north.

In the Miura Peninsula and the coastal region surrounding the Sagami Bay, the emerged benches and fossiled sessile assemblage uplifted during the 1703 event are identified above the 1923 coastline (Shishikura and Echigo, 2001). Unlike in the Awa region, the relative height between the 1703 and 1923 terraces is almost comparable to the 1923 uplift in the Miura Peninsula. In the western side of the Sagami Bay, around Odawara, where huge coseismic uplift was observed in the 1923 event, no clear landform indicating the coseismic uplift of the 1703 event is identified, leading to controversy as mentioned below.

Because the present elevation of the Genroku terrace includes the elevation change due to the 1923 event and the interseismic movement, it is required to extract each component to interpret the 1703 coseismic deformation. The interseismic movement comprises the postseismic relaxation and steady deformation due to the plate subduction. For the postseismic relaxation in tens to a hundred years, most of the source estimation of the old earthquakes, except for the recent ambitious model (Sato et al., 2016), include it into the coseismic deformation because limited observation makes it quite difficult to discriminate them. The steady deformation due to the plate subduction was problematic in the early studies. Matsuda et al. (1978) evaluated the subsidence rate from the description of the local people, and Shishikura (2000) utilized the record of the tide gauge equipped in the Awa region (Mera, Figure 1-1b) since the 1930s (Kodama et al., 1980). In recent years, the development of the nationwide global navigation satellite system (GNSS) network operated by GSI (GEONET) enabled the continuous observation of the inland elevation change and revealed the interseismic deformation rate (Sagiya, 2004) (Figure 1-2b). According to the GNSS observation, the Awa region and the Miura Peninsula subside at a rate of approximately 3 mm/year. Although there is a controversy whether this deformation rate has been constant for the past 300 years, several studies evaluated the coseismic uplift distribution of the 1703 event by extrapolating this geodetic observation (e.g., Namegaya et al., 2012).

The descriptions in historical documents and old maps also provide the

information to detect the region where no deformation occurred, which is valuable to identify the source area. Shishikura (2000) examined the position of the shoreline of Boso before 1703 and found that, around Hota (western coast) and Kominato (eastern coast) (Figure 1-1b), which located approximately 25 km north of the southernmost tip of the Boso Peninsula, that was likely no coseismic uplift or subsidence in the 1703 earthquake. For the western side of the Sagami Bay, Ishibashi (1977) referred to a description in the historical document that testified the shoreline retreat and evaluated the coseismic uplift amount to be approximately 2 meters. However, Matsuda et al. (2014) estimated the amount of the 1703 coseismic uplift to be less than 1 meter by referring to the elevation of the village already settled before 1703. Matsuda et al. (2015) also estimated the 1703 coseismic displacement at the Enoshima island in the middle part of Sagami Bay to be less than 1 meter.

The historical records also describe a huge tsunami accompanied the 1703 Genroku earthquake. Although no instrumental record of the tsunami height is available, the clues are provided by the descriptions in the historical document and monuments set up along the coast. Hatori et al. (1973) compiled the description of the 1703 tsunami and estimated the tsunami heights from the data, such as positions of damaged buildings. Furthermore, Hatori (1975b; c; 1976), Satake et al. (2008), and Namegaya et al. (2011) pointed out that religious monuments were established at the tsunami inundation limit in memory of victims or for cautionary notices. According to these investigations, the 1703 tsunami heights around the Sagami Trough were comparable to the 1923 tsunami, while those in the east Boso were much higher, up to 10 meters. Yanagisawa and Goto (2017) suggested from the historical records testifying an inundation into the inland lake in Choshi city, the northeastern end of the Boso Peninsula, with the tsunami height possibly exceeded 11 meters.

From such geological datasets, the source model of the 1703 Genroku earthquake has also been investigated (Figure 1-3b). Kasahara et al. (1973) and Matsuda et al. (1978) placed a steeper dip thrust fault just beneath the Awa region in addition to the source fault of the 1923 event (Ando, 1974) to reproduce the significant uplift there. Matsuda et al. (1978) further adopted an offshore source fault to the east of Boso to reproduce the sea-floor crustal uplift deduced from the tsunami height in the east coast of the Boso Peninsula (Hatori, 1975a). The subsequent source fault models (Aida, 1993; Shishikura, 2003; Satake et al., 2008; Namegaya et al., 2011) followed the concept that the 1703 event comprised a similar source fault to the 1923 event beneath Sagami Bay, additional exceeding slip beneath the Awa region caused huge crustal uplift there, and the slip

beneath sea-floor east off Boso generated the tsunami. Sato et al. (2016) constructed a kinematic inversion method for the slip distribution of the 1703 event taking into account the temporal elevation changes for 300 years as detailed later. Although they did not target the source of the tsunamigenic sea-floor deformation east off Boso, the evaluated coseismic slip distribution was consistent with the other models. The moment magnitude estimated by these models is Mw 8.1 (Namegaya et al., 2011) to 8.2 (Sato et al., 2016).

1.1.3 Other possible Kanto earthquakes in the historical era

Besides the 1923 Taisho and the 1703 Genroku earthquakes, several historical earthquakes are suspected to be the Sagami Trough subduction earthquakes. The candidate historical earthquakes and their probabilities are carefully reviewed by Ishibashi (2020), and he proposed four historical earthquakes that were highly probable; the 878 Gangyo earthquake, the 1293 Showo earthquake, the 1433 Eikyo earthquake, and the 1495 Meio earthquake, each named after the era name (Usami et al., 2013). The source of these earthquakes is regarded as similar to that of the 1923 Taisho earthquake (Taisho-type earthquakes defined below), and thus it is not easy to detect the geological evidence preserving the coseismic deformation. Ishibashi (2020) judged the probability based on the criteria such as whether the tsunami hit on the Sagami Bay to Boso coast, whether the shaking was felt in a wider area, even including western Japan, and whether the aftershock sequence lasted for several days, to discriminate them from inland earthquakes. The geological surveys detected tsunami deposits and abrupt sea-level changes whose ages correspond to these earthquakes (Fujiwara et al., 1999; Shimazaki et al., 2011; Mannen et al., 2018). Of course, it is quite difficult to assert it because the quality and quantity of the records are much worse than the recent earthquakes. However, the historical records support that the Kanto earthquakes repeatedly occurred at intervals of 400 years at the longest in the past 1200 years.

1.1.4 Prehistoric earthquakes

The previous geological investigations have revealed the past earthquakes occurred before the available human records. Along the coastal region in south Boso and around the Sagami Bay, various geological evidence of past earthquake events is observed. One of the most obvious paleoseismological features is the marine terrace sequence developed in the Boso and Miura peninsulas (Kayanne and Yoshikawa, 1978; Nakata et al., 1980; Kumaki, 1985), which preserve the past relative sea-level changes and the timings of abrupt crustal deformations. Additionally, the beach ridge sequences (Shishikura et al., 2001) and the tsunami deposits (Fujiwara et al., 1999) discovered in

this region also indicate the recurrence of earthquakes more frequently than the marine terrace formation (Shishikura, 2014).

Watanabe (1929) first reported that the marine terrace landform in the Awa region is divided into several levels by the cliffs and indicated the coast had suffered repeating uplift events like the 1923 Taisho and 1703 Genroku earthquakes. Sugimura and Naruse (1954; 1955) classified the marine terrace platform above the 1923 shoreline into three levels and indicated that the elevation distribution of the highest terrace (named Numa terrace after the place name) is also correlative to the historical uplifts. The subsequent geological studies (Matsuda et al., 1974; 1978; Yonekura, 1975; Yokota, 1978; Nakata et al., 1980; Kawakami and Shishikura, 2006) had updated the classification of the marine terraces via the field surveys and aerial photography readings (Figure 1-4). Matsuda et al. (1978) and Nakata et al. (1980) classified them into four levels of terrace platforms, including the Genroku terrace, and numbered them Numa I–IV in descending order. Based on the geomorphological similarity of these marine terraces to the Genroku terrace, they estimated the recurrence of earthquakes whose source region is similar to the 1703 Genroku earthquake (called the Genroku-type earthquakes).

The formation ages of the Numa terraces, which suggest the occurrence ages of the Genroku-type earthquakes, are evaluated by the dating study of fossils associated with the terraces. Unlike the younger terraces, it is rare to find the in-situ sessile assemblage directly indicating the emergence ages. Therefore, the previous surveys often had targeted the seashore sediments deposited just before the emergence, called terrace deposits, and dated fossils of marine organisms such as shell fossils buried in them. Matsuda et al. (1978) first evaluated the formation intervals of the Numa terraces to be approximately 1,500 years using the dating result (Yonekura, 1975) in Chikura, eastern coast. Nakata et al. (1980) increased the number of dating samples along the coast and evaluated the intervals were varied within 1,450–2,600 years. Note that the radiocarbon dating method at that time was early-dated (proportional counter method), and the corrections applied in the later studies using accelerator mass spectrometry (AMS), such as $\delta 13C$ mass correction (Stuiver and Braziunas, 1993), and marine reservoir calibration was not considered. Later, Fujiwara et al. (1999) evaluated the calibration value of Nakata's dataset and proposed the emergence ages of the Numa I–III terraces were approximately 7,200, 5,000, and 3,000 years ago, in descending order.

Besides the Numa terrace, several geological studies have tried to reveal the occurrence ages of the prehistoric events. Shishikura (1999) and Shishikura et al. (2001) indicated that in the lowlands located on the west coast of the Boso Peninsula, there

developed beach ridge sequences comprise four to ten abandoned dunes. Reflecting the observation that no significant uplift occurred during the 1703 earthquake (Shishikura, 2000) while a few meters of uplift was detected during the 1923 earthquake, they assumed the repeating Taisho-type earthquakes formed these sequences. Shishikura et al. (2001) estimated the formation interval of this sequence to be 400–1,000 years in the past 7,000 years based on the dating investigation. Several levels of small cliffs are also identified between the Numa terraces along the rocky coast in the Awa region and are suspected to be uplifted due to the Taisho-type earthquakes, although they are not dated (Kayanne and Yoshikawa, 1978).

In the Miura Peninsula and the surrounding coast of the Sagami Bay, several levels of marine terraces also developed. Kumaki (1985) identified three levels of Holocene marine terrace in the southeastern coast of the Miura Peninsula and named them Nobi I–III terraces. The dating survey results showed that their emergence ages were approximately 6,000, 4,600, and 3,000 years ago. Although several studies (e.g., Sato et al., 2016) regard the Nobi terraces as the counterpart of the Numa terraces, their formation source is unclear because of several questions such as the comparable uplift amount observed in 1923 Taisho and 1703 Genroku events. In the east of the Odawara area, there also develop three levels of the Holocene marine terraces. However, their formation process is also uncertain because the 1703 Genroku earthquake less likely generated any uplift in this region, as mentioned above (Matsuda et al., 2014), while more than 2 meters of uplift was measured in the 1923 event (Miyabe, 1931).

Because the Kanto earthquakes generate enormous tsunamis exceeding 10 meters, tsunami deposit is another important evidence for revealing the prehistoric events. Fujiwara et al. (1997; 1999; 2000) investigated the outcrops of the rivers and coring samples in the southernmost part of the Boso Peninsula and detected seven possible tsunami events in the past 8,000 years. Fujiwara et al. (1999; 2000) also conducted coring surveys in the Miura Peninsula and revealed tsunami deposits whose ages are consistent with those in the Boso Peninsula. On the other hand, the older inner-bay sediment, which is a better preservation circumstance for event deposits, recorded much shorter intervals (100 to 300 years) of tsunami events (Fujiwara and Kamataki, 2007). It should be noted that the tsunami deposits are not always the records of the Sagami Trough events and possibly include distant earthquakes (Hatori, 1975a)

By summarizing the observations by the previous studies, two-types of the Kanto earthquakes having different interval times and magnitudes are estimated. Shishikura (2014) proposed the rupture scenario of the earthquake along the Sagami Trough that (i)

the seismogenic zone along the Sagami Trough is divided into three segments; (A) Sagami Bay segment, (B) south Boso segment, and (C) off Boso segment, which generate the crustal deformation and tsunamis around the Sagami Bay, huge crustal uplift in the Awa region, and huge tsunamis in the eastern coast of the Boso Peninsula, respectively, and that (ii) the Taisho-type earthquakes rupture only the segment A with shorter intervals of 200–400 years, and the Genroku-type earthquakes rupture entire segments with longer intervals than 2,000 years.

1.1.5 Open questions about the Kanto earthquakes

The recurrence history of the Kanto earthquakes is getting elucidated by the previous studies as introduced above. However, the inconsistencies within the geomorphic, geologic, and geodetic observations remain, and the proposed rupture and deformation history has a weak geophysical agreement and has received some objection from the geophysical modeling studies. Here, I review the existing problems to be solved about the Kanto earthquakes.

The source analyses of the 1703 Genroku earthquakes have estimated the slip amount reached 10–20 meters beneath the Awa region (segment B in Shishikura's scenario). On the other hand, the geodetic surveys evaluated the coupling (slip deficit) rate on the plate interface along the Sagami Trough (Sagiya, 2004; Noda et al., 2013) estimated that this segment accumulates 30–40 mm/year slip deficit. If we assume that segment B ruptures every more than 2,000 years, the accumulated slip deficit amount should exceed 70 meters.

Previously, as indicated by Sugimura and Naruse (1954; 1955), the Holocene highest terrace has been considered to correlate with the distribution of the coseismic uplifts. However, Shishikura (2001) reported that uplifted seashore deposits in the middle part of the Boso Peninsula while there is no significant uplift during the historical earthquakes. Hence, another source of uplift movement is required to explain this inconsistency.

The similarity in the Numa terraces distributions has been the grounds for the recurrence of the Genroku-type earthquakes (Figure 1-4). However, the previous studies have not explained the formation process, specifically the elevation change history, during the whole series of the Numa terraces. Assuming the basic kinematics in the subduction zone, the interseismic and coseismic deformation patterns show the opposite direction (Savage, 1983) and possibly cancel out with each other after completing one sequence of the earthquake cycle. The previous studies (Matsu'ura and Sato, 1989; Sato et al., 2016;

Noda et al., 2018) have pointed out this problem and propose a mechanism for the Numa terraces remained above the sea-level. Sato et al. (2016) modeled the source slip of the 1703 Genroku earthquake based on the kinematic model of Matsu'ura and Sato (1989). They predicted that the coseismic deformation pattern, which contributes to the greater part of the elevation of the Genroku terrace, will decrease due to the slip deficit in the next hundreds of years, and the long-term deformation is approximated to be the steady deformation due to the plate subduction. Noda et al. (2018) tried to explain the coastal landform of the Boso Peninsula via the interaction of the steady uplift and the oscillations of sea-level change. However, it requires extraordinary sea-level changes during the Holocene period than the generally accepted eustatic change history.

The current rupture scenario by Shishikura (2014) is an extrapolation of the historical earthquakes which assumed based on the geological investigations. However, there arise inconsistencies when we try to explain such estimations quantitatively, such as an inconsistency between the coseismic slip and the interseismic slip deficit amount, a difference between the coseismic deformation pattern and long-term deformation pattern, and the discrepancy between the marine terrace distribution and the expectation from the kinematic model. To understand the earthquake recurrence along the Sagami Trough, we are required to reproduce the observations by the synthetic crustal deformation with a geophysical model. However, we currently have another problem: the available dataset of the marine terraces, which represents the crustal deformation history, is less quantitative and objective for the usage in geophysical models. Therefore, in this study, I first aim to increase the objectivity of the geological and geomorphological dataset of the Numa terraces, and then to construct a model to explain the observation by proposing the rupture scenario along the Sagami Trough in the past 7,000 years.

1.2 General introduction to this study

This study comprises three sections. Sections 2 and 3 describe the quantitative geomorphological and geological re-investigation of the Numa terraces, respectively. In section 4, I propose a rupture scenario of the Kanto earthquakes by constructing a mechanical plate subduction model to explain the observation. As mentioned above, for constructing the more objective rupture scenario, a more quantitative dataset of the Numa terrace distribution is required. Therefore, the geomorphological and geological studies employ new statistical methods targeting the quantitative elevation distribution and the formation ages of the Numa terraces, respectively. In the geomorphological study, I propose a new computational method to obtain the positions and elevations of the marine terraces by using the digital elevation model (DEM) along the coast. In the geological

study for dating the Numa terraces, I newly obtained dating samples and compiled them with previous data. Then, I construct a new statistical evaluation method to evaluate the formation ages of the marine terraces with the compiled dating samples. The resulting comprehensive dataset represents the formation process of the Numa terraces, revealing the crustal deformation history in the Awa region. Finally, in order to infer the scenario of the Kanto earthquakes, I construct the three-dimensional subduction model of the Sagami Trough, taking into account the stress accumulation and rupture recurrence.

2. Reexamination of the Numa terrace distribution

2.1 Introduction: Geomorphological analysis

2.1.1 Geomorphological investigation of marine terraces

Marine terraces are characteristic coastal landforms that provide evidence for short- to long-term relative sea-level change (Bradley and Griggs, 1976; Lajoie, 1986). Some marine terraces form due to eustatic sea-level changes on the scale of 10^5 years that are caused by steady tectonic uplift (Chappell, 1974; Bradley and Griggs, 1976; Anderson and Menking, 1994), while others result from recent intermittent crustal deformation such as that associated with interplate earthquakes (Shimazaki and Nakata, 1980; Scott and Pinter, 2003; Shishikura, 2014). Because marine terraces preserve essential information regarding past tectonic movements, stair-like coasts around the globe have long been the subject of many kinds of geomorphological research.

The essential information provided by a marine terrace is its emergence age and the magnitude of the past relative sea-level change. The emergence age is usually estimated by dating fossil shells, corals, botanical materials, or tephra deposits (Sieh et al., 1999; Komori et al., 2017; Berryman et al., 2018). The relative height between the uplifted old shoreline and the modern shoreline indicates the cumulative amount of vertical displacement since its emergence. These geomorphological data have been used to determine the crustal uplift rate (Bradley and Griggs, 1976), a record of sea-level change (Pirazzoli et al., 1993), and history of paleo-earthquake activity (Atwater et al., 2004). Especially, coastal uplift history has essential importance as observed evidence of earthquakes in the past. The huge abrupt coastal uplifts in subduction zones are widely believed to be caused by Mw 7 to 9 sized large earthquakes with the recurrence intervals of hundreds and thousands of years, which are fundamentally difficult to be covered by the instrumental observations as well as historical accounts.

The amount of relative sea-level change can be roughly estimated by the present height of the marine terraces. However, to determine the precise elevation change of less than a meter scale, it is essential to clarify what geometry in the marine terrace sequence indicates the old mean sea-level. The widely used criteria are to assume that the shoreline angle (the "inner edge" of the wave-cut platform formed due to erosion by sea waves at the intersection between the sea cliff and the platform) approximately corresponds to the altitude of mean sea level (Keller and Pinter, 2002). On the other hand, Kayanne and

Yoshikawa (1986) investigated the coastal landform of the Boso Peninsula and suggested that at erosional shorefront there develop a bench whose surface height corresponds to the mean sea-level and a small cliff (nip) plunges into the sea as deep as 2 to 5 meters above an abrasion platform. The inner edge of the uplifted platform (paleo-shoreline angle) was originally the bottom of the emerged nip, and thus the past mean sea-level is supposed to be a few meters higher than the paleo-shoreline angle. However, as discussed in Kayanne and Yoshikawa (1986), this sequence undergoes a complex process of erosion at shorefront, which might be different depending on the coastal circumstances, and thus there are no widely accepted criteria to precisely detect the past mean sea-level from the uplifted marine terraces. The validity of this definition is discussed later in section 5.

This study does not focus on the minor cliffs formed in the vicinity of the large-scale terrace cliff (Kayanne and Yoshikawa, 1986; Uesawa and Miyakawa, 2015), which are suspected of having uplifted due to the Taisho-type earthquakes. This hypothesis requires more evidence because no other observation, such as dating, is obtained than the surface profiles on several survey lines. A large number of dating samples are required for each level to constrain the terrace age to be less than a few hundred years, as discussed later in section 3. However, I propose that the geomorphological method developed in this study can be useful for the minor levels of marine terraces by tuning special filtering into these scales, as described below.

Besides, the sedimentary coast shows a different pattern of marine terrace sequence from the erosional rocky coast. The platforms are divided by abandoned dunes, which were originally formed just behind the shoreface by eolian deposits. As investigated by Shishikura (1999) and Shishikura et al. (2001), the beach ridges sequence parallel to the coast indicates the past uplifts. However, as discussed in Komori et al. (2017), the landform of the sedimentary coast tends to suffer erosion, weathering, and compaction severely and thus does not produce precise indicators for the past sea-level.

For the classification of terraces into generations, the detection of the paleo-shoreline is widely conducted. Although the previous studies have often relied on field survey and aerial photography interpretation to detect paleo-shoreline angles, in actual coastal topography, it is rare to find a typical terrace-like structure because of erosion and sedimentation, which make it difficult to maintain the objectivity of the classification with conventional methods. In this study, therefore, I aim to develop a new statistical method for a more objective classification of marine terraces. Although dating of marine terraces is useful to constrain the continuity of the same generation, dating materials, such as shell fragments, plants, and other organic matters, are limited in specific circumstances and are

not always found. For the detailed interpretation of the history of the coastal uplifts, the geomorphological analysis will provide independent data that enables us to evaluate along-coast continuity of the sparsely dated terraces.

The use of DEMs has recently come to play a fundamental role in various geomorphological fields. A DEM dataset, derived from LiDAR (Laser Imaging Detection and Ranging) surveys or structure-from-motion photogrammetry, enables not only visualization of elevation distribution but also analysis of landforms using statistical approaches. For example, in active fault detection, automated statistical analysis has long been used to detect lineaments in DEMs (e.g., Oguchi et al., 2003). DEM datasets also have been used effectively for the investigation of marine terraces. For example, Scott and Pinter (2003) identified terrace platforms numerically by discriminating them from intervening cliffs based on the slope and relief values calculated from mapped elevation data. Likewise, the previous methods usually extract terrace platforms based on certain geomorphological parameters, such as curvatures, and then classify them according to generation by referring to information of dating (Scott and Pinter, 2003; Bowles and Cowgill, 2012). However, the applicability of this method is limited because it postulates different terrace platforms to be horizontally separated by degraded terrace cliffs. In this paper, to overcome such difficulties, I have devised a new statistical classification method applicable to various environments by considering the elevation of the uplifted shoreline angle and its lateral continuity.

2.1.2 Cluster analysis

One of the methods developed in this study employs the K-means clustering method (Lloyd, 1982; Bishop, 2006) for the grouping. The K-means clustering is a basic grouping technique that partitions a set of data points into a number (K) of clusters. The K-means is considered as an unsupervised machine learning method. The cluster analysis has recently been utilized in various geophysical fields, such as in geodesy (Simpson et al., 2012; Takahashi et al., 2019), structural geology (Eymold and Jordan, 2019), and seismology (Perol et al., 2018). I used a class of the K-means clustering called model-based clustering, which assumes, as prior information, a specific structure in the spatial distribution of the point cloud data set. Such an approach has been used by Dasgupta and Raftery (1998) to correlate the seismic activity along faults by assuming the linear distributions.
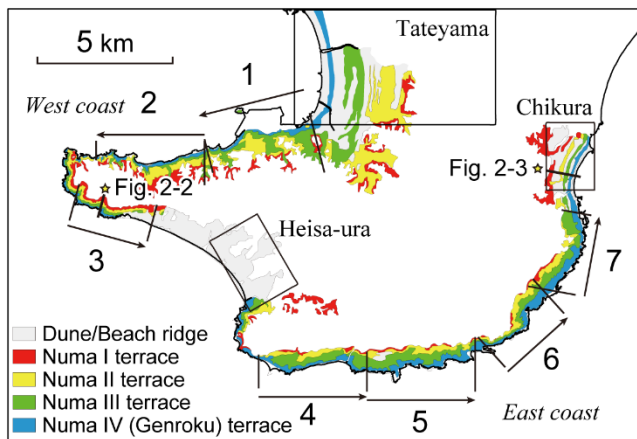
Figure 2-1. Survey area of the geomorphological analyses. Numbers and arrows indicate the analysis segments for the rocky coast. Stars indicate the survey lines for the surface profiles in Figure 2-2a and Figure 2-3a. Colors indicate the conventional Numa terrace classification from Kawakami and Shishikura (2006).

2.1.3 The object of the geomorphological survey

The coastal region of the Boso Peninsula, the main subject of this study, can be classified into sedimentary and rocky coasts, and the development of the Numa terraces has been investigated for each type, respectively. Sedimentary coasts are developed mainly in the Tateyama lowland, facing Tokyo Bay, in the Heisa-ura lowland on the southwestern coast, and in the Chikura lowland on the eastern coast (Figure 2-1). In the Tateyama lowland, four broad terrace platforms have been classified and dated on the basis of shell fragments and plants (Shishikura and Miyauchi, 2001; Shishikura et al., 2005; Fujiwara et al., 2010). In the Chikura lowland, five broad terrace platforms have been identified and dated by Komori et al. (2017). Although the Heisa-ura lowland is also recognized to be a raised sandy beach, no terrace platform has been identified there. The rocky coasts are roughly divided into two regions: between the Tateyama and the Heisa-ura lowland (west coast), and between the Heisa-ura and the Chikura lowland (east coast). The length of the west and east coasts are approximately 11 km and 15 km, respectively. Four Numa terrace levels have been classified along both of the rocky coasts (Kawakami and Shishikura, 2006) (Figure 2-1).

In this study, I conduct two types of classification methods using DEM depending on the coast types. In the rocky coasts, although the classification has been done by the previous investigations (Matsuda et al., 1974; Nakata et al., 1980; Kawakami and Shishikura, 2006), the classification criteria need more objectivity as mentioned above, and the elevation data is obtained sparsely. Therefore, I develop a new statistical method to detect the paleo-shoreline angles along the coast and obtain a more objective and quantitative terrace classification map of the Numa terraces. The other survey targets the landform in the Heisa-ura lowland, where previously no terrace platform has been

identified. I apply a different detection method for the abandoned dunes because of the different characteristics of the marine terrace sequence from the erosional rocky coast.

Additionally, I discuss the correlations of several geomorphological parameters, including the curvatures of cliffs and widths of terrace platforms quantified by the current method with the ages of the marine terraces. This examination has implications for the understanding of marine terrace formation and degradation processes. This method not only detects the elevation of the uplifted shoreline angles but also enables us to obtain other geomorphological datasets that were difficult to gather using the conventional methods.

2.2 Methods and materials

The classificatory process for the rocky coasts consists of two main steps. The first is the extraction of cliff bases (which indicate the locations of the paleo-shoreline angles) from surface profiles perpendicular to the coast (Figure 2-2a), to be used as the set of data points (i.e., picked locations of cliff bases) along the coast (Figure 2-2c) for the next step. This step corresponds to the "feature extraction" in common machine learning methods (Bishop, 2006). The second, clustering step (Figure 2-2d), is based on K-means clustering with some modification to introduce prior information about the lateral continuity of the marine terraces. On the other hand, the classification in the sedimentary lowland employs a stacking method of the geomorphological parameter profiles in the vertical direction for the detection of the elevation of the abandoned dunes.

2.2.1 Dataset

I employed DEM analysis for a more accurate interpretation of the Numa terraces. The dataset used in this study is a detailed DEM with a grid interval of 0.5 m that was generated from the observation points obtained by fixed-wing airborne LiDAR from 2012 to 2013 (Shishikura et al., 2014a), which covers mainly lower than 40 m above sea level (a.s.l.) in the Awa region (Figure 2-1). The averaged density of observation points is 5.0 to 11.0 points per m^2. The land artifacts and vegetation are eliminated and flattened via automatic and manual filtering. The accuracy of the absolute elevation value is estimated from the standard deviation to be within 0.3 m for data points where ground data were obtained and 2.0 m where the elevation value was obtained by interpolation (Shishikura et al., 2014a).
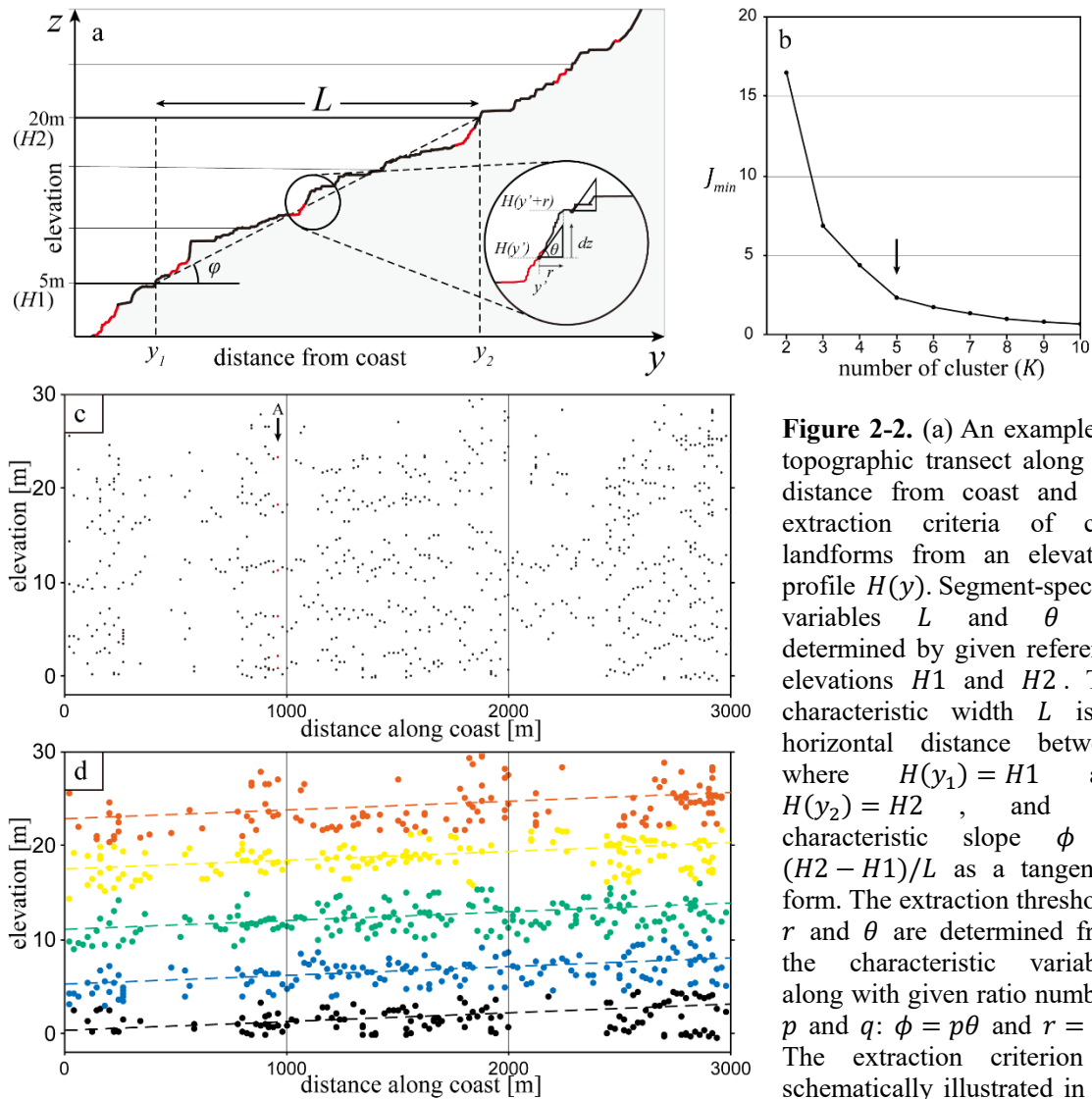
Figure 2-2. (a) An example of topographic transect along the distance from coast and the extraction criteria of cliff landforms from an elevation profile $H(y)$. Segment-specific variables L and θ are determined by given reference elevations $H1$ and $H2$. The characteristic width L is a horizontal distance between where $H(y_1) = H1$ and $H(y_2) = H2$, and the characteristic slope ϕ is $(H2 - H1)/L$ as a tangential form. The extraction thresholds r and θ are determined from the characteristic variables along with given ratio numbers p and q: $\phi = p\theta$ and $r = qL$. The extraction criterion is schematically illustrated in the circle. The red sections on the profile indicates the accepted points for the paleo-shoreline angles. (b) Decline curve of the minimum value of the objective function $J_{\min}$ (equation (2-3)) with respect to the number of cluster K for section 3. The arrow indicates the adopted number of clusters judged from the slope change. (c and d) Elevations of the extracted cliff locations plotted against along-coast distance (c) and corresponding clustering result (d) of section 3 (see Figure 2-1). The dashed lines in d are the parallel center lines of the clusters and the color of the dots corresponds to the classified clusters. The arrow in c indicates the position of the profile shown in a.

2.2.2 Classification in the rocky coast

2.2.2.1 Feature extraction

First, I will extract elevations corresponding to the paleo-shoreline angles from the elevation profiles of the coast. Figure 2-2a schematically explains the procedure of this step. I first prepare elevation profiles perpendicular to the coast from the original DEM data at w (m) interval along the coast that can be expressed as the functions $H(y)$,

where y is the distance from the coast. Here, I removed tiny bumps from the original profiles not related to marine terraces, such as artifacts and dunes, resulted in a monotonically increasing function (Figure 2-2a). Next, I search for the positions on the distance y' as the cliff bases that satisfy $H(y' + r) > H(y') + dz$, where the elevation increases by dz $(= r\tan\theta)$ with respect to the search radius r. This criterion identifies the location where the difference of the elevations is larger than dz in an interval of r, as shown in Figure 2-2a (inset). Because several neighboring positions on y' can similarly satisfy this criterion, I subsequently calculate the curvature at each position and choose the point showing the largest curvature as the representative point. This criterion better prevents the duplicate counts of cliff base points than solely using the values of the curvature or gradient at each data point individually.

Two control parameters are used for threshold setting: the search radius r and the threshold angle θ, which behave together as a band-pass filter, picking out the topography on a particular length scale. In the actual coastal topography, there is some diversity in the width of the terrace platforms and the angle of the terrace cliffs; hence, I have explored setting parameters suitable to each coastal topography. The threshold angle, θ, is determined from the ratio p with respect to the average slope ϕ of the strip: $\theta = p\phi$. The average slope ϕ is obtained using the relation $\phi = (H2 - H1)/L$, where L is the horizontal distance between points with elevations of $H1$ (m) and $H2$ (m) (illustrated in Figure 2-2a). $H1$ and $H2$ are set to be 5 (m) and 20 (m) here. Likewise, the search radius, r, is determined by the ratio q with respect to the length L: $r = qL$. These factors, p and q, can now be set uniformly over the survey region. Their settings will ensure that the threshold angle θ is sufficiently larger than the slope on platforms but does not exceed the slope on cliffs and that of each platform. These settings should be changed according to the terrace ages and modes of the formation when applying to the other survey regions. For the Numa terraces, I set them as $p = 2.0$ and $q = 2.5(\%)$.

Different tuning of these criteria can extract other scales of landforms. These values tuned in this study is targeting the inner edge of the platform and filtering out smaller terraces identified in previous geomorphological studies (Kayanne and Yoshikawa, 1986; Uesawa and Miyakawa, 2015), which indicate the uplift due to the Taisho-type earthquakes and the bench-nip sequences. In this study, I apply consistent criteria along the survey region to maintain the objectivity of the classification. Because the smaller landforms are not uniformly detected along the coast, I did not use them as the classification criteria. As shown in Figure 2-2a, the numbers of picked up points along

the most profiles are four to six, including the modern coast, consistent with the expected number of the Numa terraces and indicating the smaller cliffs are less included.

2.2.2.2 Clustering

As exemplified in Figure 2-2c, the two-dimensional point cloud $\{d_1, \cdots, d_N\}$ representing the positions of the cliff bases whose components are distance along the coast and elevation is obtained from the previous step for the entire profiles along the coast (N denotes the number of the entire extracted points). Next, I relate this data set to each marine terrace generation. The paleo-shoreline angles should ideally align in the elevation view (plots on the elevation versus the along-coast distance). The cliff bases in the actual topography may have suffered erosion and sedimentation, and their elevations may have slightly changed. Here, I conduct clustering of the point data set by considering vertical dispersion of the positions of the points.

I use the K-means method, which is a standard clustering method for point data sets, that searches for the best grouping of the data points via iterative calculations. According to Bishop (2006), a set of points $\{d_1, \cdots, d_N\}$ is optimally divided into a certain number of clusters in basic K-means clustering by minimizing the objective function described by

$$J = \sum_{n=1}^{N} \sum_{k=1}^{K} r_{nk} \|d_n - \mu_k\|^2, \tag{2-1}$$

where μ_k is a vector representing the center points of clusters, and r_{nk} is a binary indicator: when n-th data point belongs to the kth cluster, r_{nk} takes 1, otherwise takes 0. K is the number of clusters. In the application, the objective function J is minimized through an iterative procedure, where each data point is first assigned to the closest cluster center, and then each cluster center is calculated from the newly assigned data set, to minimize the summation of the norms. See Bishop (2006) for details of the method.

In the new method, I modified this procedure to pick out cluster structures surrounding centerlines rather than center points from the data set $\{d_1, \cdots, d_N\}$. Because these data points are expected to be paleo-shoreline angles that emerged due to recurrent crustal uplifts (or sea-level drops), the elevation of the corresponding cliff bases is expected to be aligned within each cluster. Therefore, I used centerlines instead of center points (μ_k), in the objective function of the K-means method. When the centerline for the

k^{th} cluster is given by $z = a_k x + b_k$, where $x, z, a_k,$ and b_k are distance along the coast, elevation, and intercept and slope of the kth cluster, respectively, norm D between the line and each point is

$$D_{nk}^2 = \frac{(a_k d_n^x - d_n^z + b_k)^2}{a_k^2 + b_k^2} \qquad (2\text{-}2)$$

where d_n^x and d_n^z denote the distance along the coast and elevation of the nth data point, respectively. Hence, the objective function J is given by replacing the norm in equation (2-1):

$$J = \sum_{n=1}^{N} \sum_{k=1}^{K} r_{nk} D_{nk}^2 \qquad (2\text{-}3)$$

The minimization of J is realized through the same procedure as in the basic K-means method, i.e., iterative minimization of r_{nk} by assignment of the data points to the closest centerline and minimization of D_{nk}^2 by redrawing centerlines with the least-square fitting, as shown in Appendix A.

Additionally, to prevent the iteration from falling into a local minimum, I stabilize the analysis by reducing the number of parameters. Specifically, I assume the centerlines are parallel to each other, $a_1 = a_2 = \cdots = a_K = a,$ and equation (2-2) is reduced to $D_{nk}^2 = (a d_n^x - d_n^z + b_k)^2/(a^2 + b_k^2)$. This assumption will not contradict with our intuition for a sufficiently small interval along coasts, supposing that each terrace was formed by similar coseismic uplift with the onshore surface gradient as small as about 25 mm per 1 km (e.g., Thatcher, 1984 for an Mw 8.4 subduction interface earthquake), resulted in negligibly small variation of the gradients between the different generation of terraces. Under this assumption, we can still safely quantify the accumulated deformation through the variable intercepts b_k or the relative terrace height. I will evaluate the validity of the assumption of parallel centerlines later by comparing the results between neighboring clustered sections. On the other hand, the larger gradient changes of the vertical deformations are reported in the vicinity of the nearshore upper plate faults: >1 m per 1 km in the 2016 Kaikoura earthquake (Clark et al., 2017) and 0.5 m per 1 km in the 1964 Alaska earthquake (Plafker, 1969). When analyzing such deformations due to inland faults, relaxing the above restriction (increase the number of the free parameters) will be required to adjust for the analyses of the localized small-wavelength deformations.
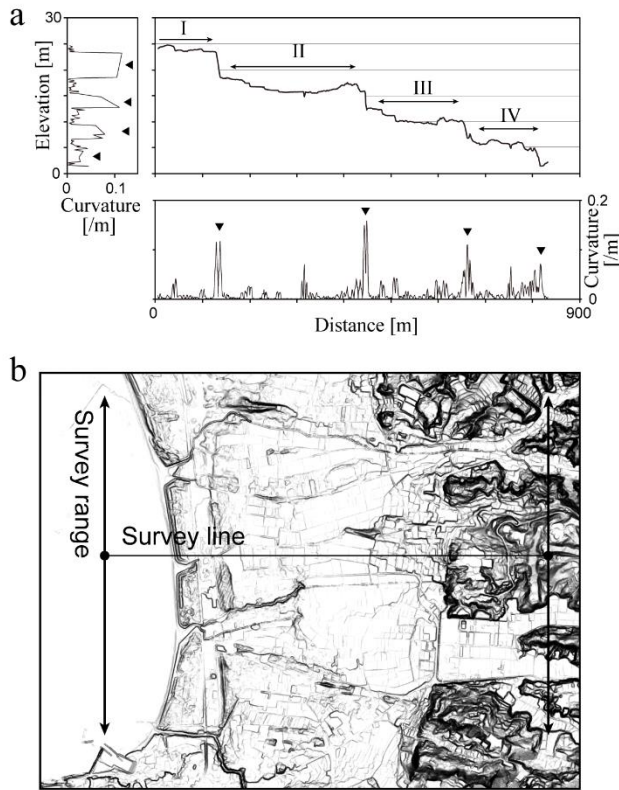
Figure 2-3. (a) Relationship between the surface profile and distribution of the absolute value of the curvature. (Top right) The surface profile taken from the Chikura lowland. The horizontal projection (bottom) and the elevation projection (top left) of the absolute value of the curvature. In both projections, the boundaries of platforms (terrace cliffs) correspond to the peaks of the profiles, indicated by triangles. (b) Settings of the survey lines for stacking in Heisa-ura. The surface profiles are taken on the survey lines with a 2-meter interval (solid lines).

Extension of the current method to such conditions will be an issue of our future study. Moreover, artificial landforms included in the DEM data are expected to be less effective using this classification criterion because such artifacts do not have lateral continuity in a long distance along the coast.

The number of clusters, K, is needed to be specified as an input to K-means clustering. Choosing the number of clusters is, however, an essential issue in clustering problems, and a generally applicable solution has not been reached yet. As for the Numa terraces, the number of terraces is already known to be five, including the modern one, and we can use this prior information in the clustering. However, I try to obtain the number of clusters independently in this study and verify the robustness of this method. Herein, I adopt the elbow method (Tibshirani et al., 2001) to determine the optimal number of clusters in each section. The evaluation with the elbow method is exemplified in Figure 2-2b. Here, the minimum value of J (J_{min}) generally decreases with an increase in the input number K, and J_{min} tends to decrease steeply with a small value of K and to turns to be gentle if K exceeds the optimal number of clusters, which is $K=5$ here. I determine the optimal number of clusters in each of seven sections along the coast.

2.2.3 Classification in the Heisa-ura lowland

For the terrace classification in the sedimentary lowlands, I adopted the curvature value for the classification criteria that are supposed to show different values on the dune geometry. Considering a 1D surface profile of marine terrace, as shown in Figure 2-3a, the absolute value of the curvature takes maximum at the base of the terrace-cliff or abandoned dune, which marks the landside limit of the terrace platform. To improve the certainty of the recognition, I conduct a stacking of vertical profiles of the curvature value. Same as in rocky coasts, the elevation of the characteristic geomorphological parameters of the marine terrace has lateral continuity in a narrow region. Thus, by stacking the vertical profiles taken from many surface profiles along the coastline, the signal (terrace landform) can be separated from the noise (local landform independent to terraces). I set parallel lines crossing the survey region, as shown in Figure 2-3b, arrange survey lines with 2-meter intervals connecting them, and obtain the vertical profile of the curvature value from the surface profile along each survey line. Finally, I calculate the average value of the vertical profiles in each survey region and detect the elevations of the abandoned dunes.

2.3 Analysis results and verification of the method

2.3.1 Extraction of cliff bases

Figure 2-2c shows the elevations of the extracted cliff bases plotted as the function of the along-coast distance for shoreline section 3 (Figure 2-1). The individual points (755 points in total) correspond to the elevations extracted in each of 150 profiles with a 20 m interval set along the coast of 3 km–wide.

The points plotted above were classified into sub-horizontally parallel clusters by applying the modified K-means clustering method. Figure 2-2d shows the results of the clustering, where the number of clusters was determined as K = 5 based on the obvious infection point of the elbow method (arrow in Figure 2-2b). The color of dots differentiates the classified clusters, which derived from the optimal r_{nk} in equation (2-3). The dashed lines indicate the parallel centerlines of each cluster. The obtained common slope value a is 6.63×10^{-5} (%), and the elevations of the centerlines at mid-point are 1.43, 6.31, 12.13, 18.49, and 23.86 (m a.s.l.) in ascending order.

Figure 2-4a shows the classified points obtained for all seven sections in the survey region shown in Figure 2-1. Sections 1, 2, 4, and 5 are 4-km wide, and sections 3, 6, and 7 are 3-km wide. The surface profiles are examined from −5 m to 30 m a.s.l. in all

a

b
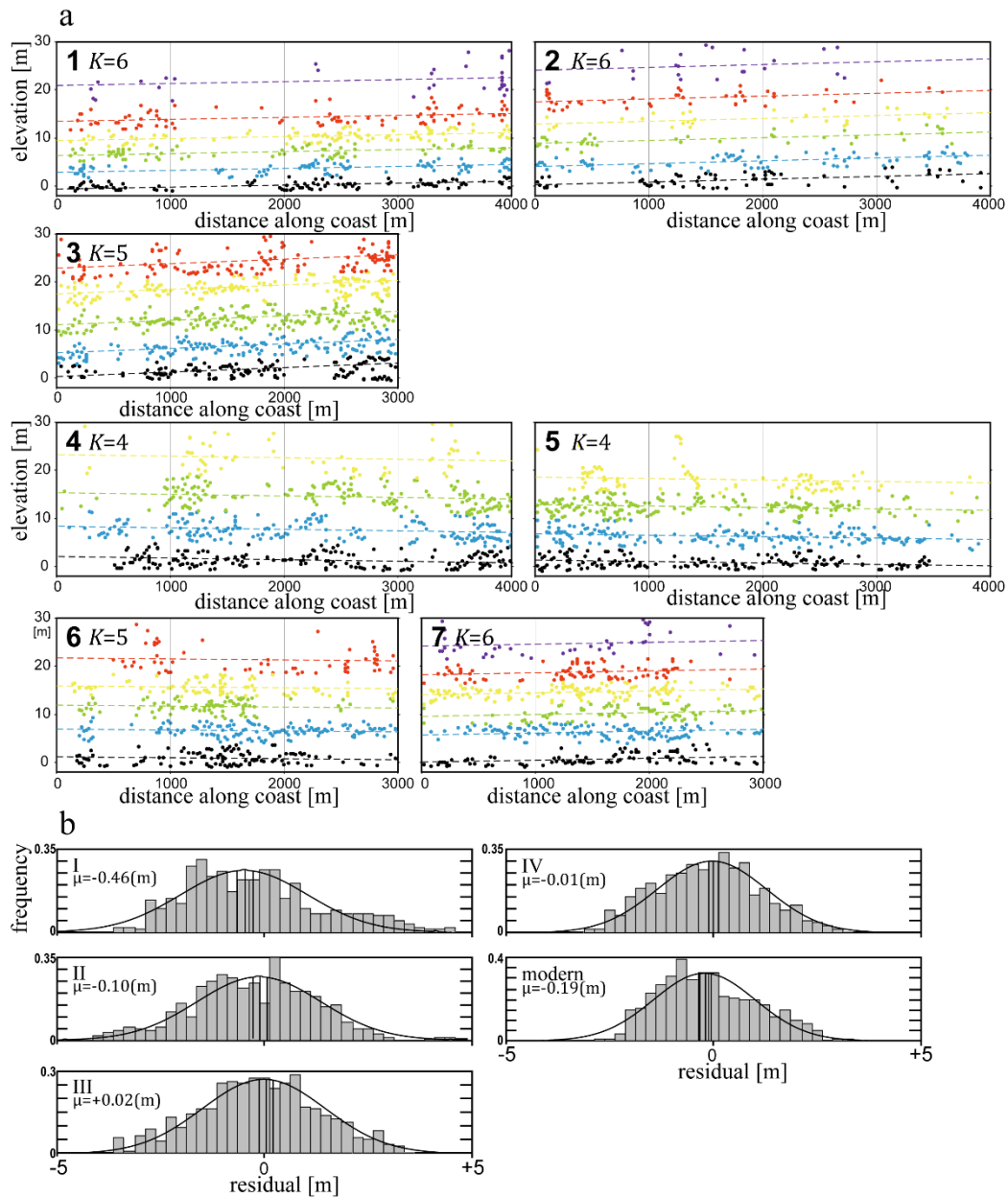
Figure 2-4. (a) Classification results of terraces for all seven analysis sections. The upper left numbers correspond to the section numbers, and the directions of distance along coast are indicated by arrows in Figure 2-1. K is the adopted number of clusters. The dots represent the elevations of extracted cliff bases, and the color corresponds to the classified cluster. (b) Histograms of the distance between each cluster point and the center line. The solid curves indicate the best-fit normal distribution with the median μ shown in the left.

of the sections. Note that 0 m a.s.l. indicates the mean sea-level, and the operation of LiDAR was at the timing of low-tide, and thus the shoreline landform approximately one meter below sea-level is included. The clustering was conducted independently between the sections. The numbers of clusters were determined by the elbow method to be 6, 6, 5, 4, 4, 5, and 6 for sections 1 to 7, respectively.
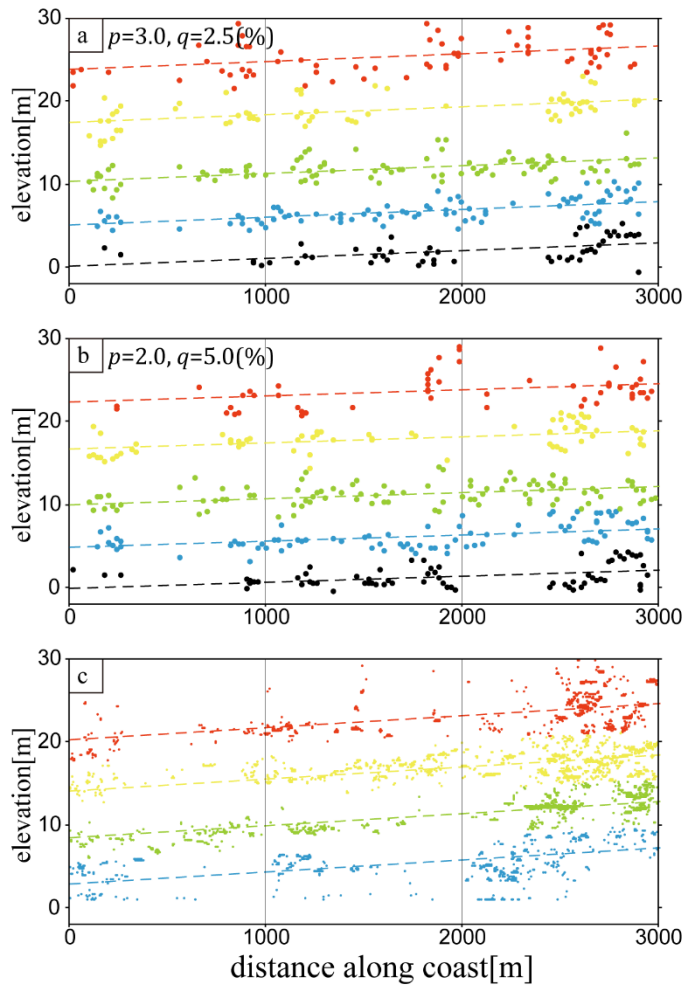
Figure 2-5. Classification results of terraces with different extraction parameters in section 3. The dots represent the positions of the extracted points in each criteria and the dashed lines are the center lines of the clusters as in Figure 2-2d. (a) The search radius p is 1.5 times multiplied. The number of extracted points is 405. (b) The threshold angle q is two times multiplied. The number of extracted points is 370. (c) The result using gradient as the extraction threshold. The surface points whose maximum gradient value is lower than 1.0 (%) are extracted from 4.0 m grid DEM. The number of extracted points is 5851.

Figure 2-4b presents the histogram of the residual vertical distance of each cluster point from the nearest point of the centerline for the lower five clusters in all sections. The histograms are well fitted by the normal distributions (the black curves) with a negligibly small shift of the median, confirming the adequateness of the obtained clustering results. If the number of clusters was insufficient, I observed multiple prominent peaks in the histograms. If the data points were randomly distributed without clustered features, the histograms showed a uniform distribution.

2.3.2 Robustness of the clustering

Next, I evaluate the robustness of the obtained clustering results. Herein, I used two parameters for the extraction of the cliff basements, p and q, as illustrated in Figure 2-2a. The number of extracted points changes according to the parameter values selected, so I first test how the clustering results change depending on them.

The original values for parameters p and q are 2.0 and 2.5(%). Figures 2-5a and 2-5b show the results of the classification when parameter p is changed to 3.0 and

parameter q to 5.0 (%), respectively. Although approximately 400 points are extracted in both cases, which is nearly half the number of the original parameter settings, the results of the clustering did not differ so much from the original one, particularly the elevation and tilt of the centerlines. One significant change is that the highest cluster in Figure 2-5a has an elevation that is approximately 1 m higher than those under the other two parameter sets (Figure 2-2d and 2-5b). This shift might be caused by contamination from background noise because larger values of p tend to pick up irrelevant cliffs in the back hill higher than the highest terrace, and the highest cluster can include all points above it. This contamination can be prevented by selecting adequate parameter values
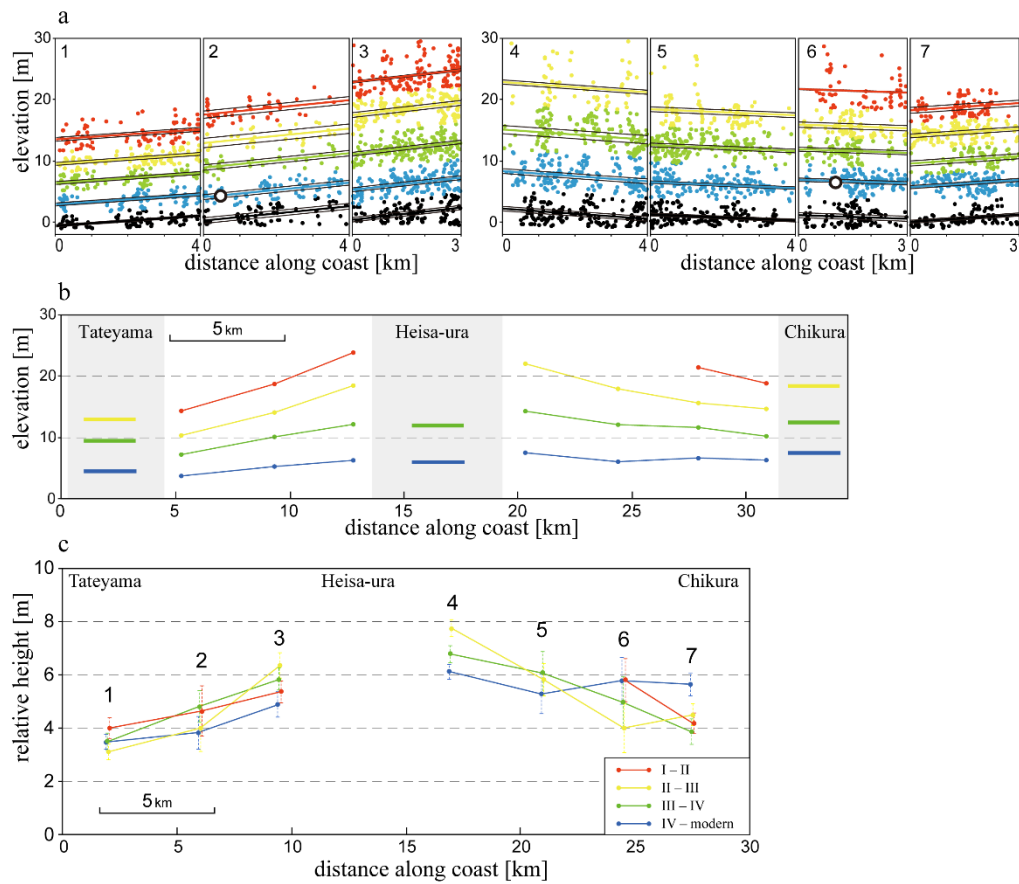
Figure 2-6. (a) Distribution of the center lines of the clusters. The numbers on upper left indicate the section number (Figure 2-1). Black lines indicate 2σ interval of each cluster estimated by 10,000 times bootstrapping. Open circles are the elevations of fossilized sessile assemblages indicating the mean sea level just before the 1703 event (Kayanne and Yoshikawa, 1986; Shishikura et al., 2014b). (b) Elevation distribution of the Numa terraces connecting the center point of each analysis section. The horizontal bars are the elevations of the detected abandoned dunes in the following analysis (Figure 2-7). (c) Relative height distribution of the Numa terraces, represented by the midpoint of each section. The error bars indicate 2σ intervals calculated from the elevation estimation of each paleo-shoreline angle (Figure 2-6a).

28

that comprise the target scales of the signals by filtering out noises, considering the band-pass nature of these parameters.

Next, to confirm the general applicability and stability of the proposed method, I test another type of characteristic geometry to be targeted. Here, I extract flat surfaces from the DEM dataset, apart from the above cliff bases, and apply the clustering in the same way. I initially down-sampled the original 0.5 m grid DEM dataset into a 4-m mesh for data-size reduction and smoothing and calculate the steepest gradient value over the area. I applied some threshold to this gradient map to extract the location with a gradient value lower than that. I then produced the plot of the elevations and the along-coast distance of the extracted locations, as shown in Figure 2-5c for section 3, using the threshold value for the slope of 1.0 (%). I confirmed that our method successfully clustered these extracted features, as shown by the colors. Note that the number of clusters is found optimal to be four because the counterpart of the lowest cliff base (Figure 2-5d) is the modern platform in this analysis and is hidden below the sea level here. The centerlines are 2–3 m lower than those obtained using cliff bases, as consistent with the general feature of marine terrace surfaces that dips down toward coastlines from the corresponding paleo-shoreline angles. This result demonstrates the robustness of the clustering method independent of the type of geometric features as long as it is related to the terrace landform. Moreover, the examination result with the down-sampled elevation data indicates that this method is likely applicable using the open data such as provided by GSI in Japan (5–10 m grid), by USGS in the US (5 m grid), and ASTER GDEM covering the whole Earth surface (15 m grid), as long as the resolution is sufficiently smaller than the platform width.

2.3.3 Connection between sections

Next, I consider the connection of paleo-shoreline angles of the same generation using the clustering results for the seven sections (Figure 2-4a). As a result of the elbow method, the number of clusters is obtained to be 4–6. Figure 2-6a shows the set of centerlines for each cluster in each section. This result indicates that the lower four levels, which appear in all seven sections, can be interpreted to be connected consistently (except for the gaps between the sections discussed below) along the whole coast in the study area. On the other hand, the fifth level from the bottom is not extracted in sections 4 and 5. However, because the distribution and its relative height from the fourth level are comparable in the east and west parts, we can interpret them to constitute a single paleo-shoreline angle generation. The reason why the fifth level is not extracted there is unclear, but it might be related to what this high and old terrace was degraded much, suffered from

29

erosion and sedimentation. Conversely, the sixth level is less reliable because it is extracted in only limited sections, and its elevation is inconsistent. I suspect that this level is the eroded back hill above the highest paleo-shoreline angle. As noticed above, the alignment of the centerlines shows certain amounts of gaps between each section in elevation, and they become the largest in the highest and the lowest levels. This tendency is understandable as the repercussion of the assumption of parallel centerlines that caused the slopes of the centerlines to be the average of all levels. Regardless of the existence of the gaps, the elevations at the middle points of the lines in the analysis sections can still be used as their averages robustly. Thus, in this study, I consider these average values as the elevations of the paleo-shoreline angles of each section, as shown in Figure 2-6b. Remarkably, independently classified paleo-shoreline angles in each section show consistent distributions of the four levels. The three levels of paleo-shoreline angles are identified along the entire coast (the lowest line in Figure 2-6a corresponds to the modern shoreline) and one level that is lacking in some sections. These four levels exactly match with the previously identified four Numa terraces. The lowest line, corresponding to the modern shoreline, is positioned few meters above the mean sea level in sections 2 and 3 (Figure 2-6b), which might be affected by the uplift due to the 1923 event prominent in this area (Figure 1-2a).

Figure 2-6c shows the relative height distributions between each level. Each distribution shows a similar trend that takes peak value in section 4 and decreases toward the north. The relative height between Numa IV and the modern level (likely includes the 1923 uplift) is slightly different from the higher levels that the peak height is approximately 2 meters lower than that between II and III, and the change in relative height is not significant in the eastern coast (sections 4–7).

2.3.4 Accuracy of paleo-shoreline angle elevation values

I evaluate the accuracy and precision of the elevations of the paleo-shoreline angles. The histograms in Figure 2-4b illustrate the distributions of the distance between each cluster point and the centerline for the lower five cluster levels (including the lowest one, the modern coastline). The histograms show approximately symmetrical distributions, and the standard deviation becomes larger for the clusters at higher elevations, maintaining the shape of the normal distributions. Moreover, I evaluate the confidence intervals of the obtained average elevation μ by the bootstrapping method. Evaluated by 10,000-times bootstrapping, 2σ confidence intervals of each level in each section are obtained, as indicated in Figure 2-6a. The average confidence interval in whole levels and sections is ±0.37 m for 2σ.

A type of tubeworm (*Pomatoleios kraussii*) forms sessile assemblages at the height of mean tidal sea level and is known as a reliable indicator of the past sea level, as discovered by Kayanne and Yoshikawa (1986). In Figure 2-6a, the elevations of the sessile fossil assemblages uplifted in the 1703 event are shown in sections 2 (Shishikura et al., 2014b) and 6 (Kayanne and Yoshikawa, 1986). Although a further evaluation of the spatial relationship between the sessile assemblages and the paleo-shoreline angles is needed, the match between the results of this study and the known elevation of 1703 mean sea level supports that the assumption of the paleo-shoreline angle is valid for the indicator of the past sea level.

For the accuracy to estimate the elevations, I noticed that the abovementioned increasing standard deviation is similar to the behavior of the diffusion equation, which is used to describe the topographic degradation due to erosion and deposition processes (Anderson and Menking, 1994), as discussed below. The normal distribution is the solution of the diffusion equation when the initial condition is given by the delta function, and the robe is increasing (diffusing) with time (Appendix B). This result suggests that the temporal reduction of the accuracy is inevitable but will be easily handled through the simple normal distribution. The assumption of the parallel centerlines might affect the distributions of the distance distributions of the points (Figure 2-4b). However, this effect
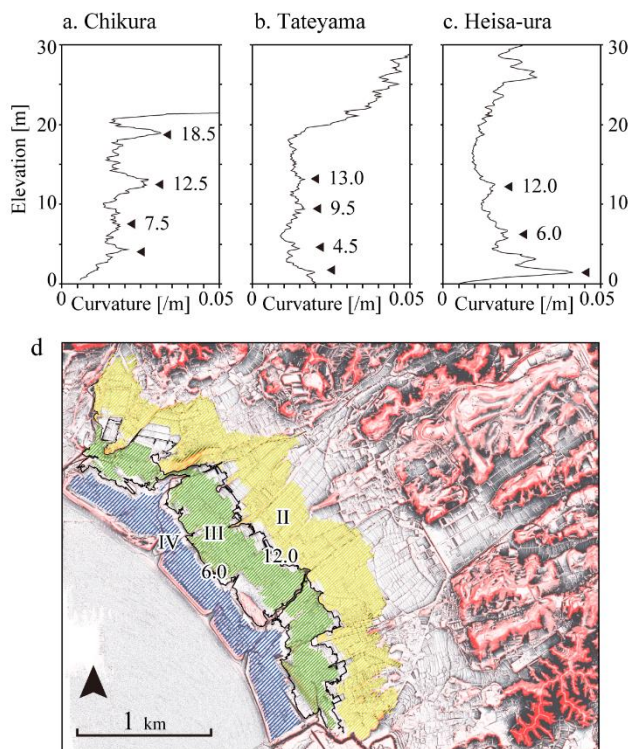
Figure 2-7. The results of the extraction of the terrace landforms in the sedimentary coasts. (a–c) The stacking results of the vertical profiles of the absolute value of curvature in (a) Chikura, (b) Tateyama, and (c) Heisa-ura. (d) Classification result of the Heisa-ura coast. The solid lines indicate the contours of the elevations along the extracted peaks from the curvature profile exemplified in (c). The circles indicate the sampling points in this study, and the colors correspond to the terrace classification.

31

is supposed to be larger at the upper and lower clusters and can be considered to be smaller than the weathering.

2.3.5 Classification in the Heisa-ura lowland

Before analyzing the terrace classification in Heisa-ura, I compare the results of the stacked profiles to the already classified marine terraces in Chikura and Tateyama for the validity examination of the method. Figures 2-7a and b show the stacking results of the vertical profiles of the absolute value of the curvature in Chikura and Tateyama, respectively. Several peaks can be seen in the vertical profiles. The elevations of these peaks correspond to the coastal side of the abandoned dunes in Chikura and Tateyama (Figure 2-1), and it suggests that these peak points can be used as the indicator of the terrace boundary. Note that these indicated elevations correspond to terrace boundaries, not paleo-shoreline angles discussed above, which directly relate to the past mean sea-level.

Figure 2-7c shows the stacked vertical profile of the absolute value of the curvature in Heisa-ura, where the surficial landform is less evident than in the other two coasts. Three prominent peaks can be seen in the vertical profile. Figure 2-7d shows the map of the Heisa-ura coast with contour lines of these peaks. The lower two peaks, around 1.5 m a.s.l. and around 6 m a.s.l., corresponding to the previously recognized modern and Numa IV dunes. The third peak, around 12 m a.s.l, is not previously recognized as the landform boundary. However, looking into the landform around this elevation in detail, several small bumps can be seen arranging along the coastline, and likely indicates the abandoned dune of Numa III. On the other hand, any higher peak than Numa III is not apparent in the vertical profile (Figure 2-7c), which might correspond to the boundary between Numa I and II. The elevations of these detected terrace boundaries are shown in Figure 2-6b for the comparison with the results in the rocky coast.

2.4 Geomorphic and tectonic implications

2.4.1 Determination of the distribution of the Numa terraces

As a result of the preceding process, I successfully obtained the distribution of Numa terrace elevation along the 25 km of the coastline. For the first time, I quantitatively confirmed that each terrace reaches its highest elevation around Heisa-ura at the western side of section 4 (Figure 2-1), and terrace elevation decreases toward the northern part of the peninsula. Figure 2-8a is a redrawn terrace classification based on the results of this study, which shows the overall similarity with the previous map (Figure 2-1; Kawakami
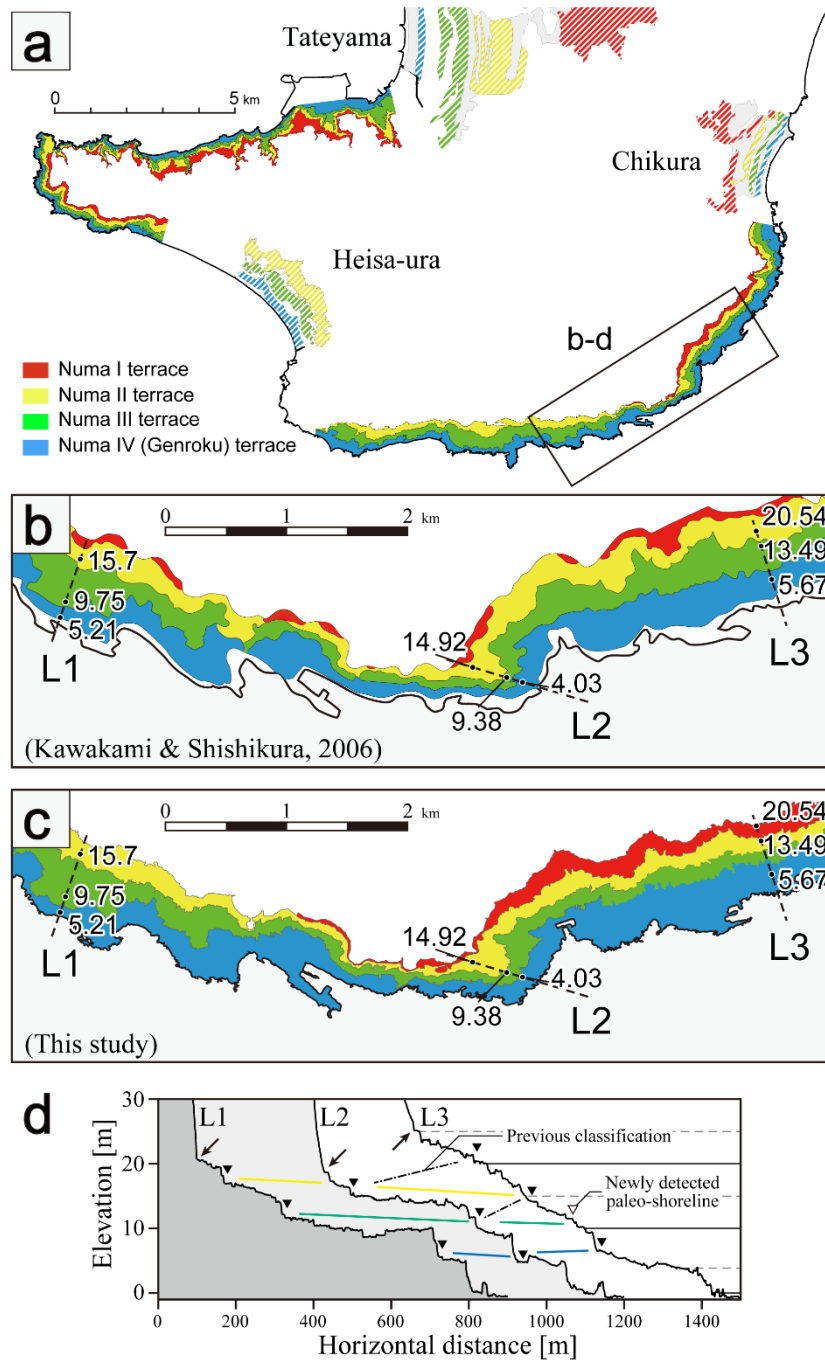
Figure 2-8. (a) Reclassification map of the Numa terraces. (b–c) Comparison with conventional Numa classification by Kawakami and Shishikura (2006) (b), updated Numa classification (c). The numbers are surface elevations along the profiles L1 to L3 indicated by black points. (d) Surface profiles along the lines L1, L2 and L3 shown in (b) and (c). Triangles indicate the positions of the paleo-shorelines. Yellow, green and blue lines connect the shoreline angles of the Numa II, III, and IV, respectively, in this study. The black chained lines indicate the previous classification. Arrows indicate the paleo-shoreline angles of Numa I in the previous studies.

and Shishikura, 2006). However, remarkable differences appear in some areas. The greatest difference is in the southeast part of the study area (Figures 2-8b–c). The paleo-shoreline of Numa III in the previous classification (Kayanne and Yoshikawa, 1986;

33

Kawakami and Shishikura, 2006; Figure 2-8b) becomes that of Numa II in this study (Figure 2-8c), and the redrawn third paleo-shoreline was not drawn or was recognized as a part of terrace sequence of Numa IV. Figure 2-8d shows the surface profiles along the survey lines shown in the classification maps. In the previous classification, the elevation of Numa II was 15.7 m a.s.l. on the west side (line L1), 14.92 m a.s.l. on the center (line L2), and 20.54 m a.s.l. on the east side (line L3). This abrupt step is inconsistent with the general distribution of the Numa terraces, which gradually decrease their elevation toward the north. The paleo-shorelines of Numa II and IV are topographically prominent, but the one of Numa III in question is not obvious (white triangle in Figure 2-8d). While the previous studies, which were based on field survey and detection from aerial photography interpretation, may have overlooked this border, I have successfully uncovered the existence of a step with the statistical method. The Numa I terrace was not detected in the western part of this region (Figure 2-8c). It is possibly because the terrace corresponding to Numa I has weak lateral continuity in this region as shown in Figures 2-8b and d and not connected by the method in this study.

2.4.2 Implications for formation/degradation processes of marine terraces

The obtained quantitative results allow us to investigate the formation and degradation processes of the marine terraces through changes in some geomorphic parameters. Understanding such surficial modification processes is important for extracting primary seismotectonic information from the current coastal topography. In this section, I discuss the temporal changes in the curvatures and widths of the four levels of the terraces.

First, I consider how the curvature of the paleo-shoreline angle changes through time. Several landform degradation models have been proposed in many geomorphological studies (e.g., Anderson and Menking, 1994; Shikakura et al., 2012) because the mode of degradation can be key information for determining how long a terrace has suffered erosion and sedimentation. Figure 2-9a shows the histograms of the curvature values at the extracted cliff bases. The curvature value is calculated along with each elevation profile by $L(x) = -\big(2H(x) - H(x - r) - H(x + r)\big)/r^2$ and the search radius r is 1 (m). Figure 2-9b compiles the mean value of the curvature versus formation age of each terrace (Komori et al., 2017), which shows that the older terraces have smoother cliff bases as expected from the monotonic degradation process.

I further find that the obtained degradation curve does not contradict the theoretical expectation from the diffusion model of the degradation process (Anderson
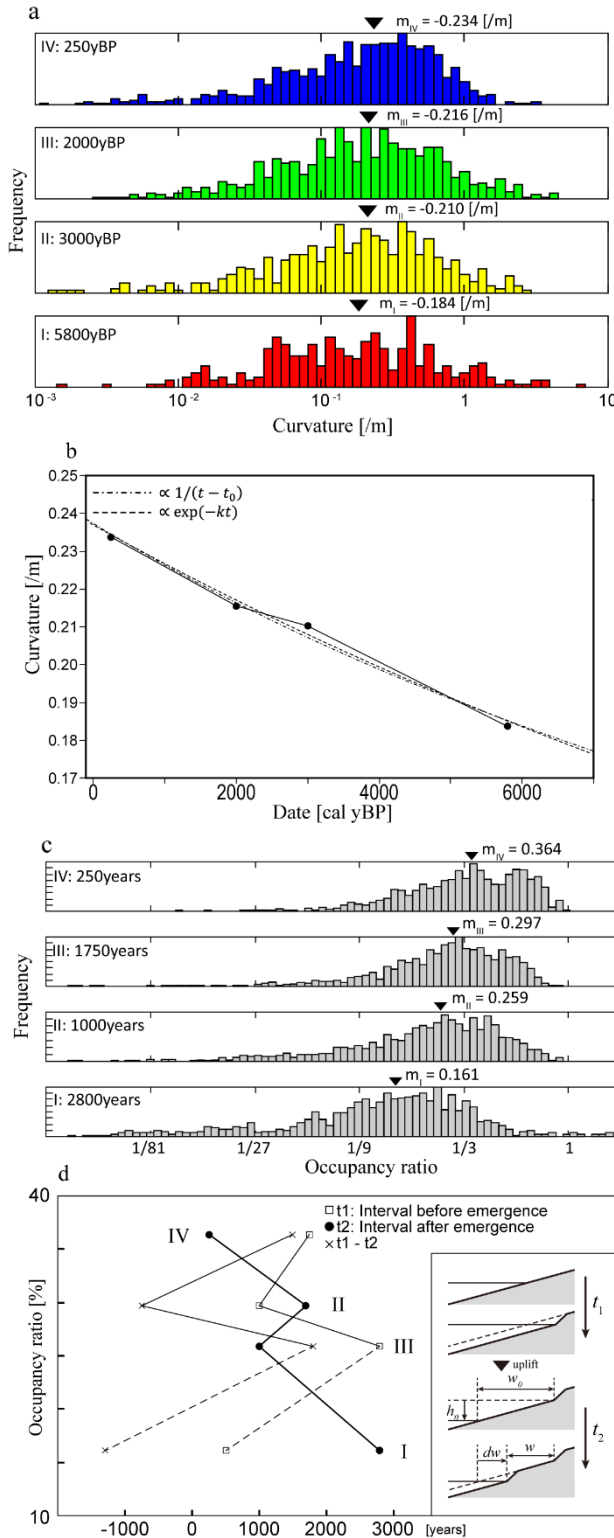
Figure 2-9. (a) Histograms of the curvature value at the extracted locations of the terrace cliffs. (b) Plots of mean value of curvature versus formation age of each terrace estimated by Komori et al. (2017). The fitted curves assume a diffusion models: $-4890.45(t + 20610)^{-1}$ (chain line), and a hypothetical one $-0.235\exp(-t/25000)$ (dashed line). (c) Histograms of the occupancy width of each platform. The horizontal axis indicates the ratio of each platform width to the total width of Numa II, III, and IV. The triangle above each histogram indicates the mean value. (d) Plots of occupancy ratio versus interval times between terrace formations. Solid circles, open squares, and crosses indicate the plots for the interval time before its emergence (t_1), after its emergence (t_2), and the difference between them ($t_1 - t_2$), respectively. The interval time of Numa I before its emergence is not revealed but we temporarily adopt 500 years based on Komori et al. (2017) and connect it by dashed lines. (inset) Schematic illustration of the relationship between the interval times t_1 and t_2, uplift amount h_0, and the original platform width just after the uplift w_0, denudation length dw, and the final platform width w.

and Menking, 1994). As detailed in Appendix B, the curvature of a cliff base is predicted to be decreased at 1/t as increasing time t governed by the diffusion equation $\partial u(t,x)/\partial t = \kappa\,\partial^2 u(t,x)/\partial x^2$, where u denote the elevation of the ground surface at

time t and location x, and κ is the diffusion coefficient. The $1/t$ curve can fit the obtained data points in Figure 2-9b, but, so far, the number of data points and temporal extent seems to be too small to eliminate the possibility of the other hypothetical candidate curves.

It will be possible to obtain additional data from other coasts to precisely determine the degradation curve. While the degradation speed should depend on the environments of the coasts, such as the climate, lithology, and the type and thickness of cover sediment, I anticipate that common features of the decaying mechanism throughout various types of the coast can be revealed by compiling the degradation curve from many sites with substantial variation in such conditions. The current result raises an expectation that, by determining the general relationship between the formation ages and the decay in curvature, the curvature could be used to infer the formation age of marine terraces in difficult circumstances of retrieving dating samples.

Next, I also compiled data on the width distribution of the terrace platforms. The models for the formation process of marine terraces have been discussed (Uesawa and Miyakawa, 2015; Noda et al., 2018), but the critical factor determining the shape of terraces is still unknown. If an empirical relationship between the formation history and terrace morphology becomes clear, it possibly advances such model studies. I attempt here to provide more direct observed data to correlate the terrace landform with the formation interval time to constrain the formation process of the marine terraces.

Figure 2-9c shows the histograms of the platform widths of the marine terraces sampled at the interval of 20 m along-coast in the entire survey region. The width of the platform is expressed here as the horizontal distance from a certain paleo-shoreline to the paleo-shoreline one step below. The horizontal axis is the ratio of the width of each platform level to the sum of the width from Numa II to IV in each profile, termed the occupancy ratio. If the terrace platform widens, the peak of the histogram will be located toward the right side. Figure 2-9c demonstrates that Numa II and III have comparable platform widths, the width of the platform of Numa I is approximately half of those of II and III, and the platform of Numa IV is as much as twice the width of II and III. Figure 2-9d shows the relations of the occupancy ratio of each terrace with the intervals before (t_1) and after (t_2) its emergence and that with the difference between them ($t_1 - t_2$). Comparing these results indicates that the platform width correlates with the time taken for the formation of the next platform rather than that of itself. To put this another way, the longer the time elapsed after a terrace uplifted (t_2), the narrower the platform becomes.

The above-observed relationship provides an essential constraint for the formation processes of marine terraces. It might be surprising if the widths of the marine terraces are irrelevant to the time (t_1) taken to be formed due to the coastal denudation, given our intuition and predictions of theoretical erosion and degradation models (Anderson and Menking, 1994; Trenhaile, 2000; Uesawa and Miyakawa, 2015; Noda et al., 2018). However, we are able to develop a possible simple scenario explaining this observed relationship, as schematically illustrated in the inset of Figure 2-9d with a sectional view of terrace development. Initially, the coastal landform is characterized as the slope face. During the period of t_1 before the uplift, I assume that the slope is denudated monotonically below sea level to some depth extent, resulted in the retreated face with almost keeping the slope angle. Here, note that the absolute amount of denudation does not play an important role because of the monotonic denudation over the depth. Next, the uplift generates the original platform width w_0, which is primarily determined by the amount of the uplift h_0 and the slope angle, not by the time of denudation, t_1. During the period of t_2 after the uplift, the original platform is denudated for the width dw in the same manner, leaving the final platform width, w. This sequence leads to the relationship $w(t_2) = w_0 - dw(t_2)$, where w_0 are a time-independent constant, and w and dw correlate with t_2 without t_1. This interpretation requires the slope face continuing offshore, subsequently emerging as the terrace platforms; indeed, such a slope is found in our targeted area (see Figure 2-2a). As I explored a similar example in the well-examined Holocene marine terraces in northeast New Zealand (Berryman et al., 2018; Litchfield et al., 2020), I speculate that the observed relationship perhaps has some generality (see Berryman et al. (2018) for the time interval after the emergence (t_2) of a wide platform being qualitatively shorter in the comparison between the terraces T2 and T3).

I demonstrate that the current method, together with the accurate dataset of the topography and ages in the Boso Peninsula area, allows us to test the models of the terrace formation process quantitatively and derive a key ingredient. These quantitative results imply that the cliff curvatures and the platform widths possibly contain the information of the ages and magnitudes of the uplift events, overprinted by other effects. While the speeds of the degradation and denudation should depend on the environments of the coasts, such as the climate, lithology, and the type and thickness of cover sediment, I anticipate that generality and individuality of the terrace formation mechanism can be revealed by extensive analyses for many other sites in the current direction. Understanding these geomorphological processes may help generate new information bearing upon tectonic processes.

2.4.3 Distribution of the Numa terraces around Heisa-ura

Furthermore, I discuss the distribution of the Numa terraces in Heisa-ura classified in this study. The terrace boundary elevations obtained in Heisa-ura are approximately comparable to but slightly lower than the adjacent rocky coast (Figure 2-6b). It should be noted that the extracted elevations in the sedimentary lowlands are not paleo-shoreline angles but the averaged positions of terrace cliffs; thus, they should be slightly higher than the positions of paleo-shoreline angles (Figure 2-3) as the results in Chikura and Tateyama lowlands (Figure 2-6b). However, following the discussion of Komori et al. (2017), because the surface elevation of the sedimentary lowland could suffer from non-tectonic subsidence due to the compaction of underground sediments, the observed elevation difference between rocky coast and sedimentary coast is not inconsistent.

3. Reevaluation of the Numa terrace formation ages

3.1 Introduction: Dating survey of marine terraces

The formation ages of marine terraces are often estimated by the dating survey of uplifted coral reefs (Sieh et al., 1999; Wang et al., 2013), terrace deposits (Komori et al., 2017; Berryman et al., 2018), and covering tephra deposits (Berryman, 1993). The available types of dating methods depend on the coastal environment and constrain the available analyzing methods. For example, although tephra deposits can constrain the date of sediment layers accurately, the occasion is quite limited and infrequent. Likewise, the coral reefs enable highly accurate in-situ dating, but the habitat is limited in the warm coastal environments. The terrace deposits, marine sediment layer deposited before the emergence, are datable via the radiocarbon method by measuring the buried shell fossils or other organic materials. Such deposits are not specific compared with the coral reefs and tephra deposits, and thus the dating is possible under broader circumstances. However, the fossils buried in sediment should have suffered the reworking effect to some extent, which is the re-deposition of the body of the organisms away from its habitat (Komori et al., 2017). Therefore, the dating results of the buried fossils do not directly indicate the emergence age of the marine terrace, and thus it is required to interpret the relation between them. The previous studies have usually assumed that the youngest dated fossil of marine organisms produced from a terrace deposit constrains the older limit of the emergence age because the younger materials basically cannot contaminate the older sediment (Nakata et al., 1980; Komori et al., 2017; Berryman et al., 2018). This assumption can provide a reasonable estimation of the emergence history of the marine terraces but allows indeterminate estimation errors because it does not provide the younger estimation limit of the emergence age.

For the geological investigation, I raised the quantity of the dataset valuable to improve the robustness of the age estimation of past earthquakes. I collected 319 radiocarbon-dated marine and terrestrial samples in total, where I added 56 samples newly in this study, 182 samples from the published datasets dated using the AMS, which applied the δ13C correction (Fujiwara et al., 1999; 2006; 2010; Ishida et al., 2002; Shishikura et al., 2005; 2014; Uno et al., 2007; Komori et al., 2017), and 81 samples before the application of δ13C correction (Fujiwara et al., 1997; Nakata et al., 1980). These samples are mainly from the three broad sedimentary lowlands; Chikura, Tateyama,
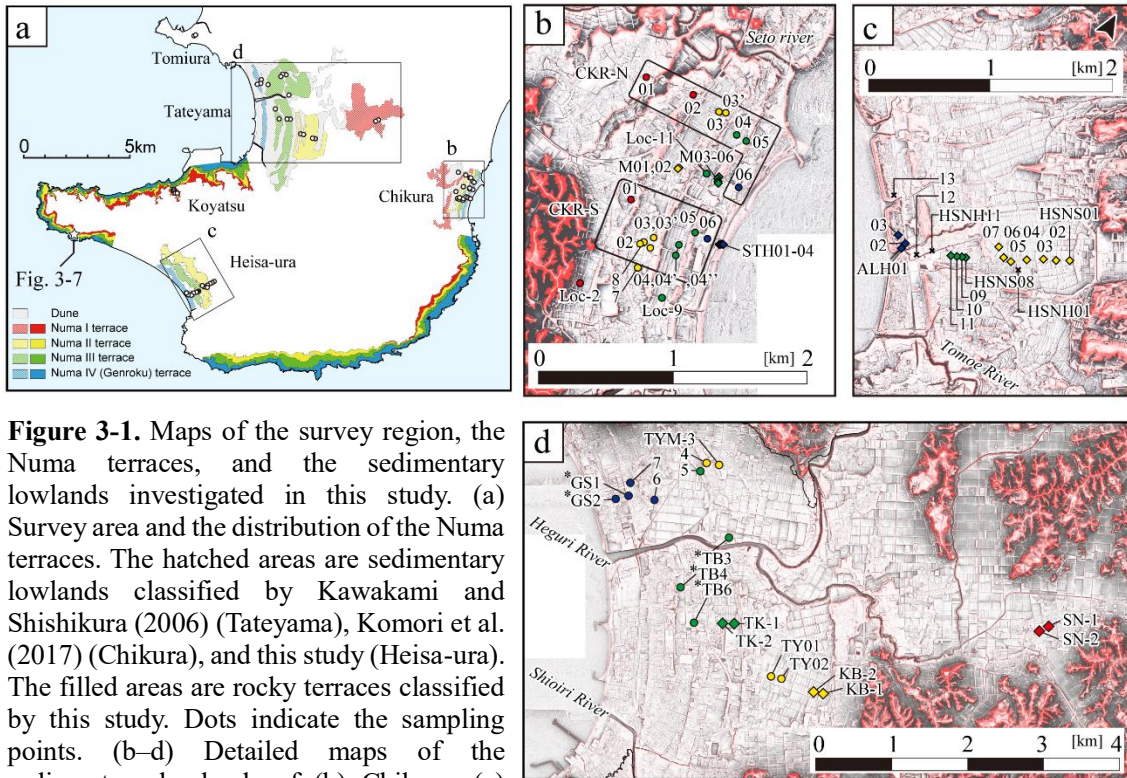
Figure 3-1. Maps of the survey region, the Numa terraces, and the sedimentary lowlands investigated in this study. (a) Survey area and the distribution of the Numa terraces. The hatched areas are sedimentary lowlands classified by Kawakami and Shishikura (2006) (Tateyama), Komori et al. (2017) (Chikura), and this study (Heisa-ura). The filled areas are rocky terraces classified by this study. Dots indicate the sampling points. (b–d) Detailed maps of the sedimentary lowlands of (b) Chikura, (c) Heisa-ura, and (d) Tateyama, colored by red relief image map (Chiba et al., 2008). Circles and diamonds indicate the sampling points of the previous studies (Fujiwara et al., 1999; 2006; 2010; Shishikura et al., 2005; 2014; Komori et al., 2017) and this study, respectively, and the color corresponds to the terrace level. Sampling points marked with an asterisk are where tsunami deposit layers are in the sediment.

and Heisa-ura (Figure 3-1b). Of these datasets, 277 samples are marine organisms. Based on the location and the sediment structure, 63 samples of them are reported to be included in tsunami deposits (Fujiwara et al., 1997; 2006).

To eliminate the subjectivity in estimating the emergence ages of the marine terraces from the dating results, I propose a new inversion method considering the sedimentation process of terrace deposits. I formulated a model of the sedimentation and reworking process in the shoreface deposits and assumed frequency distribution, which represents the distribution of the sediment ages within each terrace deposit with the emergence ages as the model parameters. Then, I estimated the emergence ages of the terraces along with their confidence intervals via a Bayesian approach. I conducted the Bayesian inversion utilizing Markov Chain Monte Carlo (MCMC) method (MacKay, 2003; Gamerman, 2006). This method can evaluate not only the older limits of the

40

emergence ages but also the younger limits statistically, which were a significant obstacle in the previous discussion about the paleo-earthquake recurrence.

3.2 Methods and Materials

3.2.1 Dating survey

3.2.1.1 Previous dating investigations and datasets

The Numa terraces have long been subject to geological investigations because of their prominent landform and indicative relationship with the hazard assessment. The previous research conducted various surveys, and 263 samples have been dated previously (Nakata et al., 1980; Fujiwara et al., 1997; 1999; 2006; 2010; Ishida et al., 2002; Shishikura et al., 2005; 2014; Uno et al., 2007; Komori et al., 2017). The sampling points and methods are displayed in Figure 3-1c–e and Table S1, and the details of each dated sample and measurement are listed in Table S2. The terrace levels to where each sampling point belongs follow the description by the original papers basically, but I carefully compared their positions and the terrace classification obtained in the previous section (Figure 2-8) and checked their reliability.

I select the dating result from this dataset for the following statistical analysis and eliminate a part of the dating samples which are not suitable for our purpose. First, I do not use terrestrial materials such as seeds, roots, and pieces of wood, because they have experienced different sedimentation process from the marine sediments. Second, I eliminate the materials obtained from several sampling points, which have likely suffered "backward reworking," which is contamination from the sea into the already emerged terrace platform. For example, the sampling point TB3 (Figure 3-1e) is adjacent to the river where the inundation of the past tsunami event had likely reached. As discussed below, the contamination of younger materials into the older terrace deposit can lead to severe distortion of the estimation. Therefore, I eliminate the sampling points positioned in the lowered land around the river flow or where any tsunami deposit layer is confirmed in the sediment (TB-3, 4, 6, and GS-1, 2 in the Tateyama lowland). Fortunately, the sediment structure of a terrace deposit shows a different appearance from the shoreface deposit and actively reported by the previous surveys because of its paleoseismological importance. Specifically, the dataset produced by Fujiwara et al. (1997; 1999; 2006; 2010) in Tateyama originally intended to reveal the tsunami deposit and were obtained from the river outcrops and marshy lowland. In this study, I refer to these samples only for the discussion of the correlation between them and the terrace deposit later.

Table 3-1. Sampling points and sampling methods in this study

Region	Point name	Surface elevation [m a.s.l.]	Classifi-cation	Sampling depth [m]	Longitude E°/′/″			Latitude N°/′/″			Sampling Method	# of dated samples
Chikura	CKR-M01	15.5	II	2.0	139	57	30.34	34	58	36.52	Geoslicer	1
	CKR-M02	15.5	II	1.6	139	57	30.13	34	58	36.35	Geoslicer	0
	CKR-M03	6.5	III	2.0	139	57	41.13	34	58	33.22	Geoslicer	0
	CKR-M04	6.5	III	1.7	139	57	41.05	34	58	33.58	Geoslicer	1
	CKR-M05	7.0	III	1.9	139	57	41.10	34	58	33.96	Geoslicer	0
	CKR-M06	7.0	III	1.4	139	57	41.22	34	58	34.33	Geoslicer	0
	STH01	4.60	IV	1.8	139	57	41.78	34	58	19.29	Geoslicer	3
	STH02	4.42	IV	1.8	139	57	42.00	34	58	19.28	Geoslicer	2
	STH03	4.34	IV	1.8	139	57	42.22	34	58	19.27	Geoslicer	2
	STH04	4.31	IV	1.6	139	57	42.58	34	58	19.24	Geoslicer	1
Tateyama	SN-1	18.50	I	6.0	139	55	2.40	35	0	11.38	Machine Coring	2
	SN-2	18.25	I	6.0	139	54	57.79	35	0	9.47	Machine Coring	2
	KB-1	15.09	II	6.0	139	53	12.95	34	59	44.62	Machine Coring	2
	KB-2	13.30	II	6.0	139	53	8.24	34	59	45.33	Machine Coring	2
	TK-1	7.40	III	6.0	139	52	29.76	35	0	12.45	Machine Coring	2
	TK-2	5.66	III	6.0	139	52	24.06	35	0	12.64	Machine Coring	2
Heisa-ura	HSNS01	21.51	II	1.5	139	50	17.45	34	56	21.52	Geoslicer	0
	HSNS02	19.54	II	1.8	139	50	13.95	34	56	19.71	Geoslicer	1
	HSNS03	18.63	II	1.6	139	50	10.38	34	56	18.42	Geoslicer	0
	HSNS04	16.59	II	1.3	139	50	6.12	34	56	16.25	Geoslicer	1
	HSNS05	14.56	II	1.1	139	50	2.24	34	56	13.89	Geoslicer	2
	HSNS06	13.95	II	1.8	139	49	59.73	34	56	13.84	Geoslicer	2
	HSNS07	13.37	II	1.2	139	49	56.76	34	56	15.52	Geoslicer, Handauger	2
	HSNH01	15.18	II	1.5	139	50	5.50	34	56	12.96	Handauger	2
	HSNS08	8.93	III	1.1	139	49	50.54	34	56	7.50	Geoslicer	1
	HSNS09	7.94	III	1.3	139	49	49.64	34	56	7.25	Geoslicer	2
	HSNS10	7.63	III	1.3	139	49	48.24	34	56	6.73	Geoslicer	2
	HSNS11	7.32	III	1.3	139	49	46.64	34	56	6.16	Geoslicer	2
	HSNH02	6.3	IV	1.5	139	49	41.4	34	56	4.9	Handauger	2
	HSNH03	3.5	IV	1.5	139	49	38.0	34	56	1.8	Handauger	1
	ALH01	3.21	IV	1.6	139	49	32.14	34	56	2.40	Geoslicer	4
	ALH02	3.14	IV	1.5	139	49	32.61	34	56	2.86	Geoslicer	3
	ALH03	2.68	IV	1.8	139	49	29.24	34	56	5.11	Geoslicer	4
	HSNH15	3.5	IV	1.8	139	49	22.6	34	56	12.0	Handauger	1

3.2.1.2 Sampling in this study

In this study, I conducted an additional sampling and dating survey. The sampling points and methods are displayed in Figure 3-1b–d and Table 3-1. For sediment sampling, I used ~6 meters' depth drilling survey by machine coring (c.f., Komori et al.,

42

2017), ~2 meters' depth Geoslicer survey using handy Geoslicer (Nakata and Shimazaki, 1997; Takeda et al., 2002), and ~1-meter depth hand auger survey depending on the sampling depth of the objective sedimentation layers. The new investigations were in three sedimentary coasts: Six drilling surveys in Tateyama, 14 Geoslicer surveys and four hand-auger surveys in Heisa-ura, and 10 Geoslicer surveys in Chikura. I examined the sedimentation structures from the obtained sediment samples, and the dating samples were collected from marine sand layers deposited before the emergence of the terrace.

In Tateyama, two drilling surveys in each terrace platform except for Numa IV were conducted: SN-1, 2 on Numa I, KB-1, 2 on Numa II, and TK-1, 2 on Numa III (Figure 3-1e). The sampling depth is 6.0 meters for every point. In Chikura, I obtained approximately two meters' depth sedimentation samples from 10 survey points, two points on Numa II (CKR-M01 and M02), four points on Numa III (CKR-M03–M06), and four points on Numa IV (STH-01–04), by using the handy Geoslicer. In Heisa-ura, I obtained sedimentation samples via the Geoslicer survey from 7, 4, and 3 points on Numa II, III, and IV, respectively. Besides, I obtained sedimentation samples using hand-auger sampling from one and three points on Numa II and IV, respectively.

The samples for dating measurements are listed in Table 3-2. In addition to the newly obtained sediment samples, two shell fossils from previously obtained sediment samples in Chikura (Komori et al., 2017) were dated. Radiocarbon dating was performed using Single Stage AMS at Atmosphere and Ocean Research Institute, the University of Tokyo (Yokoyama et al., 2010), and at Beta Analytic Inc.

3.2.1.3 Dating correction and calibration

The radiocarbon measurement using AMS also enables the counting of δ13 C and correction of the effect of mass fractionation (Stuiver and Braziunas, 1993). Because the general utilization of this method was after the 1980s, the beginning study of the Numa terraces (Nakata et al., 1980) contains much more uncertainty compared to the recent ones. In this study, I use this dataset only for reference by artificially correcting using the mean δ13 C value in the study region as applied by Fujiwara et al. (1999).

I calibrated the radiocarbon ages via the Marine 20 curve of Heaton et al. (2020) with the Oxcal program v. 4.4 (Ramsey, 2009). Although the previous dataset (Fujiwara et al., 1999; 2006; Shishikura et al., 2005; 2014; Komori et al., 2017) has been already calibrated, I recalculated their radiocarbon ages from the reported δ13 C corrected ages using the same marine reservoir correction (ΔR) value for the consistency through the dataset. The radiocarbon ages are given as probabilistic density functions presented in

calibrated years before present (cal yBP), defining CE 1950 as 0 yBP. The ΔR is set to be -150 ± 50 years by reevaluating the results of Shishikura et al. (2007) and Komori et al. (2017). The evaluation of ΔR is described in Appendix C.

3.2.2 Inversion analysis of terrace emergence ages

In the conventional methods, the formation ages of each terrace were estimated as that the youngest dated sample in each terrace deposit represents the older limit of the emergence age (Nakata et al., 1980; Komori et al., 2017). However, this method cannot constrain the associated younger limit, and the estimation is usually determined by only one sample for each level despite the number of available data of more than two hundred samples. The previous methods had neglected the older dated samples because they have

Table 3-2. Dating results of this study

Region	Sample_name	Core_name	Elevation (m a.s.l.)	material	Level	14C age		Calibrated age (95.4 % c.i.)*		
Chikura	N06210	CKR-N06	1.7	shell	IV	1630	±30	1330	-	994
	S06278	CKR-S06	1.1	shell	IV	1640	±30	1340	-	1003
	M01153	CKR-M01	14.0	shell	II	5139	±27	5631	-	5285
	M04155	CKR-M04	5.0	shell	III	2568	±22	2455	-	2049
	STH01085A	STH01	3.8	shell	IV	8509	±38	9366	-	8926
	STH01085B	STH01	3.8	shell	IV	777	±40	535	-	203
	STH01150	STH01	3.1	shell	IV	8220	±30	8971	-	8531
	STH02090	STH02	3.5	shell	IV	9594	±42	10721	-	10247
	STH02120	STH02	3.2	shell	IV	2410	±23	2281	-	1871
	STH03155A	STH03	2.8	shell	IV	695	±43	485	-	111
	STH03155B	STH03	2.8	shell	IV	548	±30	299	-	modern
	STH04080	STH04	3.5	shell	IV	769	±32	524	-	203
Tateyama	SN0101	SN01	16.8	plant	I	5080	±40	5918	-	5730
	SN0102	SN01	15.6	shell	I	6280	±40	6906	-	6476
	SN0201	SN02	16.0	plant	I	5640	±40	6495	-	6310
	SN0202	SN02	14.6	shell	I	5730	±40	6280	-	5907
	KB0101	KB01	13.4	plant	II	3500	±30	3868	(0.8)	3861
								3851	(93.6)	3691
								3658	(1.0)	3650
	KB0102	KB01	11.3	shell	II	4300	±30	4655	-	4195
	KB0201	KB02	11.4	plant	II	7450	±40	8357	-	8184
	KB0202	KB02	10.2	shell	II	4070	±30	4351	-	3902
	TK0101	TK01	5.3	plant	III	2570	±30	2757	(73.0)	2698
								2635	(6.9)	2615
								2588	(15.6)	2518
	TK0102	TK01	4.4	shell	III	3700	±30	3840	-	3435
	TK0201	TK02	3.2	shell	III	3420	±30	3480	-	3088
	TK0202	TK02	0.2	shell	III	4080	±30	4365	-	3915

Table 3-2 (continued)

Heisa-ura	SNS06150	HSNS02	18.0	shell	II	3861	±36	4072	-	3625
	SNS08038	HSNS04	16.2	shell	II	6810	±30	7439	-	7089
	SNS01050	HSNS05	14.1	shell	II	4800	±30	5275	-	4853
	SNS02045	HSNS05	14.1	shell	II	5350	±30	5885	-	5508
	SNS10100	HSNS06	12.9	shell	II	4120	±30	4405	-	3971
	SNS11065	HSNS06	13.3	shell	II	5060	±30	5575	-	5195
	SNH02100A	HSNS07	12.4	shell	II	5300	±30	5842	-	5455
	SNH02100B	HSNS07	12.4	shell	II	4610	±30	5037	-	4591
	SNH01050A	HSNH01	14.7	shell	II	4180	±30	4495	-	4057
	SNH01050B	HSNH01	14.7	shell	II	3890	±30	4100	-	3661
	SNS16080	HSNS08	8.1	shell	III	7364	±28	7953	-	7619
	SNS12060	HSNS09	7.3	shell	III	7471	±25	8060	-	7703
	SNS13060	HSNS09	7.3	shell	III	8011	±29	8659	-	8286
	SNS15060	HSNS10	7.0	shell	III	2462	±30	2320	-	1928
	SNS14070	HSNS11	6.6	shell	III	3663	±26	3803	-	3399
	SNS15050	HSNS10	7.1	shell	III	3293	±32	3347	-	2934
	SNS14085	HSNS11	6.5	shell	III	4495	±29	4855	-	4451
	SNH11020	HSNH02	3.8	shell	IV	7341	±35	7936	-	7596
	SNH11100	HSNH02	3.0	shell	IV	3588	±45	3720	-	3284
	SNH12050	HSNH03	3.5	shell	IV	4031	±55	4334	-	3827
	HSU01120	ALH01	2	shell	IV	4370	±30	4770	-	4310
	ALH01120	ALH01	2	shell	IV	6114	±47	6710	-	6299
	ALH01140	ALH01	1.8	shell	IV	892	±23	624	-	319
	ALH01150	ALH01	1.7	shell	IV	983	±36	698	-	411
	ALH02080	ALH02	2.3	shell	IV	817	±38	560	-	250
	ALH02120	ALH02	1.9	shell	IV	644	±36	441	-	56
	ALH02130	ALH02	1.8	shell	IV	4555	±32	4954	-	4524
	ALH03110A	ALH03	1.6	shell	IV	10361	±41	11844	-	11291
	ALH03110B	ALH03	1.6	shell	IV	9440	±32	10518	-	10118
	ALH03135	ALH03	1.3	shell	IV	8926	±30	9840	-	9426
	ALH03165	ALH03	1	shell	IV	9122	±32	10130	-	9630
	HSU03180	HSNH15	1.7	shell	IV	4480	±30	4841	-	4441

＊ parenthetic numbers indicate probability of each interval

been "reworked" and have no information about the emergence ages. However, the reworking process also depends on the sedimentation environment on what the coastal uplift events should impact. Therefore, the age distributions of the reworked samples are also likely to contain some information about the terrace emergence history. Here, I propose a statistical evaluation method of emergence ages by fully using the obtained dataset based on the model assumption of the sedimentation process of the terrace deposits.

3.2.2.1 Sedimentation model of terrace deposits

First, I propose the sedimentation model how the remain of marine organisms, such as shell fossils, is supposed to distribute in ages in the terrace deposits. Because the age distribution in the sediments reflects how the sediments suffer the reworking effect, I present the possible processes of reworking effects and formulate the expected age distribution. In this model, I introduce two processes of reworking; one is the deposition and flow-out process at shoreface, and the other is the inflow from the older generation of terrace deposits.

I formulate the first reworking process at shoreface. In the terrace deposit layers formed on shallow sea bottoms, it is supposed that new remains of marine organisms are buried at a constant rate over time. On the other hand, the amount of older sediments in the layer gradually decreases due to the fragmentation and the flow-out. Assuming that the terrace deposit is sufficiently mixed within the layer and the fraction of the loss of the deposited remains is independent of their ages, the decrease in the number of the remains after the deposition, $m(t)$, is described by the reservoir model (Małoszewski et al., 1983) with the ordinary differential equation

$$\frac{dm(t)}{dt} = -\frac{1}{\kappa}m(t). \tag{3-1}$$

Where κ is the mean residence time of sediments, as shown in Figure 3-2a. Note that the older side is positive of the time axis (yBP). The temporal change of $m(t)$ determines the frequency of the ages of the deposited remains found in the currently forming terrace deposit layer. Hence, the normalized frequency distribution of the such deposited remains' age, $f(t)$, becomes

$$f(t;\kappa) = m(t;\kappa)/\int_0^\infty m(\tau;\kappa)d\tau = (1/\kappa)\exp(-t/\kappa) \quad (t > 0). \tag{3-2}$$

When this terrace deposit emerges from the sea surface at $t = t_e$ and the subsequent sedimentation and erosion (or the inflow and outflow of the remains) are negligibly small, the frequency distribution of the formerly emerged terrace deposit is

$$f(t;\kappa,t_e) = \begin{cases} (1/\kappa)\exp((t_e - t)/\kappa) & (t > t_e) \\ 0 & (t \le t_e) \end{cases}. \tag{3-3}$$
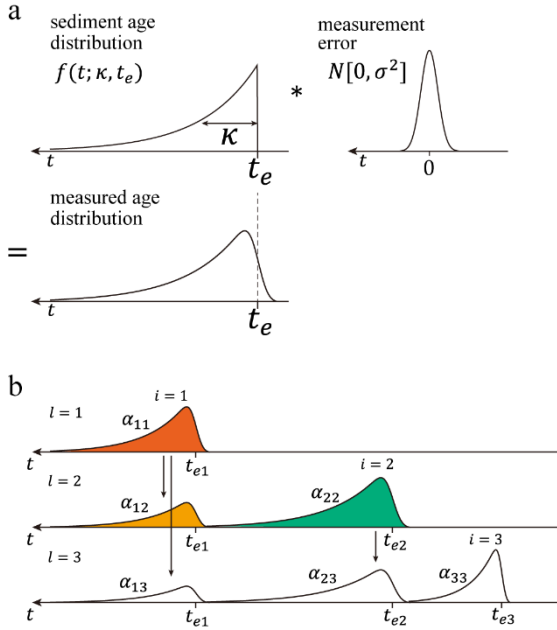
Figure 3-2. Schematic explanation of the dating frequency distributions of the terrace deposit. (a) Expected dating frequency distribution of a single terrace deposit and the convolution of the measurement error. (b) Model of the reworking effect to dating frequency distributions of younger terraces. Refer the main text for the notations and descriptions.

After the emergence of the upper terrace, a new generation of the terrace deposit starts to form.

Secondly, I consider the reworking effect that transfers the sediments from the older terrace deposits into the youngest terrace deposits. The possible process of reworking will be discussed later. Denoting the frequency distribution for the terrace deposit of the ith generation to be $f_i(t; \kappa_i, t_{ei})$, the frequency distribution for the lth level is

$$F_l(t) = \sum_{i=1}^{l} \alpha_{il} f_i(t; \kappa_i, t_{ei}). \tag{3-4}$$

Here, α_{il} is the mixture ratio of the ith generation to the lth level, and $\Sigma_{i=1}^{l} \alpha_{il} = 1$. Figure 3-2b schematically explains this relationship between the frequency distributions of each generation. For example, α_{11} is always 1 because the first level has only this generation. In the second level, the ratio of α_{12} and α_{22} is equivalent to the area ratio of the orange and green areas, and the summation $(\alpha_{12} + \alpha_{22})$ is 1. Previously, these processes that the older materials contaminate into newer sediment (equations (3-2) and (3-4)) have not been differentiated and collectively called "reworking effect." Hereafter, I term the former process "residing" in the terrace deposit to distinguish them.

47

Additionally, the obtained dating results of each sample, $d_k(t)$, include measurement error and the estimation error in the calibration. Hence, I assume a normal distribution $\sim N[0, \sigma^2]$ as the normal error and convolve it with the modeled frequency distribution $F(t)$ (Figure 3-2b).

3.2.2.2 Model parameter estimation

Now, we can assume the model parameters defining the series of modeled dating frequency distributions $F_l(t)$ as

$$\mathbf{A} = \begin{pmatrix} \alpha_{11} & & & 0 \\ & \ddots & & \\ \vdots & \alpha_{il} & \ddots & \\ \alpha_{1L} & \cdots & & \alpha_{LL} \end{pmatrix} \left(\sum_{i=1}^{l} \alpha_{il} = 1 \right),$$

$$\boldsymbol{t_e} = (t_{e1}, t_{e2}, \ldots, t_{eL}),$$

and I set the mean residence time κ to be uniform to each other because the coastal environment has not been significantly changed throughout the targeted time range, judging from the sedimentation structure and the fauna of buried fossils. Here, L means the total number of levels. In this study, the number of terraces is four, and thus the total number of the model parameters, Np, is 11 (6 for $\mathbf{A}$, 4 for $\boldsymbol{t_e}$, and κ). For simplification, hereafter I put the model parameter vector $\boldsymbol{g} = [\mathbf{A}, \boldsymbol{t_e}, \kappa]$.

Next, under the assumption that the dating result of the sediment, t, obtained from the terrace deposits follows the frequency distribution $F_l(t; \boldsymbol{g})$, I estimate the posterior distribution of the model parameters $p(\boldsymbol{g}|D)$ when the observation results D are obtained based on the Bayesian theorem. From the Bayesian formula described as

$$p(\boldsymbol{g}|D) = p(D|\boldsymbol{g}) \frac{p(\boldsymbol{g})}{p(D)}. \tag{3-5}$$

where $p(D|\boldsymbol{g})$, $p(\boldsymbol{g})$, and $p(D)$ denotes the likelihood of observation D when model parameters $\boldsymbol{g}$ are given, and the prior distributions of the model parameters and the observation, respectively. Here, I assume that $p(D)$ is a constant value, and $p(\boldsymbol{g})$ is a uniform distribution. Then, we can estimate the posterior distribution of $p(\boldsymbol{g}|D)$ via the stochastic process with a transition probability $P(\boldsymbol{g}'|\boldsymbol{g}) = p(\boldsymbol{g}'|D)/p(\boldsymbol{g}|D)(= p(D|\boldsymbol{g}')/p(D|\boldsymbol{g}))$ by formulating the likelihood $p(D|\boldsymbol{g})$ with respect to given model parameters $\boldsymbol{g}$.

First, as a simple example, I temporally assume a discrete dataset $D =$

$\{x_1, x_2, \cdots, x_n\}$ comprises n dating results, where x_i denotes the age of a sample. The likelihood $p(D|\boldsymbol{g})$ is obtained by the multiplication of the likelihoods of each dating result $p(x_i|\boldsymbol{g})$ as

$$
\begin{aligned}
p(D|\boldsymbol{g}) &= p(x_1|\boldsymbol{g})p(x_2|\boldsymbol{g})\cdots p(x_n|\boldsymbol{g}) \\
&= \prod_i F(x_i; \boldsymbol{g}).
\end{aligned}
\tag{3-6}
$$

It can be rewritten into summation from by logarithmic expression:

$$
\ln p(D|g) = \Sigma_i \ln F(x_i; g)
\tag{3-7}
$$

Then, I treat the dataset expressed by the probability densities as obtained in this study. Here, I denote the dating result of a sample to be

$$
s_i = \begin{pmatrix} x_1 & d_i(x_1) \\ x_2 & d_i(x_2) \\ \vdots & \vdots \\ x_m & d_i(x_m) \end{pmatrix},
$$

where $\Sigma_{k=1}^m d(x_k)dx = 1$ and $x_k = x_1 + dx(k-1)$. When we obtain the dataset $D = \{s_1, s_2, \cdots, s_n\}$, the likelihood $p(D|\boldsymbol{g})$ is

$$
\ln(p(D|\boldsymbol{g})) = \sum_{i=1}^n \sum_{k=1}^m d_i(x_k) \ln F(x_k; \boldsymbol{g}).
\tag{3-8}
$$

3.2.2.3. Posterior distribution with Monte Carlo sampling

To obtain the posterior distribution of the model parameters $p(\boldsymbol{g}|D)$, I adopt the MCMC methods (MacKay, 2003; Gamerman, 2006). A Markov chain is a stochastic process of $\{x^{(0)}, x^{(1)}, \cdots\}$ that satisfies the updated state $x^{(t)}$ depends only on $x^{(t-1)}$:

$$
P\left(x^{(t)}\middle|x^{(0)}, x^{(1)}, \cdots, x^{(t-1)}\right) = P\left(x^{(t)}\middle|x^{(t-1)}\right),
$$

where $P\left(x^{(t)}\middle|x^{(t-1)}\right)$ is called the transition probability. After a large number of step t, the frequency distribution of the chained dataset of x converges to the probability density $p(x)$. The sample values of the model parameters are iteratively collected following the metropolis method, and the frequency distributions are adopted as the posterior probability distributions. The sample collection is conducted by the following steps:

1. Select an initial set of model parameters $\boldsymbol{g}^{(0)}$ for the initial step $s = 0$.

2. Advance the step number from s to $s + 1$.

3. Generate a set of candidate model parameters $\boldsymbol{g}'$. For each parameter g_j, where j denotes the parameter index number ($1 \leq j \leq Np$), select the candidate value g_j' from a uniform distribution $[g_j^{(s)} - \delta g_j, g_j^{(s)} + \delta g_j]$, where δg_j is the given step size of the Markov Chain. If the candidate value is beyond the supposition, reject it and then keep $g_j' = g_j^{(s)}$. I suppose here that α and κ should be non-negative values, and, for emergence ages, I constrain that $t_{el} > t_{el+1} > 0$ ($l = 1, 2, 3$).

4. Compute the posterior probability of the candidate parameters $p(\boldsymbol{g}'|D)$ (equation (3-6)).

5. Select the set of model parameters for the step $s + 1$ by judging the acceptance of the candidate model parameters as follows by referring to the posterior probability of the previous model parameters $p(\boldsymbol{g}^{(s)}|D)$:

$$\begin{cases} \boldsymbol{g}^{(s+1)} = \boldsymbol{g}' & (if \ p(g'|D) \geq p(g^{(s)}|D)) \\ \boldsymbol{g}^{(s+1)} = \boldsymbol{g}' & (if \ p(g'|D) < p(g^{(s)}|D) \ with \ probability \ r) \\ \boldsymbol{g}^{(s+1)} = \boldsymbol{g}^{(s)} & (if \ p(g'|D) < p(g^{(s)}|D) \ with \ probability \ 1-r) \end{cases} \quad (3\text{-}9)$$

Here, r is the acceptance probability $r = p(\boldsymbol{g}'|D)/p(\boldsymbol{g}^{(s)}|D)$.

6. Iterate steps 2 to 5 for the previously determined number of iterations. After discarding the burn-in samples, the frequency distribution of $\boldsymbol{g}_j^{(s)}$ can be evaluated to be the posterior probability distribution for the jth model parameter.

In this study, I performed 10^6 times iterations and discarded the beginning 10% samples as the burn-in samples. I evaluated the modes of the estimated posterior distributions and the 68% and 95% confidence intervals from the obtained frequency distribution.

3.2.2.4 Additional constraint

In this analysis, for the stability of the estimation, I add another constrain to the model using prior information. In the previous setting, the mixture ratio α_{il} is

independent of the other model parameters, but I assume the correlation with the emergence ages t_e by referring to the observation distribution $D_l(t)$. Specifically, I adopt the values of the mixture ratio α_{il} which depend on the proposed emergence ages $\boldsymbol{t_e}$ that

$$\alpha_{il} = \int_{t=t_{e(i-1)}}^{t=t_{ei}} D_l(t)\,dt \Big/ \int_0^\infty D_l(t)dt. \tag{3-10}$$

This assumption constrains the modeled frequency distribution $F_l(t;\boldsymbol{g})$ to be

$$\int_{t=t_{e(i-1)}}^{t=t_{ei}} D_l(t)\,dt = \int_{t=t_{e(i-1)}}^{t=t_{ei}} F_l(t;\boldsymbol{g})\,dt. \tag{3-11}$$

With this assumption, the total number of the model parameters Np becomes 5 (4 for $\boldsymbol{t_e}$ and κ, when $L = 4$).
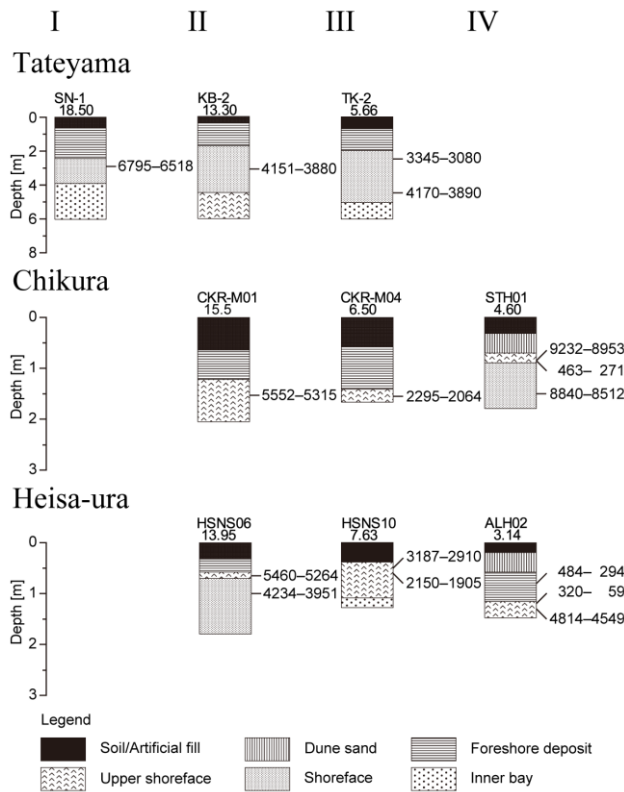
Figure 3-3. Examples of the columnar sections of the sediment samples in this study. The sedimentary layer classification is based on Komori et al. (2017). The number above each columnar section is the surface elevation of the sampling point (meter a.s.l.). The columnar sections obtained from the same level are arranged in the same column, as indicated by the top Roman numbers. The numbers displayed next to each columnar section indicate the dating results (yBP).

3.3 Results

3.3.1 Sampling and dating

3.3.1.1 Sampling results in this survey

For the analysis of the dating estimation, the sampling points in Heisa-ura are classified as colored in Figure 3-1d and Table 3-1. Although the landform boundary between Numa I and II is unclear even from the result of this study, the Geoslicer points HSNS01–07 are classified into Numa II because the following statistical analysis is less sensitive to the contamination from the older terrace to the younger terrace than its reversal as discussed below.

In Figure 3-3, several sedimentary structures beneath the sampling points in this study are displayed. All columnar sections, including the previously surveyed sampling points, are shown in Figure S-1. The types of sediment layers in the survey regions are approximately common: Soil layers just beneath the surface, middle-fine sorted sand layers with prominent lamina structure, coarse sand layers frequently containing abundant shell fragments, and silty-sand layers at deeper part. Following Komori et al. (2017), I identify the middle-fine sorted sand layer and the coarse sand layer as the foreshore deposit and the upper-shoreface deposit, respectively. The shell fossils buried in these layers can be recognized to have lived before the emergence of each terrace. From these sediments, I collected 51 marine samples and five terrestrial samples
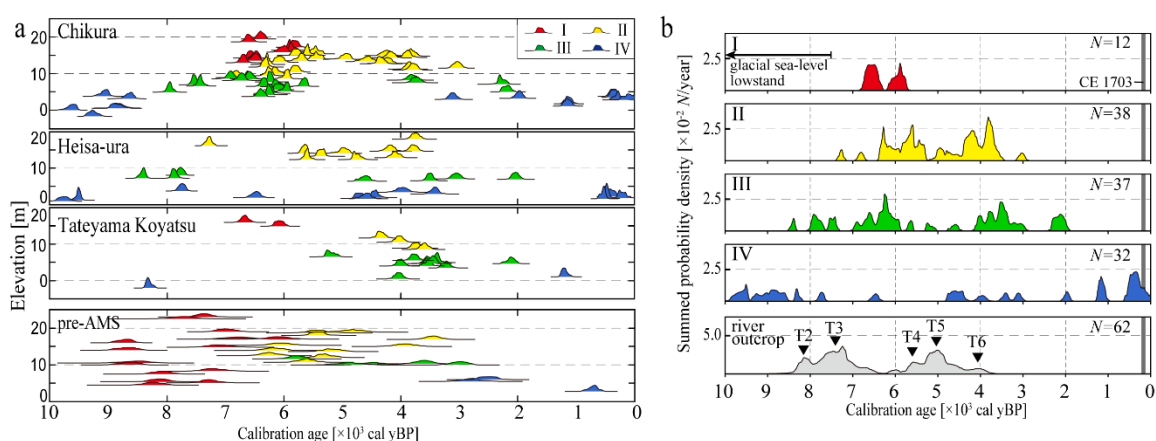
Figure 3-4. (a) Dating results of all samples in the different regions. The dating result of each sample is expressed by the PDF curve, and colors differentiate the terraces where the sampling points are located on their platforms. The bottom panel (pre-AMS) shows the re-calibrated result of the dataset by Nakata et al. (1980). Full dataset is provided in Table S-2–4. (b) Summed PDFs in each terrace level. The bottom panel is the summed PDF of the samples obtained from the river outcrop (Fujiwara et al., 1997; 1999). Triangles indicate the estimated ages of tsunami deposit layers (T2–T6) by Fujiwara et al., (1999).

for the dating measurement.

3.3.1.2 Dating results

The results of the dating measurement are listed in Table 3-2. "Conventional age" shows the measured age after the $\delta13C$ correction with 2σ interval, and "calibrated age" shows the 2σ confidence interval of the estimated age after the calibration. All results, including the previous investigations, are listed in Tables S2–S4. In these tables, all results including terrestrial materials and tsunami deposits. I selected the marine sediment samples from these datasets based on the criteria mentioned above.

Figure 3-4a shows the distribution of all dating results in each coast expressed by probability density functions (PDFs). The PDFs are colored depending on the terrace level to where the sampling points belong. The eliminated samples from the dataset for the inversion analysis, such as terrestrial samples and the marine organisms suspected to be included in the tsunami deposit, are not shown in this diagram. The ages of the youngest samples in Numa I, II, and III are ~5,800 yBP, ~3,000 yBP, and ~2.000 yBP, respectively.

The bottom panel of Figure 3-4a is the recalibrated dating distribution of the dataset by Nakata et al. (1980). Although the measurement error is larger than the current dating, the distribution of the dating result is not inconsistent with the result of this study; the ages of each terrace level is older than the youngest dated samples in the dataset of this study.

The top four panels in Figure 3-4b show the summed PDFs of each Numa terrace totaling the dating results (Figure 3-4a). From these summed PDFs, we can see the clusters typical on multiple levels. The cluster at around 6,000 cal yBP is prominent in levels I, II, and III, and the one from 4,000 to 3,000 cal yBP also can be seen in levels II, III, and IV. These clusters correspond to the residing term of the terrace deposit $f_1(t)$ and $f_2(t)$ expected in equation (3-4).

In Numa III and IV, we can see another cluster older than 7,500 cal yBP. This cluster likely corresponds to another event before the emergence of Numa I. However, no terrace level is identified higher than Numa I, and this age is consistent with the timing of the Holocene high stand in this area (Okuno et al., 2014). Hence, because the sedimentation circumstance of this age might be different from the assumed model in this study, I eliminate the dataset older than 7,500 cal yBP from the following analysis.
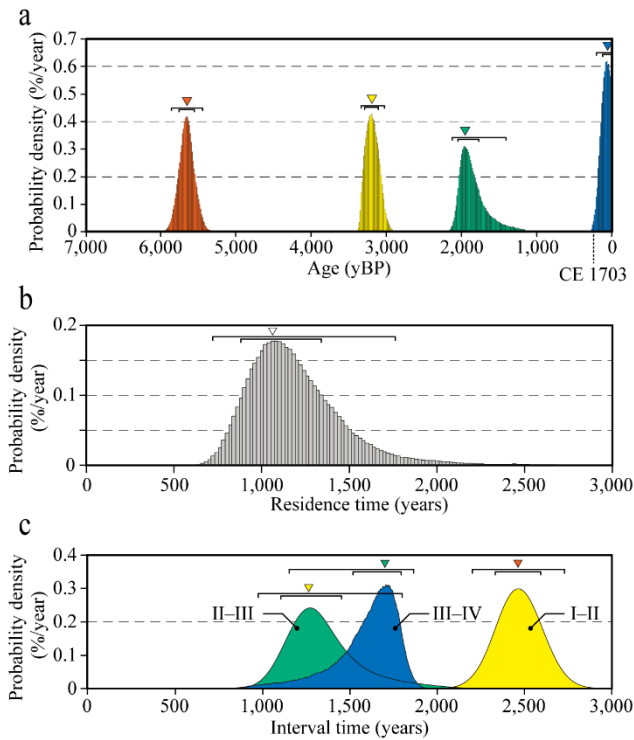
Figure 3-5. The results of the MCMC inversion. (a) Posterior distributions of the emergence ages t_e. (b) Posterior distribution of the mean residence time κ. (c) Estimated distributions of the intervals between the emergence times of the four terraces.

3.3.2 Bayesian inversion

Figure 3-5 shows the obtained posterior distributions of the five model parameters, emergence ages t_e and mean residual time κ, produced by the MCMC iteration displayed as the frequency histograms. The older limits of the posterior distributions of the emergence ages t_e are constrained by the youngest dated samples in each level (Figure 3-4a), which is consistent with the assumption of the conventional interpretations (Komori et al., 2017).

The estimated emergence ages of Numa I, II, III, and IV are 5855–5455 yBP, 3345–3025 yBP, 2125–1415 yBP, and later than 220 yBP, with the 2σ intervals, and the modes are 5655 yBP, 3200 yBP, 1950 yBP, and 65 yBP, respectively (Figure 3-5a). The Numa IV age is recorded in historical documents to be CE1703 (247 yBP), which is close to but slightly beyond the range of this estimation. The estimated mean residence time of terrace deposit τ is 780–1860 years, and the mode is 1070 years (Figure 3-5b).

3.4 Discussions

3.4.1 The validity of the sedimentation model and age estimation

In this study, I assumed one sedimentation model for the inversion analysis, considering the residing in the terrace deposit (equation (3-2)) and the mixture by the

reworking effect (equation (3-4)). Next, I discuss the validity of the proposed model for the robustness of the estimation results. The sedimentation model used in this study is constructed based on three assumptions: Production and flow-out mechanisms of the terrace deposit, the process of the reworking effect, and non-biased sampling.

The first assumption is about the construction of the terrace deposit (equation (3-3)). For the model construction, I assumed that the terrace deposit during its formation experiences (i) continuous production of updated ($t = 0$) organisms and (ii) uniform flow-out independent of the sedimentation age (equation (3-2)). (i) The production of the organisms (mainly shellfish in this study) should depend on the circumstances of the seabed. If there happened a mass generation of organisms, for example, it can be recorded as an unexpected peak in the observed sediment age distributions. Although we have no information about the actual production rate of the organisms in the past Boso Peninsula, the difference of a factor can be ignored because the exponential decay due to erosion and fragmentation should be more substantial and dominant. (ii) For the mechanisms of the flow-out, the uniform flow-out independent of age implicitly assumes a complete mixture within the terrace deposit. The deposit of the Numa terraces consists of coarse sand and shell fragments and indicates the upper-shoreface circumstance, where extreme wave power affects. Several core samples produced reversal age sequences and varied ages at the same depth, which implies a frequent mixture of sediment (Komori et al., 2017; Figure 3-4a). However, these estimations remain theoretical and need verification by a large number of dating in one specific terrace deposit in the future study.

Next, I discuss the types of the reworking process and their possible effect on the sediment age distributions. Figure 3-6 illustrates the schematic structure of the sedimentary terraces. Here, we can consider three types of processes of the reworking effect. First, the extracted older terrace deposit due to river erosion flows into the modern beach (arrows 1 in Figure 3-6). Second, the terrace deposit, which was uplifted but still set beneath the sea-level, flows into the modern beach due to the wave erosion (arrows 2 in Figure 3-6). These effects can be attributed to the mixture process considered in equation (3-4) if the erosion rate is independent of the sediment age (i.e., the complete mixture within the terrace deposit). Here, we consider another contamination of the older terrace deposit, which is the sampling of deeper sediment, as indicated by arrow 3 in Figure 3-6. The observation shows that several sampling core segments have multiple sequences of upper- and lower-shoreface, indicating several generations of terrace deposits in one core segment (Komori et al., 2017). The samples that dated older than 7,000 years obtained from Numa III and IV (Figure 3-4) were perhaps originally from the
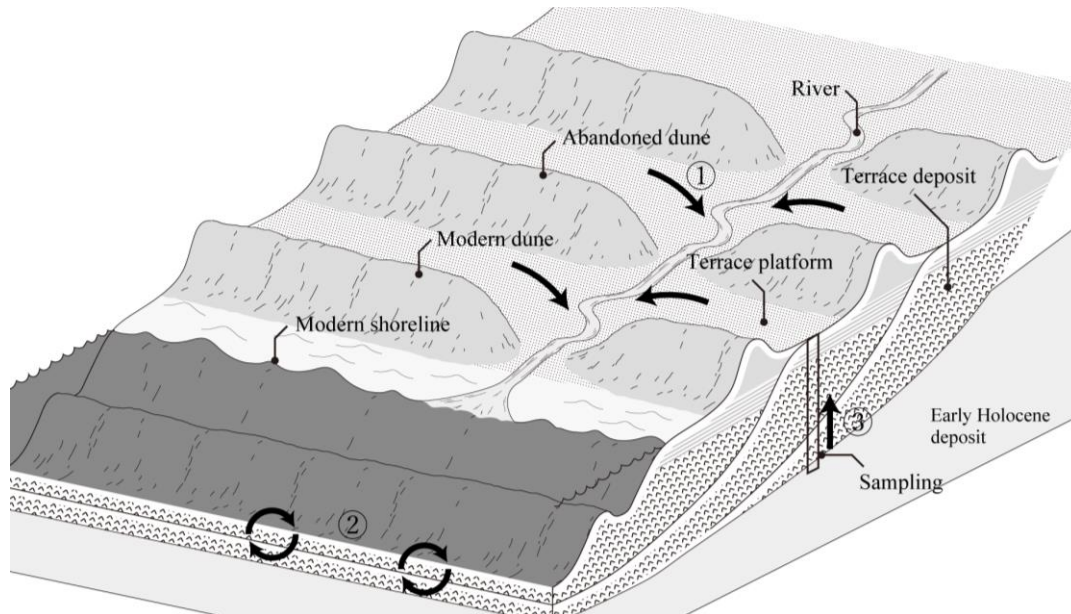
Figure 3-6. Schematic illustration of the reworking processes. Refer the main text for descriptions.

deeper sediments deposited during the early Holocene transgression (Figure 3-6). However, if the sampling was non-biased, this mixture also can be attributed to the mixture ratio α in equation (3-4).

Additionally, it is necessary to consider the impartiality in the sampling when we try to observe the sediment distribution in nature. It should be noted that the picking up of the shell fossils from the sediment had several selection criteria in the dating studies, including our investigation. First, for the stable measurement of the radiocarbon dating, we need the sample size at least ~100 mg. Second, to identify the species of the original shellfish of the fossils, because the original habitat is essential information to judge the reliability of the sampling, usually we select the fossil samples that keep the complete body. Finally, in the conventional dating survey, they avoid worn and weathered materials because they are likely to suffer reworking effect (Komori et al., 2017). This selection of the sampling might bias the observed sediment ages from the original sediment. However, if the selection criterion is uniform among the surveys, the bias in the observed sediment ages can be attributed to the mean residual time κ in equation (3-3). For example, I dated a highly worn shell fragment obtained from Numa IV in this study (STH03155B), and it showed the youngest date in the terrace deposit, which is approximately the age of the 1703 event. This result suggests that the appearance of the shell fossils is not much related to the age of itself than conventionally considered, and thus the effect of the selection bias is less than expected. To improve the estimation in this aspect, we also need to clarify the relationship between the appearance of shell fossils and their age by other dating and

sampling surveys.

3.4.2. Estimated posterior distributions

Finally, I discuss the validity of the inversion method of this study, comparing the characteristics of the estimated posterior distributions of the emergence ages and the information we already had. First, we know the emergence age of Numa IV as the occurrence date of the 1703 Genroku earthquake (247 yBP). On the other hand, the estimated range of the formation age of Numa IV in this study is younger than 220 yBP. The youngest dated sample in the terrace deposit dominantly determines the younger limit of the emergence age estimation. It is STH03155B from STH03 core in Chikura for Numa IV, and its calibrated age is younger than 231 yBP, which is already younger than the 1703 Genroku event. The backward reworking of this material is possible but not high because of the sediment structure. Another possible source of this distortion is the marine reservoir effect. We dated the fossils uplifted due to the 1923 event in the previous studies (Shishikura et al., 2007; Komori et al., 2017), but the number of dated samples is relatively small, and the degree of marine reservoir effect can be varied depending on location along the coast. Therefore, it is highly challenging to eliminate the marine reservoir effect in less than several decades. In this study, I should note there possibly exist a systematic error of several decades.

Next, the distributions of the estimated posterior distributions of the upper levels, Numa I, II, and III, also show essential information on the validity of the estimation. The posterior distributions of Numa I and II (Figure 3-5a) show approximately symmetrical distribution with ~100 years of 1σ intervals, while that of Numa III shows unsymmetrical distribution whose younger side has a much longer confidence interval. These distributions perhaps reflect the number of the referred samples; the clusters corresponding to $f_1(t)$ and $f_2(t)$ (equation (3-4)) can be seen throughout three levels and include a sufficient number of dated samples, whereas the third cluster $f_3(t)$ can refer to only two levels and contain six samples. This result should reflect the prior information that if we have a smaller number of dated samples, we cannot sufficiently determine the younger side of the emergence age, and I first quantify this conventional supposition.

In this study, I summarized the comprehensive dataset of the dating results previously conducted in the Numa terraces. However, in the statistical analysis, I used only 119 results, which is less than 40 % of the full dataset. Here, I compare the result of this study with the other types of available datasets. I recalibrated the dating results

conducted without δ13C correction (Nakata et al., 1980) (bottom panel of Figure 3-4a). Although the confidence intervals are much larger than the recent measurements, the systematic distributions are consistent with the result of this study: All of the dated samples in each level are older than the estimated emergence age, and clusters correspond to each generation of terrace deposit appear. In Nakata et al. (1980), the youngest dated samples obtained in the Numa II platform are eliminated from their discussion because they are too young, but the results of this study suggest they are still reliable.

Besides, I eliminated the suspicious dataset that has suffered backward reworking judging from the sampling circumstances, where they are obtained in the marshy lowland (TB-3–6) and river outcrops. Figure 3-4b shows the observed ages summarizing the dating results from the river outcrops (Fujiwara et al., 1997): 48 samples from the Heguri river in Tateyama and 14 samples from the Tomoe river in Heisa-ura (Figure 3-1d and e). This distribution clearly shows two clusters from 8000 yBP to 4000 yBP. Fujiwara et al. (1999) discussed it along with the sedimentation structure and estimated it includes five layers of tsunami deposits (T2–T6) due to the lesser Taisho-type events, as indicated in the bottom panel of Figure 3-4b (T4 event might correspond to the Genroku-type event that uplifted the Numa II terrace). Comparing this distribution with the sediment ages from terrace deposits (Figure 3-4b), the peaks show the complementary phases. If we assume that the Taisho-type events occur (quasi-)periodic, there are two possible reasons why the age distribution of the tsunami deposit has complementary peaks to that of the terrace deposit. The first possible cause is that the tsunami deposit less likely to settle before the larger Genroku-type due to some coastal circumstances, such as elevations change. Otherwise, the more extensive tsunami inundation due to the Genroku-type event possibly removes the recent tsunami deposits at shallow depth. At this moment, the mechanism behind this difference is unclear, but this result suggests we should carefully distinguish the tsunami deposit and terrace deposit because they have fundamentally different sedimentation and preservation processes and tend to show different age distributions.

3.4.3. The updated formation history of the Numa terraces

Now, along with the result of the geomorphological survey, the combined dataset of the emergence ages and the present elevations of the paleo-shoreline angles is available. Figure 3-7 shows the estimated uplift history in the west of Heisa-ura (star in Figure 3-1b), where the estimated uplift rate is the highest in the study region. As discussed in the previous studies (Komori et al., 2017), it is suggested that the Numa terraces have varied formation interval times while having approximately similar relative heights. As a result
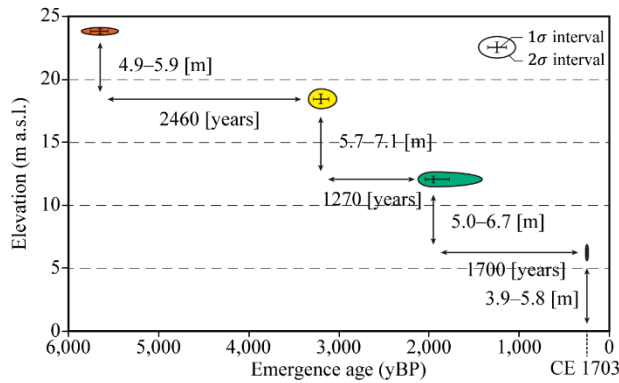
Figure 3-7. Estimated uplift history at the west of Heisa-ura. The elevations of the paleo-shoreline angles are taken from west of Heisa-ura (Figure 3-1a) estimated in this study (Figure 2-6).

of this study, the minimum interval time is 1270 years (between Numa II and III), and the maximum is 2460 years (between Numa I and II). Although the minimum value has relatively high uncertainty because the emergence age of Numa III has a wider confidence interval, the interval time between Numa I–II is nearly twice as long as the shortest one. The variation of the interval times of the Numa terrace formation is quantitatively evaluated for the first time in this study.

Previously, the Numa I terrace has been regarded as the Holocene highest marine terrace, which was formed during the Holocene high stand approximately 7,500 years ago (Nakata et al., 1980; Okuno et al., 2014). This assumption has been supported by the dating result of a shell fossil (oyster shell) attached to the bedrock in Chikura (TH-277 from Nakata et al. (1980), Table S-4). However, the elevation of this sampling point (~23 m a.s.l.) is higher than the estimated elevation of Numa I in Chikura in this study, and the age of this shell fossil (7675–7035 cal yBP) is older than the newly evaluated Numa I age. These inconsistencies suggest that the Holocene highest marine terrace in this area is different from Numa I. Also, along the rocky coast, a higher terrace than Numa I was shown in some sections in the geomorphological analysis (Figure 2-4a). The topographic connection is not confirmed along the wider region, but this level might correspond to the Holocene highest terrace.

4. Mechanical reexamination of the crustal deformation history along the Sagami Trough

4.1 Introduction: Open questions about subduction models

To interpret the relationship between the earthquake recurrence along the Sagami Trough and the accompanying crustal deformation, I construct the 3-D elastic dislocation model based on mechanical constraints on the plate interface. Many of the previous earthquake cycle modeling using elastic dislocation model adopted the kinematic back-slip model (BSM) (Savage, 1983; Sato et al., 2016). However, the BSM does not preserve any deformation after an earthquake cycle if a kinematic constraint is assumed that the total accumulation and release of the slip are equivalent (Kanda and Simons, 2010). Then, I utilize the elastic subducting plate model (ESPM) by Kanda and Simons (2010) that reproduces more realistic features of subduction zones and adapt them for earthquake cycle modeling by considering the mechanical coupling (Johnson and Segall, 2004; Herman et al., 2018; 2020).

I examine two issues that have been questioned by the previous studies with kinematic subduction models. The first problem is about the preservation of permanent uplift after an earthquake cycle completion. I focus on the local geometry on the plate interface that possibly has a large contribution in ESPM and introduces the geometry of the subducted seamount, which the previous seismic survey suggested (Tsumura et al., 2009). The second issue is about the relationship between the event interval times and the preserved crustal uplift. I test the dependence of them on the rupture extent of each event.
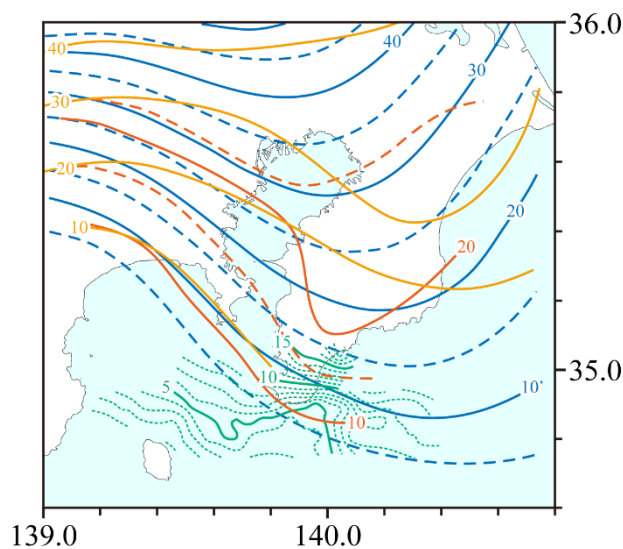
Figure 4-1. Depth distribution of the upper interface of PHS estimated by (orange) the seismic tomography (Hirose et al., 2008), (blue) seismicity (Hashimoto et al., 2004), and (red, green) active source seismic surveys on land (Sato et al., 2016) and offshore (Tsumura et al., 2009). The unit is km.

4.2 Dataset

4.2.1 Plate interface structure of the Sagami Trough

The previous source estimations of the historical earthquakes have pointed out that the structure of the upper interface of the subducting PHS has a significant contribution to the evaluation of the coseismic slips (Sato et al., 2005; Namegaya et al., 2011). Various structural geological surveys have investigated the geometry of the upper surface of PHS such as seismic tomography (Hirose et al., 2008; Ito et al., 2019), active source seismic surveys (Sato et al., 2005; Tsumura et al., 2009; Kimura et al., 2010; Miura et al., 2011), and seismicity (Ishida, 1992; Hashimoto et al., 2004) (Figure 4-1). The detailed geometry of the source region of the Kanto earthquakes, which is quite essential for the local deformation evaluation, is the subject of seismic reflection surveys. Specifically, Tsumura et al. (2009) conducted a comprehensive seismic survey focusing on the shallower part of the upper interface of PHS around the Awa region and inferred a subducted seamount whose height and width are 3–5 km and ~20 km, respectively. This local geometry is acceptable based on the other seismic survey profile (Miura et al., 2011; JAMSTEC, 2012; Miura and Arai, personal communication).

4.2.2 Geological and geodetic datasets

I used the elevations and formation ages of the Holocene marine terraces as the observation data of surface displacement obtained in the previous sections. The observation that is required to be reproduced by the kinematic model is the distributions
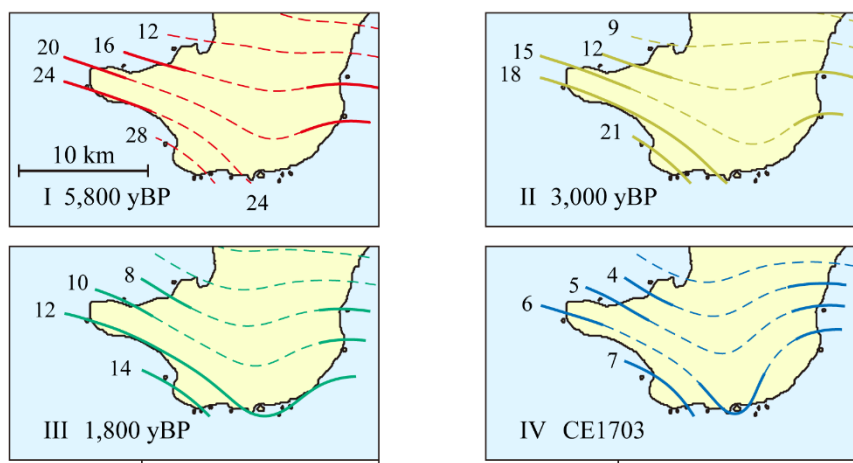
Figure 4-2. Elevation distributions and the formation ages estimated in this study. Dashed lines are interpolated contours.

of the four levels of marine terraces whose relative heights reach 6–7 meters at the southernmost part of the Boso Peninsula and steeply decrease toward the north (Figures 2-6c and 4-2). The formation ages of the terraces are constrained to be approximately 5,800, 3,000, 1,800, and 200 years ago, respectively.

Moreover, other observations are available to constrain the model parameters. The present GNSS observation and estimated slip deficit rate on the plate interface (Sagiya, 2004; Noda et al., 2013) can be used for the validation of the interseismic movement of the model. The historical geodetic measurement and the results of source inversions (Kobayashi and Koketsu, 2005; Nyst et al., 2006) (Figure 1-3a) constrain the configuration of the rupture property. Moreover, the geological and historical studies (Fujiwara et al., 1999; 2000; Shishikura et al., 2001; Ishibashi, 2020) indicated the averaged intervals of the smaller type (Taisho-type) of the Kanto earthquakes.

4.3 Models and Methods

4.3.1 Mechanical plate subduction and the earthquake cycle model

I simulate the crustal deformation around the subduction zone using the mechanical dislocation model. Many dislocation models have been used to represent the subduction zone deformation (e.g., Savage, 1983; Matsu'ura and Iwasaki, 1983). In this study, I utilize the concepts of ESPM proposed by Kanda and Simons (2010; 2012) and mechanical coupling (Johnson and Segall, 2004; Herman et al., 2018; 2020). The ESPM reproduces the subduction of the oceanic plate by the steady dislocation on the upper and lower boundary of the subducting plate (Figure 4-3). It is a quite simple elastic dislocation model with one more degree of freedom than the simplest dislocation model, back-slip model, of Savage (1983) but can produce a more realistic elastic deformation pattern the plate subduction as detailed below. Additionally, the mechanical coupling is a concept to realize a more kinematically realistic co- and inter-seismic slip distribution on the upper plate interface via a stress-based boundary condition. The approximation with the basic kinematic back-slip model assumes that the coseismic slip amount is the reflection of the accumulated interseismic back-slip can be less accurate when the plate interface has short-wavelength structures such as subducted seamount, as discussed below. In this model, I simulate the earthquake cycle based on balancing shear stress change on the plate interface that is expected to produce long-term crustal deformation depending on the plate interface geometry. Note that the cycle terms, in this study, the sequence of earthquakes with the interseismic stress build-up and the coseismic stress release, which is not always characteristic.
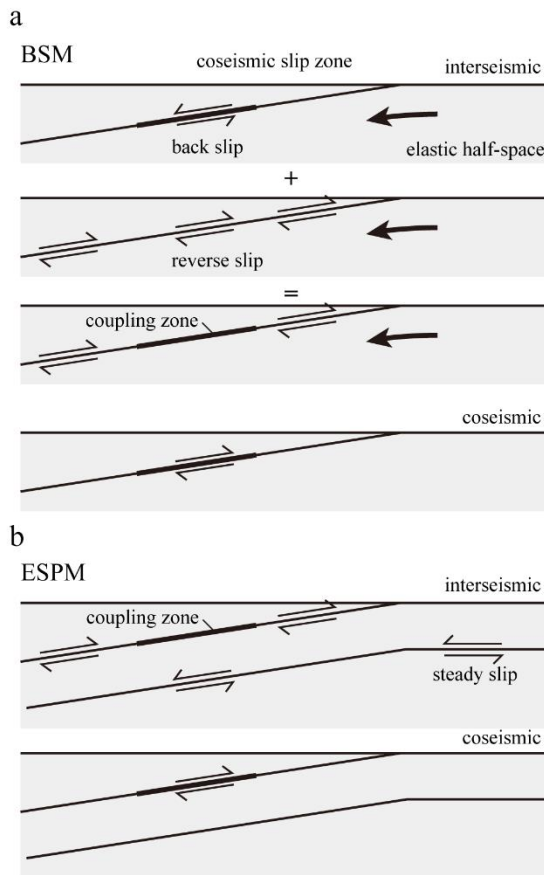
Figure 4-3. Schematic illustrations of (a) the back-slip model and (b) the elastic subduction plate model. Refer the main text for descriptions.

Figure 4-3 schematically illustrates and compares the back-slip model (Savage, 1983) and the ESPM (Kanda and Simons, 2010; 2012). The back-slip model represents the interseismic strain accumulation by superposing the uniform reverse slip on the whole plate interface and the normal slip (named back-slip) upon the locked zone. On the other hand, the ESPM assumes the uniform reverse and normal slips on the subducting plate's upper and lower boundary, respectively, except for the coupling zone. When the geometry of the plate interface is determined, the degree of freedom of ESPM is only one more than that of the back-slip model (thickness of the subducting plate H). Kanda and Simons (2010) show that the ESPM model produces a permanent deformation after a seismic cycle, which comprises subduction along the trench axis and uplift at shortly arcward of the trench due to the curvature on the plate interface. I employ ESPM to discuss the long-term deformation around the subduction zone because the back-slip model does not preserve any crustal deformation after an earthquake cycle.

Matsu'ura and Iwasaki (1983) and Sato et al. (2016) take into account the effect of the permanent displacement, which was ignored by the back slip model. As discussed in Fukahata and Matsu'ura (2016), the permanent displacement explained by this model is

caused by the combination of the lifting up of the plate due to the curvature on the plate interface and the gravitational compensation tends to draw back the uplift. However, this model pays attention to the broader scale of deformation that is comparable to the lithosphere thickness, such as the island arc formation. Therefore, the effect of a minor structure on the plate interface, such as a subducted seamount, is beyond the reach of this assumption. To overcome their limitation, I employ the mechanical model considering the stress-based boundary condition for the earthquake cycles as detailed below.

The postseismic transient displacements due to asthenospheric viscosity is not included in the present model because I deal with the deformation process of 400–10,000 years, which is much longer than the stress relaxation time of approximately five years for a typical value of asthenosphere viscosity (Matsu'ura and Iwasaki, 1983; Sato et al., 2016) and even the complete post-seismic decay of the transient vertical displacement of over 100 years (Sato and Matsu'ura, 1988). The effect of gravitational compensation (Matsu'ura et al., 1989) is not also included, but this effect is not significant in the wavelength shorter than the lithospheric thickness. In this study, I focus on the displacement pattern in the scale of 10 km, representing the size of the southern Boso Peninsula area. For another source of the permanent displacement accompanying the plate subduction, the contribution of branch faults is reported in many subduction zones
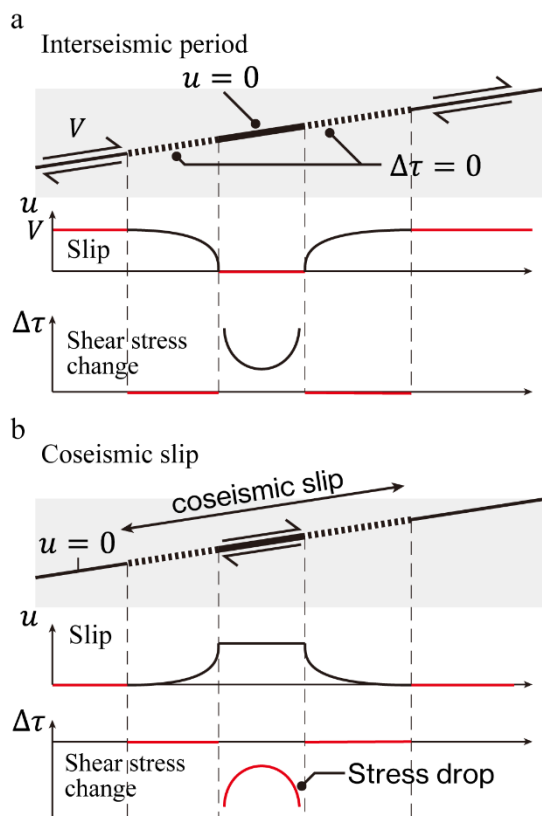
Figure 4-4. Schematic illustration of the boundary conditions of the mechanical coupling. (a) Boundary conditions on the upper plate in the interseismic period. (middle) Slip rate distribution. (bottom) Shear stress change rate distribution. Red lines indicate the boundary conditions and black lines are calculated distributions. (b) Boundary conditions at the coseismic slip. (middle) Coseismic slip amount. (bottom) Coseismic shear stress change. Line colors are same as (a).

(Plafker, 1972; Park et al., 2000; Clark et al., 2017; Shyu and Wang, 2018) and is invoked by directly modeling individual faults (Cummins and Kaneda, 2000) or by mimicked as balk plasticity (Wang and Bilek, 2011). However, in the vicinity of the study region, no clear evidence of significant Holocene activity of inland faults is reported by active fault studies (Suzuki et al., 1990; Kawakami and Shishikura, 2006). The reflection survey by Mori et al. (2015) reported that the averaged slip rate of the offshore splay fault is possibly 0.56 m/ka in the past 18,000 years, which is less significant than modifying the signatures of the subduction process in this area. Therefore, as the first-order approximation, I neglect the asthenospheric viscosity and upper plate inelastic deformation.

In this study, I simultaneously model the earthquake cycle and the crustal deformation modifying the ESPM by considering the mechanical coupling, based on the stress balancing between interseismic accumulation and coseismic release. Figure 4-4 schematically illustrates the configuration for the earthquake cycle model. The upper plate interface is divided into the aseismic area and the coseismic slip area, and the coseismic slip area is also divided into the coupling patch and the decoupled zone. In the interseismic period, steady slips equivalent to the plate subduction rate occur on the whole lower plate interface and the aseismic area on the upper plate interface, while no-slip occurs and the shear stress accumulates on the coupling patch. The decoupled zone, which is a remaining part of the coseismic slip area, behaves as a transition zone between the aseismic area and the coupling patch without accumulating the shear stress at this phase. Then, the coseismic slip amount is given to release the accumulated shear stress (stress drop) on the coupling patch. The restored slip amount depends on the plate interface's geometry, where the geometry with larger curvatures and shorter wavelengths have stronger effects (Fang and Dunham, 2013; Romanet et al., 2020). Thus, the total slip amount throughout the earthquake cycle is not necessarily equal to the amount of plate subduction, unlike the assumption in Sato et al. (2016) and the simple back-slip model (Savage, 1983).

Because I focus on developing a possible model that can explain the ages and heights of observed marine terraces, I first examine the relationship between the configuration of the plate interface, such as the short wavelength geometry and the positions and rupture timings of the coupling patches. Next, I propose a requirement to reproduce the characteristics of the observed marine terraces and the surface deformation pattern with the two-dimensional model, particularly the similar relative height distribution despite the different formation intervals. Then, I expand to a three-dimensional half-space approximating the Sagami Trough subduction zone and search for

a possible rupture scenario that reasonably matches the observation by trial and error.

4.3.2 Formulation of the mechanical earthquake cycle model

I modeled the upper surface of PHS approximating the estimated geometry by Hashimoto et al. (2004) and Sato et al. (2005) and the lower PHS by shifting this geometry by the plate thickness H. I set the plate thickness H to be 40 km in this study, following the lithosphere thickness assumed in the previous study (Sato et al., 2016). Just beneath the Awa region, I further added the subducted seamount's geometry revealed by Tsumura et al. (2009) only on the upper surface. The modeled geometry of the upper surface of PHS is shown in Figure 4-5. I meshed this plate interface into the triangular boundary elements and classified into coupling patches, decoupled zone, and aseismic areas.

Next, I formulate the governing equation and boundary conditions of the modeled earthquake cycle. I constrain all slip motion on the interface to parallel this plate motion direction for simplicity. I employ the static boundary element method with the triangular element embedded in a homogeneous half-space (Meade, 2007). The shear stress change on the slip area, $\Delta\tau$, and the displacement on the free surface Δu due to fault slip s is given by the representation theorem:

$$\Delta\tau_i = \Sigma_j K_{ij}^{\text{trac}} s_j \tag{4-1}$$
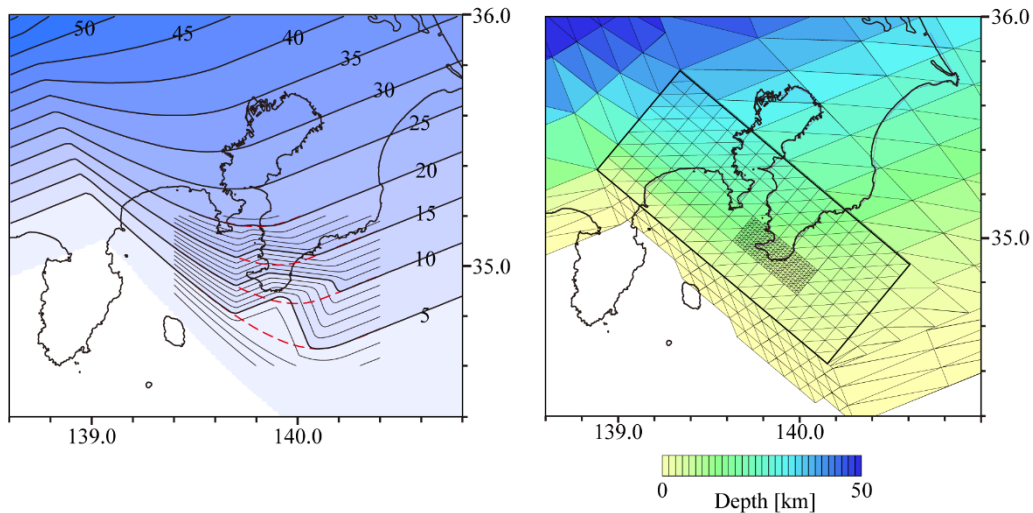
Figure 4-5. Geometrical settings of the three-dimensional subduction model. (a) The depth contour (km) of the upper plate interface of PHS. Solid contour indicates the geometry of the upper plate interface including the subducted seamount, while red broken contour indicates the plate interface without seamount geometry. (b) Configuration of the triangle dislocation patches around the survey region.

$$\Delta u_i = \Sigma_j K_{ij}^{\text{disp}} s_j \qquad (4\text{-}2)$$

where K^{trac} and K^{disp} denote the kernel matrices, and i and j denote the index number of the receiver point and the source element, respectively. Equations (4-1) and (4-2) are used to calculate the slip amount on the coseismic slip area and dislocation amount on the ground surface, respectively.

I next construct the boundary conditions specifically assigned to the aseismic and seismic areas in each of the interseismic and seismic periods. I always assign the displacement boundary condition with the uniform slip rate on the lower boundary of the plate and aseismic area of the upper boundary as $-V$ m/year on the lower boundary and as V m/year on the aseismic area of the upper boundary, where V is the relative plate motion rate of PHS to the land plate (DeMets et al., 1994) and the plus or minus signs stand for the reverse and normal motions (see Figure 4-3). On the seismic area of the upper boundary, I use the mixed boundary conditions:

$$s_{i \in (\text{coupling patch})} = 0 \qquad (4\text{-}3)$$

$$\Delta \tau_{i \in (\text{decoupled zone})} = 0. \qquad (4\text{-}4)$$

The solution for the boundary condition of stress (equation 4-4) is given by

$$s_i = \Sigma_j (K^{\text{trac}})_{ij}^{-1} \Delta \tau_j \qquad (4\text{-}5)$$

where $(K^{\text{trac}})^{-1}$ denotes the inversion matrix of K^{trac}. By solving this equation, I obtain the shear stress change in the seismic area throughout the interseismic period (Figure 4-4a). For the next step of the coseismic slip, I here prepare the stress drop distribution $\Delta \tau'$ which are the summation of the interseismic stress change and the inherited stress from the preceding cycle. Next, in the coseismic period, I use the other mixed boundary conditions:

$$\Delta \tau_{i \in (\text{rupture area})} = -\Delta \tau_i' \qquad (4\text{-}6)$$

$$s_{i \in (\text{intact area})} = 0, \qquad (4\text{-}7)$$

where rupture area means the union of the decoupled zone and the designated coupling patches, and the intact area is the remaining coupling patches. In the intact area, the shear stress further accumulates in the coseismic period as calculated by equation (4-1) and is inherited to the next event. Figure 4-4b shows the coseismic slip without an intact area.

4.3.3 Configuration of the coupling patches and the modeled earthquake cycle

I next examine the requirements for the spatial distribution of the coupling areas and the associated coupling coefficient to reproduce the observed marine terrace distribution. I consider the source area on the Sagami Trough subduction zone, spanning between the Izu Peninsula to the west and the east off Boso Peninsula to the east, as shown in Figure 4-5b. For the current earthquake recurrence simulation, the positions and extents of coupling patches and their rupture timings are prescribed as model input parameters, not determined by fracture criteria. Here, I determine the parameters based on the observations and the results of the two-dimensional model described below.

The coupling patch configuration can follow the observations of coseismic slip distributions and the present geodetic measurements. I assume two coupling patches beneath Odawara and the Miura Peninsula (northwestern patches), referring to the slip concentration indicated by the slip inversion studies of the 1923 Taisho earthquake (Sato et al., 2005; Nyst et al., 2006). These couplings are consistent with the slip deficit estimation using GNSS observation (Sagiya, 2004; Noda et al., 2013). I additionally place other coupling patches around the Awa region, which are estimated to be the main source region of the 1703 Genroku event (Sato et al., 2016), and identified where the slip deficit concentrates (Sagiya, 2004; Noda et al., 2013). However, the detailed slip amount and distribution here in the historical event is unclear. Therefore, I determine the positions of these southwestern patches by referring to the result of the examination with the two-dimensional subduction model.

I simulate the earthquake cycle along the Sagami Trough by specifying the rupture areas allowing the variation in the involved patches and the timings of each event. Following the previous interpretation, I assume that the northwestern patches rupture every 400 years. On the other hand, the source areas of the Genroku-type events are poorly understood even if the ages of the uplift events of the Awa region are well constrained. Therefore, along with the examination of the positions of the coupling patches, I also evaluate the possible rupture extent and timings via the two-dimensional model (plane-strain condition) to explain the observed heights of the marine terraces.

Figure 4-6 demonstrates the 2-D model approximates the structure of the
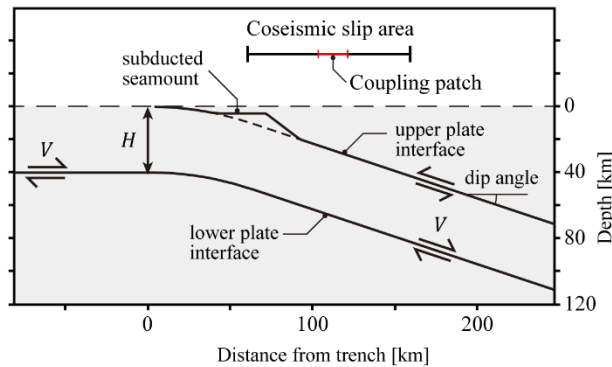
Figure 4-6. Settings of the two-dimensional subduction model. Refer the main text for descriptions.

subducting PHS beneath the Boso Peninsula, including the subducted seamount. This 2-D model comprises 3-D dislocation elements (Meade, 2007) sufficiently long in the direction perpendicular to the plane of the paper. I examine the dependence of the final deformation pattern on the configurations of the subduction and coupling patches using this approximation. First, to explore the dependence on coupling patches, I change the configuration of the coseismic slip area with (i) no coupling patch, (ii) patches on a limited part (partially-coupled), and (iii) patches in the whole coseismic slip area (entirely-coupled). Second, I explore the dependence on the large-scale geometry, including the subducting angle and thickness, of the subducting plate and local geometry due to a subducted seamount. Finally, I explore the deformation pattern representing the uplifted coast by changing the rupture scenario with multiple coupling patches.

Finally, I search for the rupture scenario regarding the areas and timings that can explain the observed elevation distribution of the Numa terraces on a trial and error basis. In this study, I limit ourselves to find a possible scenario as one of the candidates having a physically reasonable basis, rather than exploring all possibilities or singling out the unique solution due to limitation in the presently available data.

4.4 Results

4.4.1 Approximation with a two-dimensional model

Before constructing the formation scenario of the Numa terraces, I examine the characteristics of the deformation pattern produced by the mechanical model in this study and the required conditions to reproduce the observation using the 2-D model. First, to explore the deformation pattern after a cycle of interseismic and coseismic deformation, I examine the relationship between the deformation pattern and the subducting plate geometry. The configuration of the coupling patch is shown in Figure 4-7a. Figure 4-7b shows the shear stress change and slip distribution on the upper plate interface and the
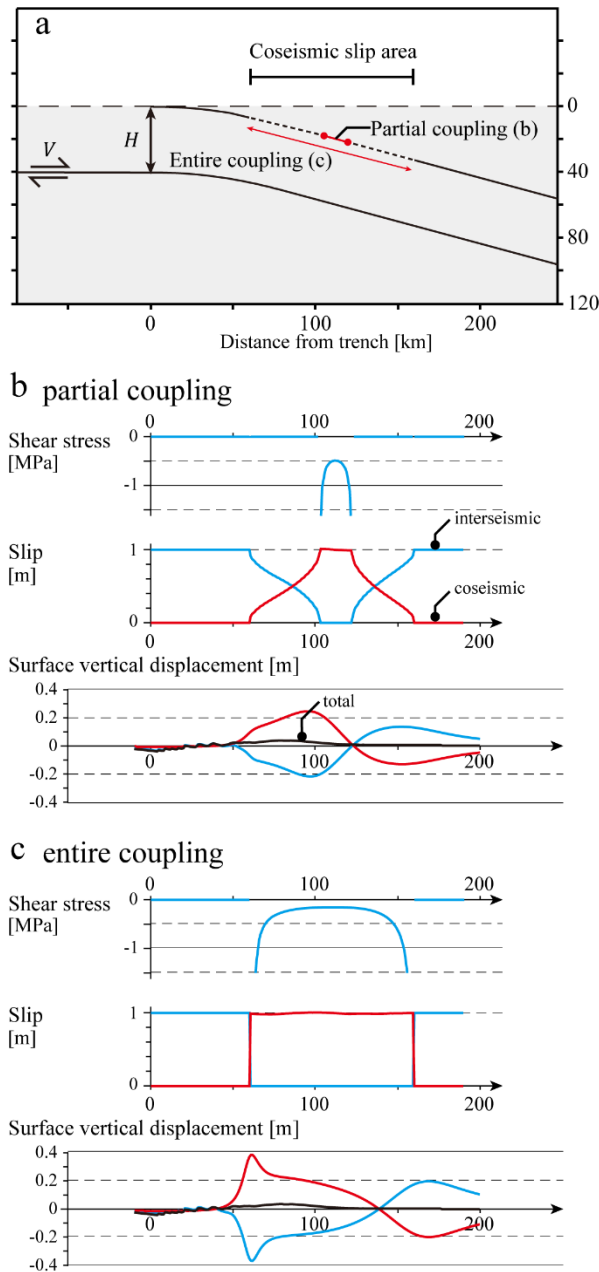
Figure 4-7. Examination result of the two-dimensional model without the subducted seamount geometry and the comparison with different settings of the coupling. (a) Cross-sectional view of the model. (b) The distributions of the shear stress change (top) and slip (middle) on the upper plate interface and the distribution of the surface vertical displacement (bottom). Red, blue, and black lines indicate the distribution of coseismic, interseismic, and total period. (c) The distributions when the coseismic slip area is entirely coupled. The line colors are same as (b).

vertical surface displacement of interseismic, coseismic, and total periods when the rupture zone is partially coupled, and Figure 4-7c shows those when the rupture zone is entirely coupled. Here, I assume the unit slip $V = 1$ (m) for the total slip amount during the interseismic period when giving the boundary condition. I set the same total slip amount in the succeeding examination of 2-D models. The shear stress change distributions show the typical stress concentration on the edges of the coupling patch. The slip distribution of the partially coupled model (Figure 4-7b) shows a concentration of slip and slip deficit on the coupling patch in the coseismic and interseismic periods,
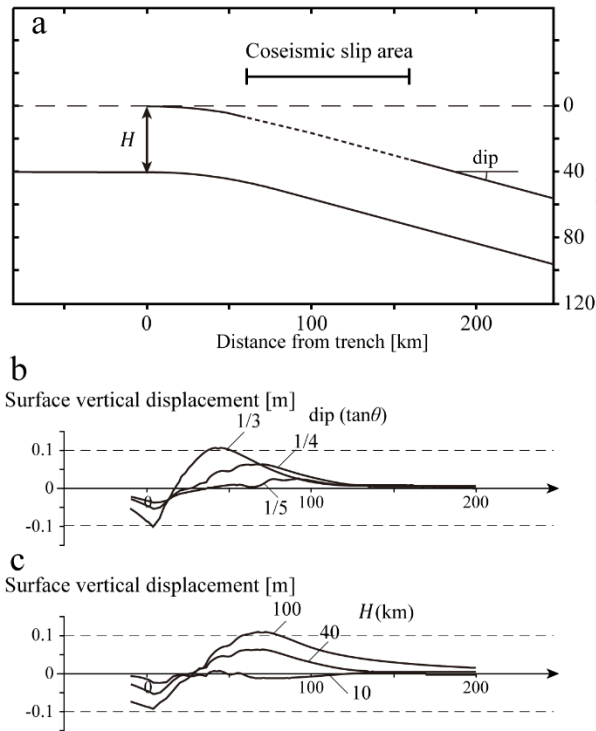
Figure 4-8. Examination result of the two-dimensional model comparing the surface displacement change with different geometrical parameters of the subducting plate. (a) Cross-sectional view of the model. (b) The distributions of the total surface displacement with different dip angles of the subducting plate. (c) The distributions of the total surface displacement with different thickness of the subducting plate.

respectively, and the gradual change of slip amount in the transition zone (decoupled zone). The coseismic and interseismic surface displacements depend on the configuration of the coupling patch; the peaks of displacement appear just above the upper edge of the coupling patch, but the total displacement distribution is a constant independent of the coupling configuration. I next examine the relationship between the total surface displacement and the large-scale geometry of the subducting plate, such as the subducting angle and the thickness. These relationships are already discussed by Kanda and Simons
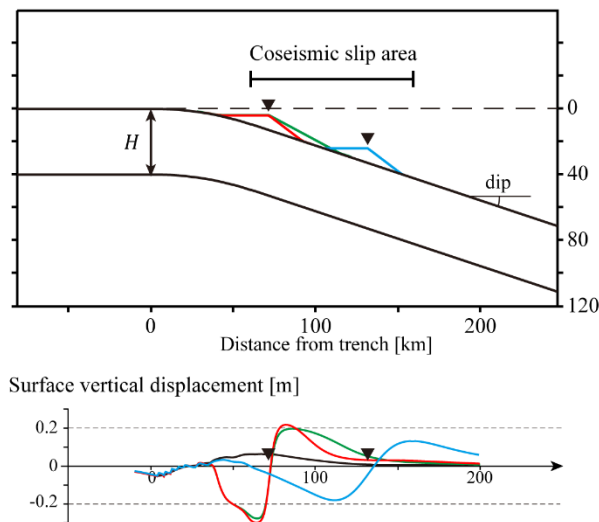
Figure 4-9. Examination result of the two-dimensional model comparing the surface displacement change with different geometries of the subducted seamount. (a) Cross-sectional view of the model. Red, green, and blue lines indicate the modeled geometries of the subducted seamount. The black triangles indicate the positions of the summit of the subducted seamount. (b) The distributions of the total surface displacement with different geometries of the subducted seamount. The line colors and triangles correspond to the seamounts shown in (a).

71
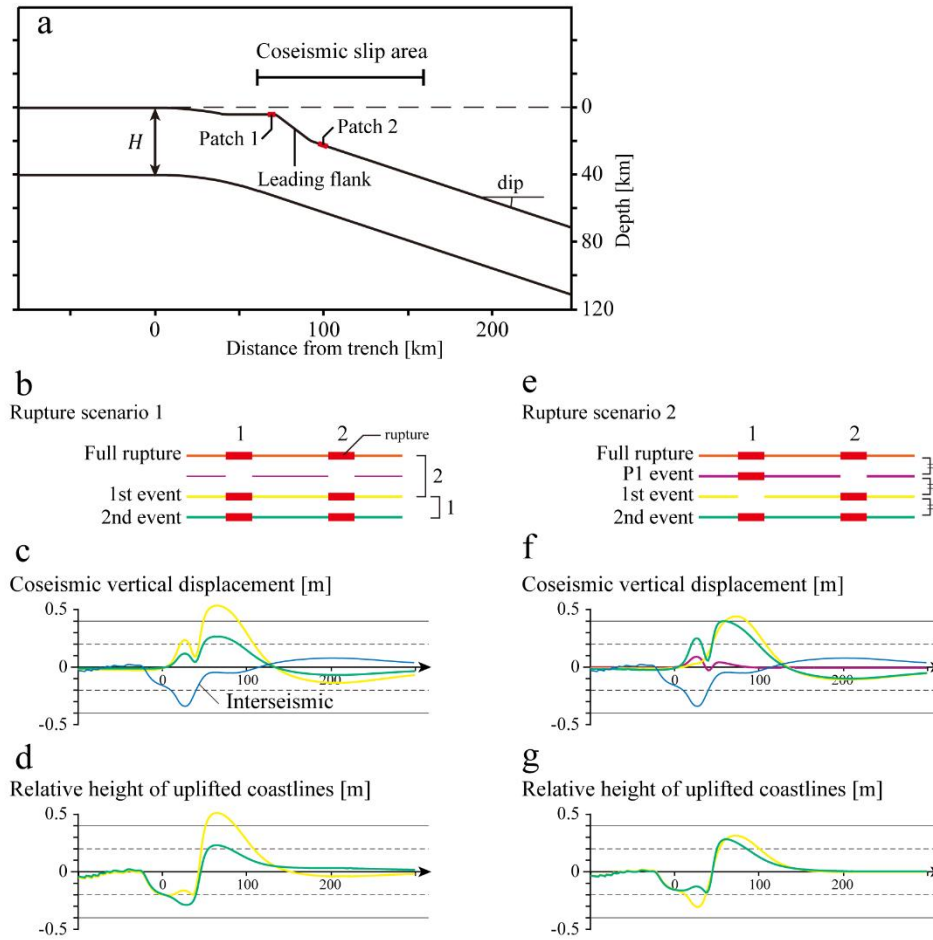
Figure 4-10. Examination result of the two-dimensional model comparing the coseismic surface displacements and the heights of the uplifted coastlines with different rupture scenarios. (a) Cross-sectional view of the model. Red lines indicate the positions of coupling patches. (b) Rupture timings of the coupling patches of the rupture scenario 1. Two events occur after an entire rupture whose interval times are twice different. (c) The distributions of the coseismic displacement. Yellow and green lines indicate the distributions of the first and the second event, respectively. The blue line indicates the displacement in the interseismic period, (d) The distributions of the total vertical displacement since the rupture event until the next event of scenario 1. These distributions correspond to the relative heights of the uplifted coastlines. (e) Rupture timings of the coupling patches of the rupture scenario 2. Three rupture occur after an entire rupture with a constant interval time where the ruptured coupling patches are different; only patch 1 is ruptured (P1 event), only patch 2 is ruptured (the first event), and the entirely ruptured event (the second event). (f) The distributions of the coseismic displacement. The purple line indicates the coseismic displacement of the P1 event. (g) The distributions of the total vertical displacement since the rupture event until the next event of scenario 2.

(2010), so I briefly demonstrate them in Figure 4-8 that (i) the steeper the subducting angle, the more localized the uplift near the trough axis, and (ii) the thicker the subducting plate, the more remained uplift. When the thickness of the subducting plate is zero, the subduction model coincides with the back-slip model (Kanda and Simons, 2010). Furthermore, I examine the effect due to the existence of the subducted seamount. Figure

4-9 shows the total displacement distributions when different shapes of seamounts are provided by changing (i) the dip angle of the leading flank and (ii) the depth. Independent of such parameters, the total displacement distributions show common features that the uplift and subsidence remain on the landward side and the trough-axis side, respectively, and the hinge point appears in the immediate vicinity of the top edge of the seamount indicated by triangles in Figure 4-9. The total displacement pattern depends on the shape of the subducted seamount as that a steeper flank causes a concentrated displacement and that the seamount places at the deeper part produce smaller and broader displacement.

Second, I explore the accumulated vertical displacement s with the recurrent ruptures on the multiple coupling patches. I set two coupling patches on the front and rear side of the leading flank of the subducted seamount, as shown in Figure 4-10a. I investigate the two patterns of rupture recurrence; in the first case, every event is a full rupture involving the two patches, and the interval time of the first rupture is twice as long as that of the second rupture (Figure 4-10b), and in the second case, every event has the same interval times, but the middle two events rupture only one patch (Figure 4-10e). Figures 4-10c and f show the distributions of the coseismic vertical displacement s. Figures 4-10d and f show the total vertical displacement between one event to the next event, which corresponds to the relative height of the uplifted coastlines. In the first case (Figures 4-10b–d), the amounts of coseismic displacement and relative height are proportional to the interval times; thus, the relative height of the coastline at the first event is twice higher than that of the second event. On the other hand, with the rupture segmentation (Figures 4-10e–g), because of the partial release of the accumulated shear stress on patch 1 without a significant surface displacement (the purple line in Figure 4-

a

b
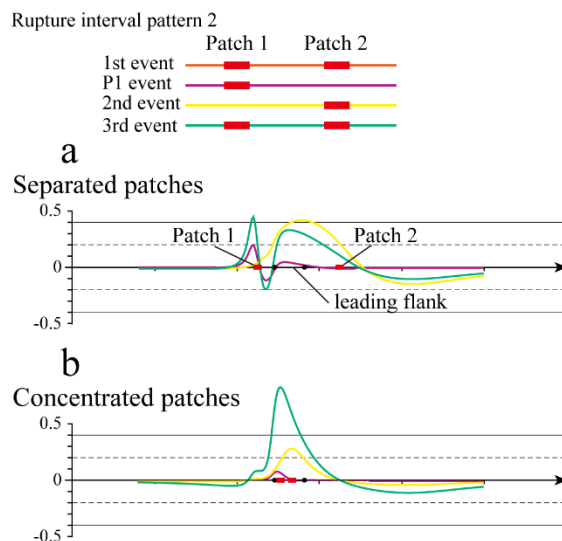
Figure 4-11. Examination result of the two-dimensional model comparing the coseismic surface displacements with different configurations of the coupling patches. The geometry and rupture scenario is same as the scenario 2 in Figure 4-5. (a) The distributions of the coseismic displacements when the coupling patches are separated. (b) The distributions of the coseismic displacements when the coupling patches concentrate on the leading flank of the subducted seamount.
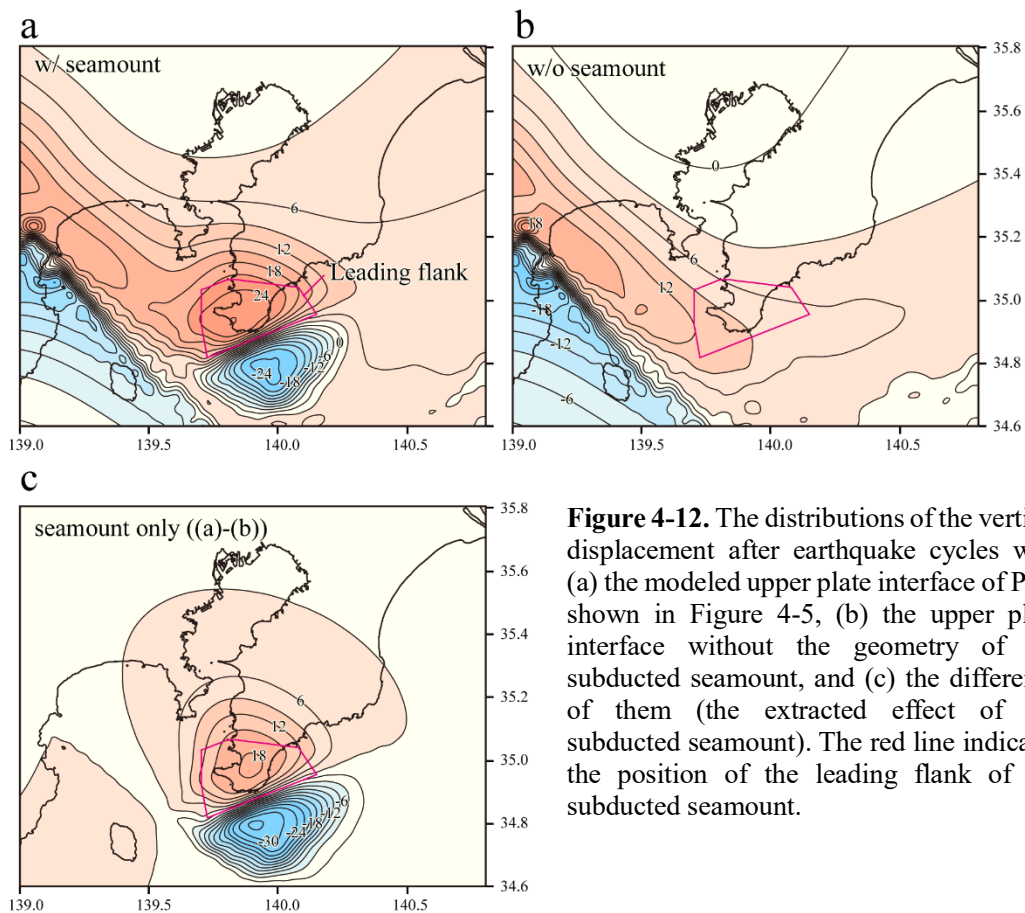
Figure 4-12. The distributions of the vertical displacement after earthquake cycles with (a) the modeled upper plate interface of PHS shown in Figure 4-5, (b) the upper plate interface without the geometry of the subducted seamount, and (c) the difference of them (the extracted effect of the subducted seamount). The red line indicates the position of the leading flank of the subducted seamount.

10f), the coseismic displacement amounts are comparable in the first and second events. Consequently, the relative height of the coastlines at the first and second events are not significantly changed despite the twice longer formation intervals.

Additionally, I examine how the remained elevation distribution changes depending on the configuration of the coupling patches. I tested two other configurations of the coupling patches; the first one is that both patches are located on the leading flank, and the second one is that two patches much separate from each other. Figure 4-11 shows the coseismic displacement distributions in each case. The geometry of the subducting plate is the same as Figure 4-10. This result shows that the separated patches still produced comparable amounts of coseismic displacements (Figure 4-11a), but, in the case of the closely-located patches, the coseismic displacement of the third event is twice higher than that of the second event (Figure 4-11b). This result suggests that the coseismic displacement in each event is strongly affected by the slip amount on the leading flank. The condition on the slip amount to be comparable for the second and third events is that patches 1 and 2 are located in the rear and front of the leading flank.

The examination with the two-dimensional model revealed that the mechanical boundary condition leads to the concentrated deformation pattern after earthquake cycles, different from the kinematic boundary condition. Especially, a local geometry on the upper plate interface like a subducted seamount causes a short-wavelength of long-term surface deformation (Figure 4-9). When multiple coupling patches have a different pattern of rupture intervals, the elevations of uplifted coastlines are not necessarily proportional to the rupture interval times (Figure 4-10). These results approximate the features of the Numa terraces indicated by the geological investigations.

4.4.2 Deformation distribution with a three-dimensional model

Next, I examine the long-term deformation due to the three-dimensional plate interface geometry. Figure 4-12 shows the vertical displacement distribution on the surface when 6,000 years of strain accumulation and release with a steady slip rate $V = 25$ [mm/yr] (DeMets et al. 1994). Figures 4-12a and b illustrate the displacement when the geometry of the subducting plate's upper surface has the local bump (Solid line in Figure 4-5a) and without it (Red broken line in Figure 4-5a), respectively. The surface displacement without the seamount (Figure 4-12b) shows a pattern parallel to the trough axis that uplift peak occurs on the landward side and huge subsidence occurs around the trough axis, which is also demonstrated by Kanda and Simons (2010). The larger uplift appears on the western side because of the higher dip angle, as demonstrated in the previous section, and the uplift to the east of the Boso Peninsula is small. The deformation distribution with a subducted seamount (Figure 4-12a) shows a large uplift concentration around the Awa region. Figure 4-12c shows the difference between them and thus represents the effect of the subducted seamount. The uplift peak positions above the leading flank of the subducted seamount.

4.4.3 Reproduction of the geomorphological observations with the modeled earthquake cycle

Finally, I search for the possible configuration of coupling patches and the rupture history to reproduce the current elevation distributions of the Numa terraces. I set two additional coupling patches other than the source of the Taisho-type events, around the Awa region as shown in Figure 4-13a, which place on the rear and front of the leading flank of the subducted seamount, considering the result of the 2-D model (Figure 4-11). Figure 4-13b shows the assumed rupture scenario of the coupling patches, found to be optimal after a set of trial and error. First, the northwestern side of the slip region (patches 1 and 2) rupture every 400 years, approximating the Taisho-type events (Shishikura, 14).
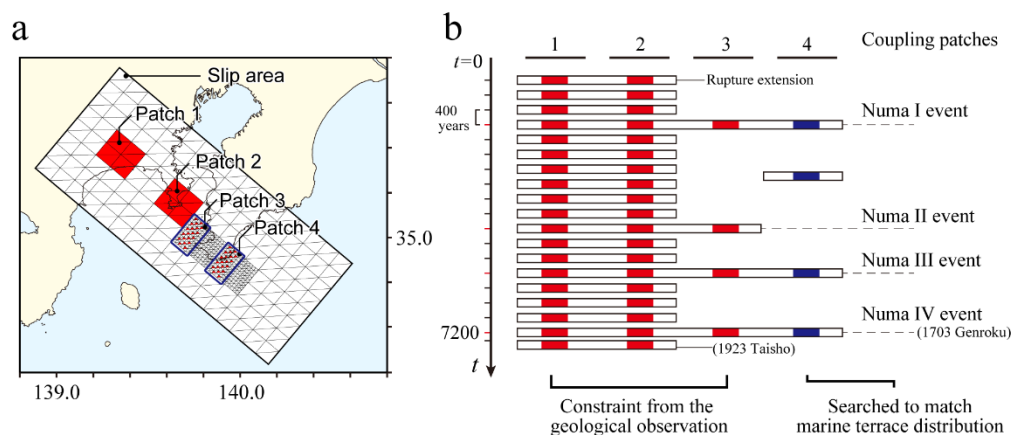
Figure 4-13. Specified rupture scenario for the reproduction of the marine terraces. (a) Positions of the coupling patches. The northwestern patches (patches 1 and 2) are determined to follow the estimated slip distribution of the 1923 event (Sato et al., 2005; Nyst et al., 2006). The southwestern patches (patches 3 and 4) are located rear and front of the leading flank of the subducted seamount. (b) The settings of the rupture timings and the extensions. The rupture timings of patches 1 to 3 are determined from the geological observations (red lines), and that of patch 4 is searched to match the observed marine terrace distribution.

On the other hand, the southeastern patches rupture at the timings of the formation ages of the Numa terraces. If I set the entire rupture for each Numa terrace formation event, the relative heights of the terraces are proportional to the formation interval times. Therefore, I set an isolated rupture of patch 4 at the timing between the Numa I and II events; this follows the rupture scenario 2 in the two-dimensional model examination (Figure 4-10). When this patch ruptures simultaneously to the Numa II event, the relative elevations of Numa II and III are proportional to the rupture interval times of patch 3, and the earlier this patch ruptures, the higher elevation of Numa III becomes. However, the deformation amount also depends on the coupling patch configuration and the plate geometry, and thus it is required to clarify that dependence to determine the particular timing of this rupture.

First, I investigate the modeled slip distribution and crustal deformations of the slip event representing the historical earthquakes. As displayed in Figure 4-13b, the last two events are the proxies of the historical 1923 Taisho and 1703 Genroku earthquakes. The 1923 event is set to occur 220 years after the full rupture and break patches 1 and 2. The 1703 event is a full rupture that occurs 400 years after the break of patches 1 and 2 and 1600 years after the southeast patches break. Figures 4-14a and b show the slip distributions of these events. The slip is concentrated in the ruptured coupling patches and expands in the decoupled zone. The moment magnitudes of these events are M_W 7.7 and 8.2, respectively, comparable to the estimated source by the previous studies. Figures 4-

76

14c and d are the calculated vertical displacement distributions on the ground surface. The simulated Genroku event (Figure 4-14d) produced huge uplift concentrate around the Awa region up to 6 meters. The hinge line, where no uplift and subsidence occur, places in the middle part of the Boso Peninsula. For the simulated Taisho event (Figure 4-14d), the maximum uplift places to the south of the Miura Peninsula, where the coupling patch 2 is located, consistent with the geodetic observation (Figure 1-2a).

Moreover, we can compare the interseismic slip and displacement with the modern instrumental observation via GNSS. Figure 4-15a shows the simulated interseismic slip deficit distribution in the coseismic slip area, which is derived by subtracting the interseismic slip rate from the steady slip rate V. This distribution is constant throughout all earthquake cycles. Note that this slip deficit distribution does not necessarily coincide with the coseismic slip distribution. Figure 4-15b shows the
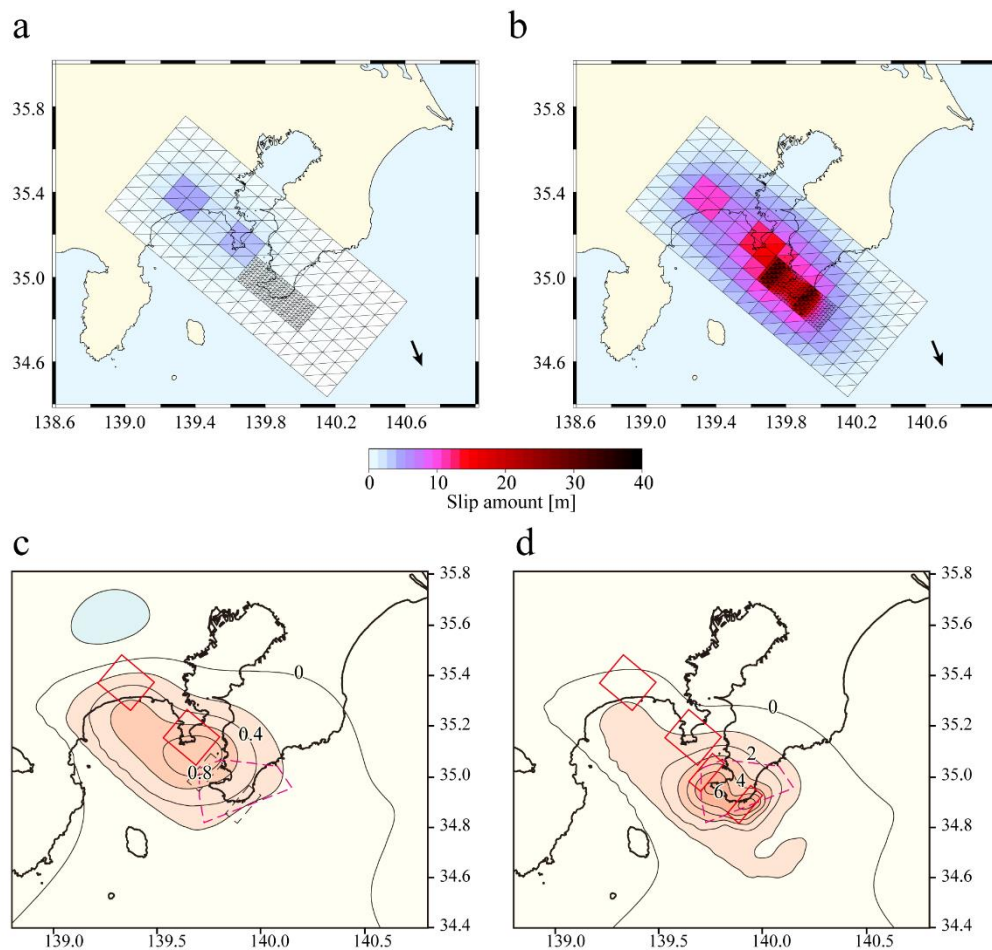
Figure 4-14. Simulated historical earthquakes in the rupture scenario. (a, b) The coseismic slip distributions of the proxies of the 1923 event (a) and the 1703 event (b). (c, d) The coseismic surface vertical displacement due to the proxies of the 1923 event (c) and the 1703 event (d).
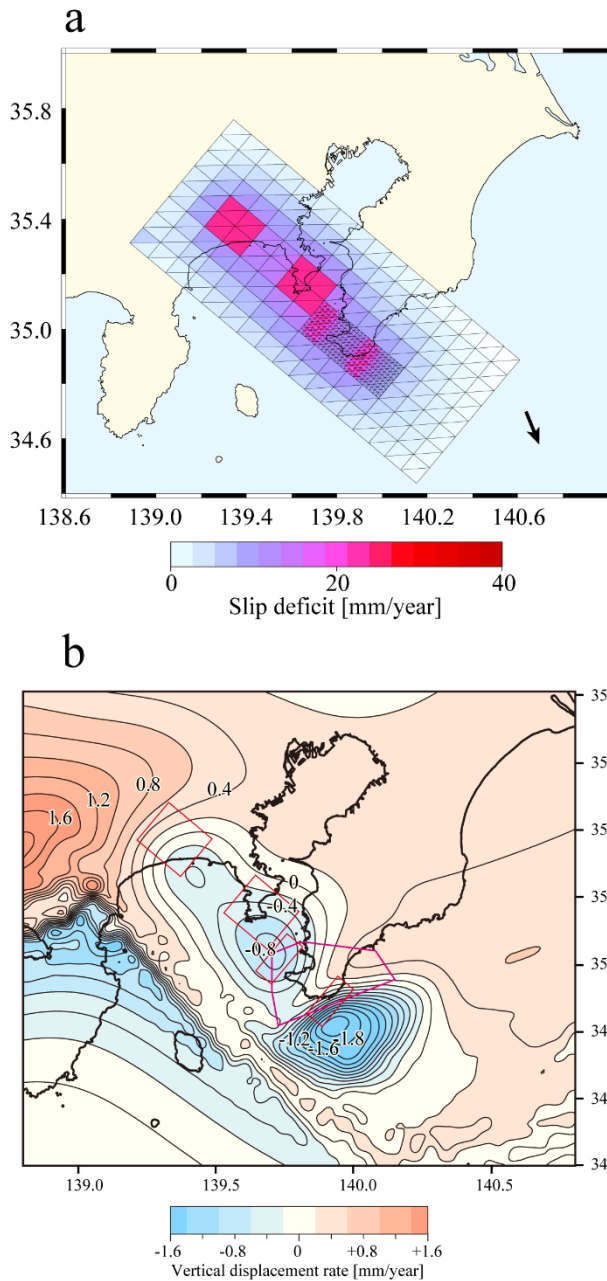
Figure 4-15. Modeled movement is the interseismic period. (a) The slip deficit distributions on the coseismic slip area. (b) The surface vertical displacement rate in the interseismic period.

simulated interseismic displacement rate on the ground surface. Compared with the modern GNSS observation result (Figure 1-2b), the horizontal displacement pattern almost corresponds to the observation, but the vertical displacement pattern does not fit in the Awa region. The reason for the consistency and inconsistency is discussed later.

Lastly, I calculate the elevation distributions of the modeled Numa terraces. Figure 4-16 shows the vertical displacement accumulated after each rupture of patch 3, which corresponds to the Numa terrace formation event. Each elevation distribution
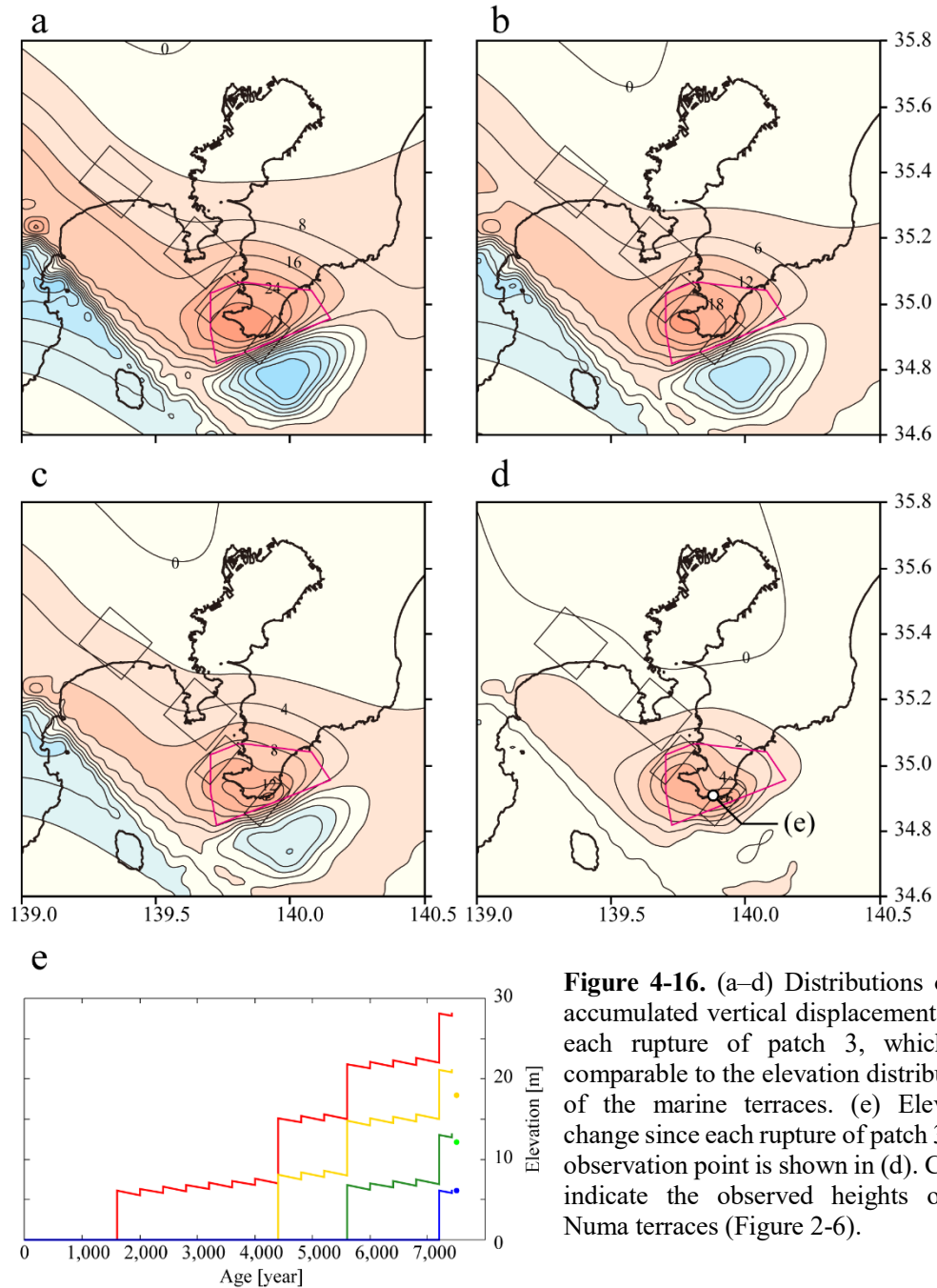
Figure 4-16. (a–d) Distributions of the accumulated vertical displacement since each rupture of patch 3, which are comparable to the elevation distributions of the marine terraces. (e) Elevation change since each rupture of patch 3. The observation point is shown in (d). Circles indicate the observed heights of the Numa terraces (Figure 2-6).

shows the concentration of uplift at the Awa region, and the peak amount of relative height is 6–8 meters in common. These characteristics follow the observed distributions of the Numa terraces. Figure 4-16e shows the time evolution of the elevation change at the observation point in the Awa region, starting from each rupture of patch 3. These curves demonstrate that the uplifted coastline does not go back to the sea-level again in this model; this is different from the results of the previous subduction models (Matsu'ura and Sato, 1989; Sato et al., 2016; Noda et al., 2018).

4.5 Discussion

I constructed a rupture scenario to explain the geomorphological observation with a newly developed mechanical subducting plate model. The reproduced elevation distributions of the modeled Numa terraces (Figure 4-16) follow the general characteristics of the result of the geomorphological investigation; the maximum relative heights at the Awa region of 6–7 meters and the short wavelength uplift concentration in the Awa region. However, because this scenario is produced by try-and-error searching, it might not be the unique solution to explain the geological/geomorphological observations. Next, I compare the model to the other observations for the validity examination.

Comparing the geodetic observation of the coseismic vertical displacement due to the 1923 Taisho earthquake (Figure 1-2a) and the modeled Taisho deformation (Figure 4-14c), the deformation pattern approximately follows the observation because the coupling patches 1 and 2 are set to imitate the slip concentration indicated by the previous inversion studies (Sato et al., 2006; Matsu'ura et al., 2007). However, the amplitude of the uplift amount and the released moment is smaller than the observation. The coseismic displacement amount is approximately proportional to the slip amount, which basically corresponds to the slip-deficit rate times the event interval. Several possible solutions can be considered here for this inconsistency. The first candidate is to enlarge the coupling patches 1 and 2. However, to release the moment comparable to that estimated by the inversion studies (Mw >7.8), it is required that almost the entire area of the coseismic slip region of the 1923 event is coupled. Second, the slip deficit rate possibly changes during the interseismic period. However, it might be less likely to consider that the plate convergence rate is twice faster than the present observation (DeMets et al., 1994). The other candidate is the possibility of remaining intact patch at the last rupture (i.e., the 1703 event). As discussed in the previous geological studies (Matsuda et al., 2014), the difference in the slip around the Sagami bay between the 1703 and 1923 events is arguable. If patch 2 is further divided into small patches and a small patch remained to be unbroken, the slip amount in the 1923 event can be much larger than in the model executed in this study. However, because the purpose of this study is landform change in the Boso Peninsula, I would not stick to reproduce the source slips of the historical earthquakes by excessively complicating the model.

Next, I compare the geodetic observation (Sagiya, 2004; Noda et al., 2013) and the modeled interseismic slip deficit and surface displacement (Figure 4-15). First, the modeled slip deficit rate (Figure 4-10a) approximately follows the estimation by the

inversion studies (Sagiya, 2004; Noda et al., 2013) but shows the split distribution. However, the inversion resolution depends on the density of the GNSS array and the focal depth, and thus it cannot detect the detailed patchy shape smaller than tens of kilometers if it is actually split. The interseismic surface displacement rate (Figure 4-15b) shows a characteristic distribution. The subsidence peaks are located on the upper edges of the coupling patches. Besides, extraordinary subsidence occurs above the trailing flank of the subducted seamount, as expected in the 2-D model (Figure 4-9). Although the subsidence pattern and the amplitude around the Sagami bay are consistent with the observation, the observed high subsidence rate in the south Boso Peninsula is not reproduced. The deformation of the Awa region is sensitive to the slip on the leading flank of the subducted seamount, just beneath there. In this configuration, I do not put a coupling patch here following the 2-D model examination (Figure 4-11). If we allow a more complicated configuration of the coupling patches, such as discussed in the 2-D examination (Figure 4-7), it might satisfy both the requirement of constant coseismic uplift (Figure 4-11) and the interseismic subsidence.

The modeled Numa terraces (Figure 4-16) approximately follow the geomorphological observation: peak uplift at the Awa region whose relative height is 6–7 meters and steeply decrease toward the north (Figure 4-2). Compared with the observed distribution (Figure 4-2), the uplift amplitude is comparable, but the deformation wavelength is rather broader than the observation; the relative height at Tateyama and Chikura is lower than the modeled terrace elevations. The deformation wavelength is sensitive to the geometry of the subducted seamount, as examined in the 2-D model (Figure 4-9); the steeper the dip angle of the leading flank, the shorter the surface deformation wavelength. The introduced geometry of the subducted seamount in this model is taken from the seismological survey (Tsumura et al., 2009) (Figure 4-1), but the estimation accuracy of the geometry has room for improvement. I do not target to determine the geometry of the plate interface in this study and thus do not conduct a parameter study to fit the observation, but further study will be required to reproduce those characteristics accurately by constraining the geometry of the subducted seamount.

The mechanical boundary condition introduced in this study strongly affected the relationship between the event interval times and the relative heights of the uplifted terraces (Figure 4-16). If we use the kinematic boundary condition, which assumes that the slip amount on each slip element is always proportional to the waiting time, the uplift amount is supposed to be almost proportional to the event interval times. The similar uplift amount at the Numa II and III events (Figure 4-16e) despite their different interval

times are affected by the slip amount between the coupling patches 3 and 4 (Figure 4-13a), where different slip distributions are expected with the kinematic and mechanical assumptions.

The elevation distribution of the modeled Numa IV terrace (Figure 4-16d) can have a different feature from the relative height distributions of the higher terraces. Because the interval time after the event is much shorter, the deformations due to the interseismic movement and the Taisho-type events less affect the final elevation distribution. Moreover, the deformation due to the last event, modeled Taisho event (Figure 4-14c), is included because the rebound in the interseismic period is not completed. In fact, the elevation distribution of Numa IV is slightly different from the higher terraces (Figure 2-6). However, this model expects that the final elevation of Numa IV will be dominated by the crustal change due to the rupture event of patch 3.

Finally, I compare the modeled long-term deformation pattern (Figure 4-12a) and other geological investigation results. Previously, Shishikura (2001) reported that uplifted Holocene seashore deposits are also confirmed in the middle to the north area of the Boso Peninsula, but it was inconsistent with the coseismic displacement distribution during the historical earthquakes (Shishikura, 2014). My model explains this inconsistency. The coseismic deformation pattern is dominantly affected by the positions of ruptured coupling patches (Figure 4-14). On the other hand, the long-term deformation pattern depends more strongly on the plate interface geometry (Figure 4-12). Therefore, the height distribution of the Holocene highest marine terrace shows a broader wavelength than the coseismic displacement. The modeled long-term deformation
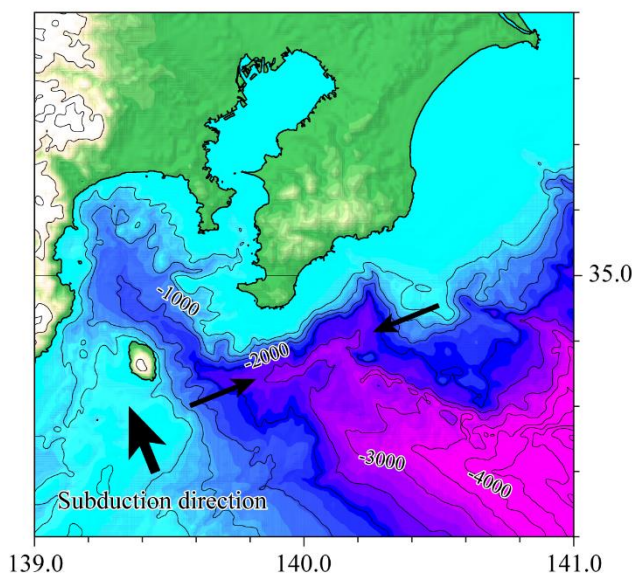
Figure 4-17. Elevation and bathymetry map around the survey region. The contour interval is 500 meters. The digital elevation model is from ETOPO1 Global Relief Model (Amante and Eakins, 2009).

distribution in this model (Figure 4-12a) shows quite comparable distribution to the Holocene highest marine terrace (Shishikura, 2014).

This study revealed that the landform in the Awa region is strongly affected by the subducted seamount beneath there. On the other hand, the modeled surface displacement also predicted long-term subsidence offshore Boso, above the trailing flank of the subducted seamount. The bathymetry map (Figure 4-17) shows trough-like submarine topography directs ENE, which is distorted from the feature of the Sagami Trough. Kasahara et al. (1973) and Matsuda et al. (1978) pointed out this feature and considered it the surface expression of an active thrust fault. However, subsequent structural surveys (e.g., Sato et al., 2006; Tsumura et al., 2009) did not detect any fault whose strike is parallel to this topography. Here, I can propose that this distorted trough geometry was also formed due to the seamount subduction. The depth of the trough is 2,000–3,000 meters, which is equivalent to half a million years of subsidence expected in our model over a simple extrapolation and reasonable to the time-scale of the Sagami Trough formation. For complete modeling, other processes are still needed to be considered, such as shifting of the seamount position, inelastic deformation around the subducted seamount (Wang and Bilek, 2011), and sedimentation. However, it is suggestive that the analog experiments (Dominguez et al., 1998; 2000) of seamount subduction and the structural survey in the Nankai Trough (Park et al., 1999) showed subsidence remained behind the seamount.

5. General discussion

The geomorphological survey in this study that employed feature extraction and its grouping method improved the objectivity of the terrace classification in the Awa region. In the subsequent analysis, I assumed that the past sea-level elevation, indicating the total uplift amount after the emergence, corresponds to the paleo-shoreline angle, the inner-edge of the terrace platform. However, as Kayanne and Yoshikawa (1986) suggested, a more detailed geomorphological investigation is required to determine what coastal landform precisely indicates the mean sea-level and how such landform suffers degradation and weathering after emergence. As for the Numa terraces, even if it is required to reevaluate the elevation distribution of the Numa terraces (Figure 4-2), the amplitudes might be changed up to a few meters. However, the overall pattern (wavelength) is not changed because the robustness of the classification is supposed. In other words, the estimated sea-levels are equally shifted by the same amount over the area. Therefore, the subsequent analysis of the kinematic modeling still maintains validity.

Many previous studies suggested the existence of small cliff landforms between the major cliffs of the Numa terraces, which likely indicate the uplifts due to the Taisho-type earthquakes (Kayanne and Yoshikwa, 1986; Uesawa and Miyakawa, 2015). On the other hand, the result of the mechanical examination in this study (Figure 4-16e) suggests that the uplifts due to the Taisho-type earthquakes mostly decrease in the interseismic period, and their final heights are relatively small than the reports by the geological studies. These smaller cliffs need further examination in the future for the discussion of the detailed rupture history along the Sagami Trough, including kinematic and mechanical simulations with a higher resolution and the geomorphological reevaluation of whether they have lateral continuity like the Numa terraces.

For more in-depth discussions with the mechanical subduction model, it is required to enlarge the geological and geomorphological dataset. In this study, the survey region of the geomorphological analysis was limited between the Tateyama and Chikura lowlands. However, the marine terraces are reported to be distributed beyond this coast to the north and in the Miura Peninsula. The kinematic model predicted that the relative heights of the uplifted coasts tend to be proportional to the interval times as farther away from the Awa region (Figure 4-12). Therefore, the relationship between the terrace elevation and formation age in the middle Boso Peninsula and Miura Peninsula is possibly another strong constraint for the rupture scenario.

In this study, the dating analysis employed the newly assumed sedimentation model and estimated the terrace formation ages more quantitatively. In constructing the sedimentation model, I simplified the structure of the sedimentary terraces to be impartial within each level of the terrace. However, the actual structure is supposed to include a more complicated distribution of the sediments, such as vertical and horizontal heterogeneity accompanying the coastal development and minor crustal deformation events (e.g., Taisho-type events), which might be highly site-specific. Moreover, as discussed above, the relationship between the appearance of the shell fossils and their ages is another essential parameter for the terrace age estimation. The concept of my model that represents the sediment age distribution with the model parameters of the sedimentation process can expand to a more complicated sedimentation structure if further investigation increases the number of dating samples and determine the sedimentation model.

The rupture scenario constructed by the newly developed mechanical subduction model in this study proposed that the elevation distribution of the Numa terraces is possibly explained by the interaction of subducted seamount and the rupture segmentation beneath the Boso Peninsula. However, this scenario contains arbitrariness and allows a possibility of another deformation scenario. Specifically, the configuration of the coupling patches in the southwestern part of the slip region has much uncertainty to be determined. Moreover, the inland faults and the plastic deformation in the hanging wall (Wang and Bilek, 2011) are not included in this study and possibly modify the deformation process and stress condition on the plate interface. The examination result in this study implies that the different slip angle between the large-scale plate subduction and the local slip direction cause the long-term surface vertical deformation, and thus it might be explained with a splay fault. However, the kinematically supported example that reproduces Numa terrace distribution associated to the coseismic uplifts at least disproved the assertion that the coseismic uplifts inevitably vanish during the interseismic period by the previous studies (Matsu'ura and Sato, 1989; Sato et al., 2016; Noda et al., 2018).

Finally, I discuss the updates about the understanding of the recurrence history of the Kanto earthquakes. Previously, as summarized by Shishikrua (2014), the Kanto earthquakes are considered to comprise two types of rupture, Taisho-type, and Genroku-type earthquakes, which rupture only the northwestern region with 200–400 years' interval and the whole coupled region with 2,000–2,700 years' interval, respectively. The proposed scenario in this study suggested that the previously assumed 'Genroku-type earthquakes' had a variation in the rupture extent and interval time. Moreover, the

possibility of the isolated rupture of the eastern patch was suggested. In the rupture scenario of this study, I fixed the recurrence of 'Taisho-type earthquakes,' which rupture only two northwestern patches with 400 years' interval. However, following the estimation about the eastern patch behavior, the variation in the 'Taisho-type earthquakes' is also possible. In this study, I did not discuss the coupling patches possibly located east of the Boso Peninsula, which generate a tsunami in the 1703 Genroku earthquake (Matsuda et al., 1978; Namegaya et al., 2011; Yanagisawa and Goto, 2017). Considering the mechanical coupling, this part of rupture is supposed to affect the stress condition in the region discussed in this study, but the available dataset, for now, cannot constraint any property of this part before the historical events.

The major interest in the Kanto earthquakes is whether the rupture of the Sagami Trough has some recurrence pattern or not (Philibosian and Meltzner, 2020). At least, the geological evidence suggests that the western and eastern parts of the Sagami Trough can have different rupture interval times on average, which correspond to 'Superimposed cycles' in Philibosian and Meltzner (2020). On the other hand, it was suggested that the variable rupture pattern could exist within each part. However, if the similarity in the Numa terraces height, which implies the constant slip amount on the leading flank of a subducted seamount in each event, is determined by some kinematic background, the occurrence interval also might follow some law. Future studies, for example, the quasi-dynamic earthquake recurrence model (e.g., Hori and Miyazaki, 2011) and the paleoseismological survey in the other region, will improve the understanding of this region. Additionally, the behaviors on and around subducted seamounts have been a subject of study in many places, such as the deformation in the forearc structure (Park et al., 1999; Gardner et al., 2001; Okamura and Shishikura, 2020) and the effects on the coupling conditions (Mochizuki et al., 2008; Sun et al., 2020). The results of this study are also expected to contribute to the studies in other coastal regions.

6. Summary

I re-investigated the Numa terraces, which are the Holocene uplifted marine terraces distributed in the southernmost part of the Boso Peninsula, and reevaluate the occurrence history of the Kanto earthquakes using newly developed mechanical models for plate subduction and earthquake recurrence. As for the geological and geomorphological studies on the Numa terraces, I newly developed computational and statistical methods and obtained a quantitative dataset indicating the formation ages and the elevation distributions. Using these datasets as the observation value, I proposed a

rupture scenario on the plate interface of the Sagami Trough in the past 7,000 years to explain the current distribution of the Numa terraces.

For the evaluation of the Numa terrace distribution, I introduced the computational method comprises the cliff extraction and the grouping into generation and quantitatively obtained the elevation distributions of the four levels of the terraces continuously for the first time. The obtained elevation distributions show the consistent pattern that reaches a peak of 6–8 meters in relative height and steeply decreases toward the north. They are similar to the coseismic uplift distribution due to the 1703 earthquake and imply the cumulativeness of coseismic deformation.

For the dating investigation, I constructed a comprehensive dataset of the dating results in the Numa terraces by compiling the previously conducted surveys and newly obtained results in this study. I newly developed a statistical estimation method for the terrace emergence ages using the Bayesian method with this dataset. As a result, the emergence ages were constrained within a few hundred years. This constraint successfully estimated the younger limit of the emergence ages for the first time, which was the major difficulty in the previous studies. The newly estimated emergence ages are 5655 yBP, 3200 yBP, 1950 yBP, and CE1703 in descending order, and their interval times are widely varied. This result updated the long-accepted estimation by the previous investigations (Nakata et al., 1980; Fujiwara et al., 1999). The combining results of the geomorphological and geological investigations revealed that the Numa terraces have comparable relative heights in the southernmost part of the Boso Peninsula, while they have different formation intervals almost twice as long.

I construct a new plate subduction model by combining the elastic plate subducting model and the mechanical coupling model and discussed the rupture scenario of the past Kanto earthquakes. Most of the previous kinematic models of the paleo-earthquakes assume a back-slip model that does not preserve coseismic deformation after an earthquake cycle. The new model reproduced the permanent uplift associates with the local structure on the plate interface. The rupture scenario I proposed in this study assumed four coupling patches on the plate interface and reproduced the present distribution of the Numa terraces with variable rupture intervals and extent over the coupling patches. This result disproved the assertion by the previous studies that the coseismic uplift inevitably vanishes during the interseismic period. The rupture scenario of the Kanto earthquake became less periodic than the previous assumption, and this new scenario has a mechanical basis, consistently explains the geologic and geomorphologic observations.

Acknowledgments

I would like to express my special appreciation and thanks to Prof. Ryosuke Ando, my Ph.D. supervisor, for having been a tremendous mentor for me for six years. I could not thank him enough for improving my research ability from the basics, giving me plenty of opportunities, and encouraging me to persist in the study. This dissertation was improved thanks to his thoughtful and thorough reviews.

I am also grateful to Prof. Masanobu Shishikura for data provision, cooperation in field surveys, and valuable discussions. He provided me the digital elevation model used in this study and unpublished sampling and dating results in Tateyama (SN, KB, and TK sampling points).

Also, I would like to thank Prof. Yusuke Yokoyama, Dr. Y. Miyairi, Ms. Y. Ando, and Mr. N. Fukuyo for the cooperation on the radiocarbon dating measurement and valuable discussions concerning section 3.

I appreciate helpful reviews from the referees, Prof. Kenji Satake, Prof. Hajime Kayanne, Prof. Tatsuya Ishiyama, Prof. Yosuke Aoki, and Prof, Toshihiko Sugai.

Moreover, I wish to acknowledge fruitful discussions and advice with Prof. Satoshi Ide and my outstanding research group members, Dr. N. Aso, Dr. P. Romanet, Dr. A. Toh, Dr. S. Yabe, Dr. T. Nishikawa, Dr. D. Sato, Dr. N. Mizuno, Mr. Y. Yamaguchi, Mr. T.W. Chang, Mr. S. Ozawa, Mr. K. Uemura, Ms. M. Aso, Ms. L. Kaneko, Mr. K. Suzuki, Mr. R.O.P. Martínez, Mr. T. Hisakawa, Mr. R. Namiki, Mr. K. Masuda. Mr. T. Iida and Mr. K. Muramatsu.

I would like to thank Prof. Kerry Sieh and Prof. Aron Meltzner for valuable advice on my study. My experiences of field investigations and interactions with them made this dissertation highly improved.

At last, I would like to give a special thanks to my friends, S. Shibata, T. Okuda, S. Tan, T. Kanzaki, M. Ozawa, and N. Noda, for their encouragement and for always supporting me.

Appendices

Appendix A: Formulation for the center lines of the cluster points

The redrawing of center lines (equation (2-2)) can be solved linearly by the least-squares method. When vectors $\mathbf{Y}_k$ (the observation vector represents the elevations of the data points) and $\mathbf{A}_k$ (the model parameter vector represents the intercept and slope of the center line) and a matrix $\mathbf{G}_k$ are given by

$$\mathbf{Y}_k = (r_{1k}d_1^z \quad r_{2k}d_2^z \quad \cdots r_{Nk}d_N^z)^{\mathrm{T}}$$

$$\mathbf{G}_k = \begin{pmatrix} r_{1k}d_1^x & r_{1k} \\ r_{2k}d_2^x & r_{2k} \\ \vdots & \\ r_{Nk}d_N^x & r_{Nk} \end{pmatrix}$$

$$\mathbf{A}_k = (a_k \quad b_k)^{\mathrm{T}},$$

the observation equation for the k-th center line is $\mathbf{Y}_k = \mathbf{G}_k\mathbf{A}_k + \boldsymbol{e}_k$ ($\boldsymbol{e}$ is an error vector), and thus the optimal parameters of the lines are calculated as

$$\mathbf{A}_k = \left(\mathbf{G}_k^{\mathrm{T}}\mathbf{G}_k\right)^{-1}\mathbf{G}_k^{\mathrm{T}}\mathbf{Y}_k \tag{A1}$$

For the constraint of parallel center lines (equation (4)), I calculate vector $\mathbf{B} = (a \quad b_1 \quad b_2 \quad \cdots b_K)^{\mathrm{T}}$ minimizing the error in

$$\mathbf{Z} = \mathbf{HB} + \boldsymbol{e}_k \tag{A2}$$

Where the observation vector $\mathbf{Z}$ (N) and the matrix $\mathbf{H}$ (N × K + 1) is given as

$$\mathbf{Z} = (d_1^z \quad d_2^z \cdots d_N^z)^{\mathrm{T}}$$

$$\mathbf{H}_{in} = \begin{cases} d_n^x & (i = 1) \\ r_{n(i-1)} & (2 \leq i \leq K + 1) \end{cases}$$

The objective vector $\mathbf{B}$ is linearly solved by

$$\mathbf{B} = (\mathbf{H}^{\mathrm{T}}\mathbf{H})^{-1}\mathbf{H}^{\mathrm{T}}\mathbf{Z}. \tag{A3}$$

In addition, it should be noted that the iteration in K-means clustering has initial value dependency. In this study, I set random initial clusters 200 times to prevent the solution from falling into local minimums.

Appendix B: Diffusion equation and curvature of cliff bases decaying on time

The 1-D diffusion equation for a quantity $u(t,x)$ varying with the time t and space z is generally given by

$$\frac{\partial u(t,x)}{\partial t} = \kappa \frac{\partial^2 u(t,x)}{\partial x} \tag{B1}$$

Here, κ is a diffusion coefficient. When I set the initial condition, $D(0,z)$, to be a delta function centered at $z = \mu$, the solution becomes the well-known normal distribution form as

$$u(t,x) = \frac{1}{2\sqrt{\pi\kappa t}} \exp\left(-\left(\frac{x-\mu}{2\sqrt{\kappa t}}\right)^2\right). \tag{B2}$$

with standard deviation σ corresponding to $\sigma = \sqrt{2\kappa t}$, which is an increasing function of time t.

Next, I consider a mathematical model to describe the decay of the curvature of the paleo-shoreline angle as the function of time. I consider the initial topography is given by the unit step function $u(0,x) = \mathrm{stf}(x)$ to mimic a marine terrace, where $\mathrm{stf}(x) = 1$ for $x<0$ and $=0$ for $x>0$. An analytic convolution method shows that the topographic change governed by the diffusion equation is described by the error function as

$$u(t,x) = \int_{-\infty}^{\infty} \frac{1}{2\sqrt{\pi\kappa t}} e^{-\frac{\xi^2}{4\kappa t}} \mathrm{stf}(x-\xi)d\xi = \frac{1}{2}\left(1 + \mathrm{erf}\left(\frac{x}{2\sqrt{\kappa t}}\right)\right). \tag{B3}$$

The curvature follows the second derivative of the error function obtained as

$$\frac{\partial^2 u}{\partial x^2} = -\frac{x}{4\sqrt{\pi}(\kappa t)^{3/2}} \exp\left(-\frac{x^2}{4kt}\right). \tag{B4}$$

By evaluating the derivative of $\partial^2 u/\partial x^2$ and the identity,

$$\frac{\partial^3 u}{\partial x^3} = \frac{1}{4\sqrt{\pi}}(\kappa t)^{3/2}\left(\frac{x^2}{2\kappa t} - 1\right)e^{-\frac{x^2}{4\kappa t}} = 0, \tag{B5}$$

the temporal progress of the peak value of $\partial^2 u/\partial x^2$ appearing at $x = -\sqrt{2\kappa t}$ is given as

$$\max\left[\frac{\partial^2 u}{\partial x^2}\right] = \frac{1}{2\sqrt{2e\pi}}\frac{1}{\kappa t}. \tag{B6}$$

Hence, the curvature at the cliff base becomes proportional to t^{-1}.

Appendix C: Evaluation of the marine reservoir effect

The site-specific marine reservoir correction value, ΔR, is estimated by the measured radiocarbon age of a marine organism whose living date (older than CE 1940s) is determined, such as historically collected materials and dated materials via other dating methods (e.g., Hirabayashi et al., 2017). In the surrounding coast of the Sagami Trough, the fossilized sessile assemblage uplifted at the timing of the historical earthquakes (1923 Taisho and 1703 Genroku) can be obtained, and ΔR value has been evaluated based on their dating results. Shishikura et al. (2007) and Komori et al. (2017) previously collected the fossils associated with the historical uplifts and evaluated ΔR in the Miura and Boso peninsulas. However, the calibration curve (Heaton et al., 2020) was updated after the estimation, and it is required to reevaluate the ΔR value. Figure A1 shows the calibrated probability density functions of the samples of Shishikura et al. (2007) and Komori et al. (2017) with temporary ΔR values of -100 to -200 years. The appropriately calibrated dates are supposed to match the ages of the historical earthquakes (247 yBP and 27 yBP). According to this result, I evaluate the ΔR value around the Boso peninsula to be -150 ± 50 years.
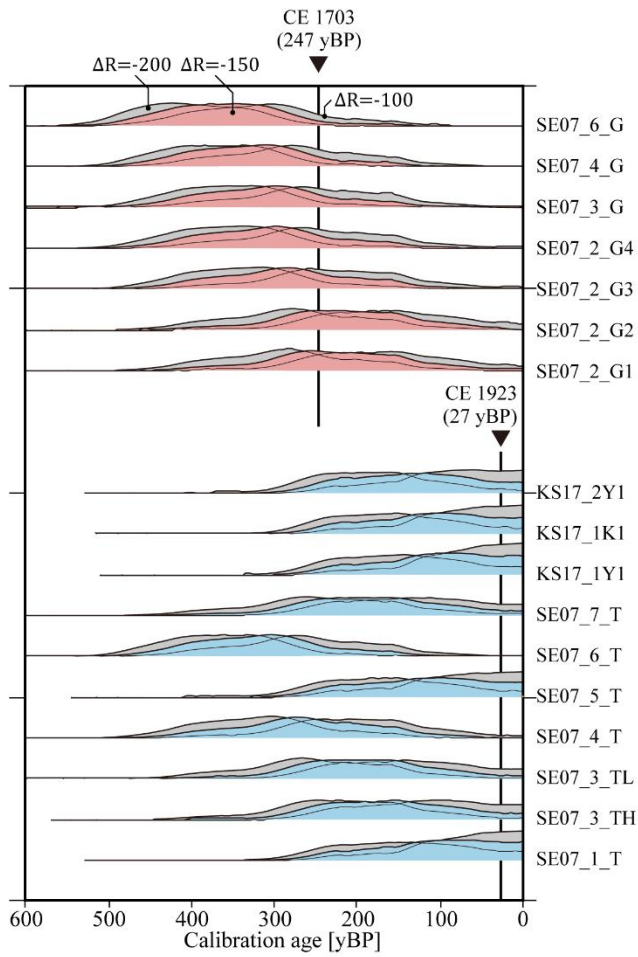
Figure A1. Calibrated probability densities of the coseismic uplifted samples in historical earthquakes from Shishikura et al. (2007) and Komori et al. (2017). Red- and blue-filled curves are samples associated with the 1703 Genroku and 1923 Taisho earthquakes, respectively, calibrated with ΔR=-150. The grey-filled curves are calibrated with ΔR=-200 and -100. Vertical bars indicate the ages of historical earthquakes.

Table S-1. Sampling points and sampling methods for all data

Region	Point name	Surface elevation [m a.s.l.]	Classification	Sampling depth [m]	Longitude E°/'/"			Latitude N°/'/"			Sampling Method	marine /terrestrial /NR	samples	# of dated samples	Reference
Chikura	CKR-N01	23.06	I	6.0	139	57	21.41	34	58	56.85	Machine Coring	2	0	0	Komori et al. (2017)
	CKR-N02	18.87	I	6.0	139	57	34.31	34	58	52.85	Machine Coring	5	0	0	
	CKR-N03	14.50	II	6.0	139	57	41.36	34	58	49.05	Machine Coring	5	0	0	
	CKR-N03'	13.75	II	6.0	139	57	43.21	34	58	48.87	Machine Coring	5	0	0	
	CKR-N04	9.10	III	6.0	139	57	46.23	34	58	43.90	Machine Coring	5	0	0	
	CKR-N05	8.51	III	6.0	139	57	48.80	34	58	42.51	Machine Coring	5	0	0	
	CKR-N06	3.87	IV	6.0	139	57	46.73	34	58	32.13	Machine Coring	5	0	0	
	CKR-S01	21.49	I	6.0	139	57	17.22	34	58	29.40	Machine Coring	3	0	0	
	CKR-S02	16.66	II	5.0	139	57	19.74	34	58	19.46	Machine Coring	4	0	0	
	CKR-S03	15.72	II	2.0	139	57	22.56	34	58	18.54	Machine Coring	4	0	0	
	CKR-S03'	15.77	II	5.5	139	57	23.46	34	58	20.84	Machine Coring	3	0	0	
	CKR-S04	10.45	III	2.0	139	57	29.53	34	58	16.90	Machine Coring	0	0	0	
	CKR-S04'	10.44	III	1.0	139	57	29.58	34	58	16.89	Machine Coring	0	0	0	
	CKR-S04"	10.36	III	6.0	139	57	30.36	34	58	19.26	Machine Coring	4	0	0	
	CKR-S05	10.00	III	7.6	139	57	34.88	34	58	22.00	Machine Coring	3	0	0	
	CKR-S06	3.87	IV	7.0	139	57	38.21	34	58	20.59	Machine Coring	2	0	0	
	CKR-M01	15.5	II	2.0	139	57	30.34	34	58	36.52	Geoslicer	1	0	0	This study
	CKR-M02	15.5	II	1.6	139	57	30.13	34	58	36.35	Geoslicer	0	0	0	
	CKR-M03	6.5	III	2.0	139	57	41.13	34	58	33.22	Geoslicer	0	0	0	
	CKR-M04	6.5	III	1.7	139	57	41.05	34	58	33.58	Geoslicer	1	0	0	
	CKR-M05	7.0	III	1.9	139	57	41.10	34	58	33.96	Geoslicer	0	0	0	
	CKR-M06	7.0	III	1.4	139	57	41.22	34	58	34.33	Geoslicer	0	0	0	
	STH01	4.60	IV	1.8	139	57	41.78	34	58	19.29	Geoslicer	3	0	0	
	STH02	4.42	IV	1.8	139	57	42.00	34	58	19.28	Geoslicer	2	0	0	
	STH03	4.34	IV	1.8	139	57	42.22	34	58	19.27	Geoslicer	2	0	0	
	STH04	4.31	IV	1.6	139	57	42.58	34	58	19.24	Geoslicer	1	0	0	
	C-Loc.02	23.5	I	2.6							Machine Coring	0	1	0	Uno et al. (2007)
	C-Loc.07	15.1	II	2.0							Machine Coring	1	0	0	
	C-Loc.08	15.3	II	2.0							Machine Coring	1	0	0	

Region	Sample										Method				Reference
Tateyama	C-Loc. 09	9.2	III	1.0							Machine Coring	1	0	0	
	C-Loc. 11	9.0	III	2.0							Machine Coring	1	0	0	
	TY01	12.10	II	4.0	139	52	47.12	34	59	51.63	Geoslicer	0	3	0	Shishikura et al. (2005)
	TY02	12.20	II	4.0	139	52	53.03	34	59	50.53	Geoslicer	2	4	0	
	TYM-3	9.43	III	4.0	139	52	23.80	35	1	15.97	Machine Coring	0	1	0	Shishikura et al. (2014a)
	TYM-4	9.07	III	4.0	139	52	16.15	35	1	18.13	Machine Coring	0	1	0	
	TYM-5	5.96	III	2.5	139	52	12.35	35	1	13.61	Machine Coring	0	1	0	
	TYM-6	5.34	IV	7.0	139	51	51.57	35	1	1.59	Machine Coring	1	1	0	
	TYM-7	5.44	IV	5.0	139	51	39.37	35	1	8.39	Machine Coring	1	0	0	This study
	SN-1	18.50	I	6.0	139	55	2.40	35	0	11.38	Machine Coring	1	1	0	
	SN-2	18.25	I	6.0	139	54	57.79	35	0	9.47	Machine Coring	1	1	0	
	KB-1	15.09	II	6.0	139	53	12.95	34	59	44.62	Machine Coring	1	1	0	
	KB-2	13.30	II	6.0	139	53	8.24	34	59	45.33	Machine Coring	1	1	0	
	TK-1	7.40	III	6.0	139	52	29.76	35	0	12.45	Machine Coring	1	1	0	
	TK-2	5.66	III	6.0	139	52	24.06	35	0	12.64	Machine Coring	2	0	0	
	GS1	1.70	IV	4.4	139	51	38.44	35	1	3.39	Geoslicer	4	0	5	Fujiwara et al. (2006)
	GS2	1.90	IV	3.4	139	51	32.17	35	1	2.13	Geoslicer	4	0	5	Fujiwara et al. (2010)
	TB3	1.99	III	6.7	139	52	27.23	35	0	46.73	Machine Coring	8	0	0	Fujiwara et al. (1999)
	TB4	1.43	III	8.9	139	52	3.62	35	0	27.00	Machine Coring	13	0	0	
	TB6	1.83	III	9.2	139	52	10.22	35	0	12.82	Machine Coring	10	0	0	
Koyatsu	Heguri River	N/A	N/A	N/A							Outcrop	48	0	0	Fujiwara et al. (1997)
	KYT-1	5.92	III	5.9	139	49	6.60	34	58	31.30	Machine Coring	2	1	0	Shishikura et al. (2014a)
	KYT-2	5.94	III	5.9	139	49	7.21	34	58	31.79	Machine Coring	0	3	0	
	KYT-3	6.71	III	6.7	139	49	7.75	34	58	29.98	Machine Coring	0	1	0	
	KYT-4	6.91	III	6.9	139	49	7.92	34	58	29.70	Machine Coring	1	0	0	
	KYT-5	6.92	III	6.9	139	49	8.55	34	58	30.09	Machine Coring	2	0	0	
	KYT-6	7.44	III	7.4	139	49	8.34	34	58	28.12	Machine Coring	0	0	0	
	KYT-7	7.62	III	7.6	139	49	9.75	34	58	27.91	Machine Coring	0	1	0	
	KYT-8	7.65	III	7.7	139	49	10.27	34	58	27.42	Machine Coring	1	0	0	
	KYT-9	8.68	III	8.7	139	49	12.60	34	58	27.24	Machine Coring	1	1	0	
Tomiura	TM01	3.90	III	3.5	139	49	42.02	35	2	11.52	Geoslicer	0	2	0	Shishikura et al. (2005)
	TM02	3.90	III	2.8	139	49	44.65	35	2	11.71	Geoslicer	0	2	0	

Heisa-ura	HSNS 01	21.51	II	1.5	139	50	17.45	34	56	21.52	Geoslicer	0	0	0	This study
	HSNS 02	19.54	II	1.8	139	50	13.95	34	56	19.71	Geoslicer	1	0	0	
	HSNS 03	18.63	II	1.6	139	50	10.38	34	56	18.42	Geoslicer	0	0	0	
	HSNS 04	16.59	II	1.3	139	50	6.12	34	56	16.25	Geoslicer	1	0	0	
	HSNS 05	14.56	II	1.1	139	50	2.24	34	56	13.89	Geoslicer	2	0	0	
	HSNS 06	13.95	II	1.8	139	49	59.73	34	56	13.84	Geoslicer	2	0	0	
	HSNS 07	13.37	II	1.2	139	49	56.76	34	56	15.52	Geoslicer Hand-auger	2	0	0	
	HSNH 01	15.18	II	1.5	139	50	5.50	34	56	12.96	Hand-auger	2	0	0	
	HSNS 08	8.93	III	1.1	139	49	50.54	34	56	7.50	Geoslicer	1	0	0	
	HSNS 09	7.94	III	1.3	139	49	49.64	34	56	7.25	Geoslicer	2	0	0	
	HSNS 10	7.63	III	1.3	139	49	48.24	34	56	6.73	Geoslicer	2	0	0	
	HSNS 11	7.32	III	1.3	139	49	46.64	34	56	6.16	Geoslicer	2	0	0	
	HSNH 02	6.3	IV	1.5	139	49	41.4	34	56	4.9	Hand-auger	2	0	0	
	HSNH 03	3.5	IV	1.5	139	49	38.0	34	56	1.8	Hand-auger	1	0	0	
	ALH01	3.21	IV	1.6	139	49	32.14	34	56	2.40	Geoslicer	4	0	0	
	ALH02	3.14	IV	1.5	139	49	32.61	34	56	2.86	Geoslicer	3	0	0	
	ALH03	2.68	IV	1.8	139	49	29.24	34	56	5.11	Geoslicer	4	0	0	
	HSNH 15	3.5	IV	1.8	139	49	22.6	34	56	12.0	Hand-auger	1	0	0	
	Tomoe River	N/A	N/A	N/A							Outcrop	14	0	0	Fujiwara et al. (1997)
Onjuku	ONJ-1										Geoslicer	1	0	0	Shishikura et al. (2014)
	ONJ-2										Geoslicer	1	0	0	
	ONJ-7										Geoslicer	0	2	0	
Iwai	IW01										Geoslicer	1	0	0	Shishikura et al. (2005)
	IW02										Geoslicer	3	2	0	
												22	3	1	
												6	2	0	

Table S-2. Dating results for coring samples

Region	Sample_name	Core_name	elevation (m a.s.l.)	material	Level	14C age		Calibrated age (95.4 % c.i.)*			Reference
Chikura	N01361	CKR-N01	19.5	shell	I	6044	±34	6632	-	6255	Komori et al.
	N01441	CKR-N01	18.7	shell	I	6226	±26	6830	-	6429	(2017)
	N02300A	CKR-N02	15.9	shell	I	5676	±29	6245	-	5870	
	N02465	CKR-N02	14.3	shell	I	6191	±26	6783	-	6392	
	N02480B	CKR-N02	14.1	shell	I	6119	±25	6695	-	6311	
	N02530B	CKR-N02	13.6	shell	I	6124	±29	6706	-	6317	
	N02595	CKR-N02	13.0	shell	I	6303	±24	6920	-	6516	
	N03170A	CKR-N03	12.8	shell	II	4215	±28	4520	-	4090	
	N03180	CKR-N03	12.7	shell	II	4299	±23	4650	-	4200	
	N03410B	CKR-N03	10.4	shell	II	5481	±29	6000	-	5610	
	N03515B	CKR-N03	9.4	shell	II	5898	±41	6478	-	6073	
	N03566	CKR-N03	8.9	shell	II	6408	±29	7048	-	6634	
	N03'230B	CKR-N03'	11.5	shell	II	3282	±23	3332	-	2928	
	N03'260A	CKR-N03'	11.2	shell	II	3942	±25	4158	-	3725	
	N03'280	CKR-N03'	11.0	shell	II	3891	±26	4097	-	3669	
	N03'404B	CKR-N03'	9.8	shell	II	5785	±25	6321	-	5951	
	N03'528	CKR-N03'	8.6	shell	II	5623	±26	6185	-	5787	
	N04145A	CKR-N04	7.7	shell	III	5871	±25	6432	-	6051	
	N04205	CKR-N04	7.1	shell	III	2662	±29	2615	-	2158	
	N04270	CKR-N04	6.4	shell	III	5771	±27	6304	-	5939	
	N04450A	CKR-N04	4.6	shell	III	5867	±35	6431	-	6035	
	N04540A	CKR-N04	3.7	shell	III	6043	±32	6630	-	6255	
	N05200A	CKR-N05	6.5	shell	III	5355	±30	5889	-	5515	
	N05200B	CKR-N05	6.5	shell	III	5992	±30	6565	-	6193	
	N05290	CKR-N05	5.6	shell	III	5739	±26	6279	-	5922	
	N05345G	CKR-N05	5.1	shell	III	5628	±26	6190	-	5793	
	N05430	CKR-N05	4.2	shell	III	5897	±27	6469	-	6091	
	N06100A	CKR-N06	2.9	shell	IV	3339	±24	3384	-	2991	
	N06210	CKR-N06	1.7	shell	IV	1630	±30	1330	-	994	This study
	N06335	CKR-N06	0.6	shell	IV	8349	±30	9123	-	8653	Komori et al.
	N06385	CKR-N06	0.0	shell	IV	9029	±38	10007	-	9519	(2017)
	N06560A	CKR-N06	-1.7	shell	IV	8666	±32	9487	-	9106	
	S01427A	CKR-S01	17.2	shell	I	5497	±29	6034	-	5629	
	S01510A	CKR-S01	16.4	shell	I	5576	±29	6148	-	5733	
	S01550A	CKR-S01	16.0	shell	I	5543	±27	6107	-	5693	
	S02170A	CKR-S02	15.0	shell	II	5296	±32	5840	-	5450	
	S02170C	CKR-S02	15.0	shell	II	5467	±31	5987	-	5606	
	S02355A	CKR-S02	13.1	shell	II	5727	±27	6271	-	5916	
	S02420A	CKR-S02	12.5	shell	II	5934	±26	6497	-	6130	
	S03030A	CKR-S03	15.4	shell	II	5151	±24	5641	-	5295	
	S03080A	CKR-S03	14.9	shell	II	4221	±35	4532	-	4089	
	S03095	CKR-S03	14.8	shell	II	3918	±25	4134	-	3705	
	S03135	CKR-S03	14.4	shell	II	3965	±28	4210	-	3770	
	S03'145B	CKR-S03'	14.3	shell	II	4173	±27	4484	-	4046	
	S03'225A	CKR-S03'	13.5	shell	II	5403	±28	5919	-	5566	
	S03'395B	CKR-S03'	11.8	shell	II	5957	±25	6530	-	6167	
	S04"175A	CKR-S04"	8.6	shell	III	6485	±26	7142	-	6735	
	S04"180A	CKR-S04"	8.6	shell	III	6228	±28	6834	-	6429	
	S04"185A	CKR-S04"	8.5	shell	III	6210	±25	6800	-	6404	

	S04"222B	CKR-S04"	8.1	shell	III	6330	±30	6952	-	6543	
	S05313A	CKR-S05	6.9	shell	III	7110	±30	7713	-	7390	
	S05340B	CKR-S05	6.6	shell	III	6978	±31	7581	-	7261	
	S05515	CKR-S05	4.9	shell	III	7553	±32	8168	-	7808	
	S06278	CKR-S06	1.1	shell	IV	1640	±30	1340	-	1003	This study
	S06340A	CKR-S06	0.5	shell	IV	8363	±40	9155	-	8651	Komori et al. (2017)
	M01153	CKR-M01	14.0	shell	II	5139	±27	5631	-	5285	This study
	M04155	CKR-M04	5.0	shell	III	2568	±22	2455	-	2049	
	STH01085A	STH01	3.8	shell	IV	8509	±38	9366	-	8926	
	STH01085B	STH01	3.8	shell	IV	777	±40	535	-	203	
	STH01150	STH01	3.1	shell	IV	8220	±30	8971	-	8531	
	STH02090	STH02	3.5	shell	IV	9594	±42	10721	-	10247	
	STH02120	STH02	3.2	shell	IV	2410	±23	2281	-	1871	
	STH03155A	STH03	2.8	shell	IV	695	±43	485	-	111	
	STH03155B	STH03	2.8	shell	IV	548	±30	299	-	modern	
	STH04080	STH04	3.5	shell	IV	769	±32	524	-	203	
	Beta-211441	C-Loc. 02	22.5	peat	I	650	±40	670	-	553	Uno et al. (2007)
	Beta-206399	C-Loc. 07	13.3	shell	II	4470	±40	4839	-	4423	
	Beta-210276	C-Loc. 08	13.9	shell	II	4770	±40	5262	-	4826	
	Beta-216401	C-Loc. 09	8.2	shell	III	3910	±40	4140	-	3684	
	Beta-211442	C-Loc. 11	7.5	shell	III	3850	±40	4066	-	3607	
Tateyama	TY0101	TY01	11.3	seeds	II	70	±40	267	(26.7)	215	Shishikura et al. (2005)
								148	(68.8)	21	
	TY0102	TY01	8.9	wood	II	3320	±50	3690	(5.1)	3660	
								3647	(90.0)	3447	
								3419	(0.3)	3415	
	TY0103	TY01	8.7	wood	II	3360	±40	3693	-	3482	
	TY0201	TY02	11.7	soil	II	1490	±40	1510	(1.7)	1496	
								1472	(2.6)	1454	
								1417	(91.1)	1300	
	TY0202	TY02	9.7	wood	II	3250	±40	3562	-	3387	
	TY0203	TY02	9.3	wood	II	3420	±40	3827	(10.5)	3790	
								3774	(5.6)	3741	
								3731	(79.4)	3565	
	TY0204	TY02	8.5	leef	II	3430	±40	3828	(13.7)	3788	
								3775	(81.8)	3571	
	TY0205	TY02	8.5	shell	II	3850	±40	4066	-	3607	
	TY0206	TY02	8.2	shell	II	3740	±40	3899	-	3462	
	SN0101	SN01	16.8	plant	I	5080	±40	5918	-	5730	This study
	SN0102	SN01	15.6	shell	I	6280	±40	6906	-	6476	
	SN0201	SN02	16.0	plant	I	5640	±40	6495	-	6310	
	SN0202	SN02	14.6	shell	I	5730	±40	6280	-	5907	
	KB0101	KB01	13.4	plant	II	3500	±30	3868	(0.8)	3861	
								3851	(93.6)	3691	
								3658	(1.0)	3650	
	KB0102	KB01	11.3	shell	II	4300	±30	4655	-	4195	
	KB0201	KB02	11.4	plant	II	7450	±40	8357	-	8184	
	KB0202	KB02	10.2	shell	II	4070	±30	4351	-	3902	
	TK0101	TK01	5.3	plant	III	2570	±30	2757	(73.0)	2698	
								2635	(6.9)	2615	
								2588	(15.6)	2518	
	TK0102	TK01	4.4	shell	III	3700	±30	3840	-	3435	
	TK0201	TK02	3.2	shell	III	3420	±30	3480	-	3088	
	TK0202	TK02	0.2	shell	III	4080	±30	4365	-	3915	
	PLD-26263	TYM-3	5.5	leaf	III	3210	±20	3457	-	3383	Shishikura et al. (2014a)
	PLD-26264	TYM-4	5.3	wood	III	3300	±20	3565	-	3463	
	PLD-26265	TYM-5	5.2	leaf	III	2195	±20	2310	(56.6)	2221	

97

								2216	(7.2)	2191	
								2185	(31.7)	2123	
	PLD-26266	TYM-6	1.4	wood	IV	1085	±20	1058	(32.8)	1021	
								1007	(62.6)	932	
	PLD-26267	TYM-6	-2.3	seaurchin	IV	7905	±25	8525	-	8175	
	Beta-374985	TYM-7	0.7	shell	IV	1690	±30	1391	-	1056	
	JNC5668	GS1	-0.1	shell	IV	878	±110	698	-	205	Fujiwara
	JNC6318	GS1	-0.3	shell	IV	1008	±33	714	-	438	et al. (2006)
	JNC6320	GS1	-2.0	shell	IV	1612	±34	1308	-	968	
	JNC6322	GS1	-2.3	shell	IV	1968	±32	1707	-	1342	
	NG0101	GS1	-0.7	NR**	IV	NR		880	***	680	Fujiwara
	NG0102	GS1	-0.8	NR	IV	NR		660	***	530	et al. (2010)
	NG0103	GS1	-1.1	NR	IV	NR		1100	***	910	
	NG0104	GS1	-1.3	NR	IV	NR		980	***	780	
	NG0105	GS1	-1.5	NR	IV	NR		8010	***	7830	
	JNC5664	GS2	0.3	shell	IV	723	±78	523	-	92	Fujiwara
	JNC5665	GS2	1.0	shell	IV	222	±76	180	-	modern	et al. (2006)
	JNC5666	GS2	-0.1	shell	IV	1212	±79	960	-	545	
	JNC5667	GS2	-1.3	shell	IV	7219	±109	7925	-	7413	
	NG0201	GS2	-0.1	NR	IV	NR		680	***	550	Fujiwara
	NG0202	GS2	-0.4	NR	IV	NR		900	***	715	et al. (2010)
	NG0203	GS2	-0.8	NR	IV	NR		900	***	720	
	NG0204	GS2	-0.9	NR	IV	NR		950	***	770	
	NG0205	GS2	-1.4	NR	IV	NR		1060	***	890	
	TB3C-8	TB3	1.3	shell	III	3835	±50	4057	-	3574	Fujiwara
	TB3C-7	TB3	1.2	shell	III	3875	±50	4103	-	3619	et al. (1999)
	TB3C-6	TB3	0.3	shell	III	5205	±50	5726	-	5315	
	TB3C-5	TB3	-0.7	shell	III	4955	±55	5476	-	4987	
	TB3C-4	TB3	-1.4	shell	III	6405	±55	7080	-	6608	
	TB3C-3	TB3	-2.8	shell	III	7755	±60	8384	-	7984	
	TB3C-2	TB3	-3.9	shell	III	8185	±65	8967	-	8443	
	TB3C-1	TB3	-4.0	shell	III	8215	±70	8994	-	8461	
	TB4C-13	TB4	1.1	shell	III	2110	±45	1908	-	1486	
	TB4C-12	TB4	0.4	shell	III	2460	±45	2330	-	1908	
	TB4C-11	TB4	-0.6	shell	III	3630	±50	3790	-	3343	
	TB4C-10	TB4	-1.0	shell	III	4075	±50	4380	-	3891	
	TB4C-9	TB4	-1.7	shell	III	3320	±50	3387	-	2941	
	TB4C-8	TB4	-2.7	shell	III	3715	±50	3886	-	3432	
	TB4C-7	TB4	-3.1	shell	III	4025	±50	4314	-	3822	
	TB4C-6	TB4	-4.0	shell	III	4935	±55	5460	-	4970	
	TB4C-5	TB4	-4.3	shell	III	5500	±55	6070	-	5610	
	TB4C-4	TB4	-4.8	shell	III	6120	±55	6726	-	6296	
	TB4C-3	TB4	-5.3	shell	III	7930	±120	8738	-	8044	
	TB4C-2	TB4	-6.0	shell	III	8220	±60	8991	-	8489	
	TB4C-1	TB4	-6.6	shell	III	8405	±70	9272	-	8687	
	TB6C-10	TB6	0.4	shell	III	4440	±50	4830	-	4390	
	TB6C-9	TB6	-0.3	shell	III	4205	±60	4561	-	4041	
	TB6C-8	TB6	-0.8	shell	III	3440	±50	3541	-	3097	
	TB6C-7	TB6	-2.3	shell	III	4580	±55	5025	-	4525	
	TB6C-6	TB6	-3.3	shell	III	5410	±55	5960	-	5547	
	TB6C-5	TB6	-4.4	shell	III	5790	±55	6361	-	5936	
	TB6C-4	TB6	-5.5	shell	III	6675	±60	7345	-	6900	
	TB6C-3	TB6	-6.8	shell	III	8230	±65	9004	-	8486	
	TB6C-2	TB6	-7.2	shell	III	8375	±70	9231	-	8641	
	TB6C-1	TB6	-7.8	shell	III	8380	±95	9272	-	8608	
Koyatsu	Beta-374979	KYT-1	4.3	shell	III	2520	±30	2376	-	1981	Shishikura
	PLD-26252	KYT-1	3.7	seaurchin	III	4055	±20	4324	-	3886	et al. (2014a)

	PLD-26253	KYT-1	2.9	wood	III	3800	±20	4245	(80.7)	4142	
								4127	(14.8)	4092	
	PLD-26254	KYT-2	4.3	wood	III	3835	±20	4389	(1.3)	4374	
								4354	(5.6)	4327	
								4299	(88.6)	4150	
	Beta-374980	KYT-2	3.8	plant	III	3570	±30	3972	(8.5)	3942	
								3932	(76.7)	3824	
								3793	(6.5)	3770	
								3746	(3.7)	3727	
	Beta-374981	KYT-2	3.2	wood	III	3620	±30	4072	(5.6)	4044	
								3989	(89.8)	3840	
	PLD-26255	KYT-3	4.6	wood	III	3085	±20	3365	-	3234	
	PLD-26256	KYT-4	3.7	shell	III	3705	±25	3841	-	3442	
	PLD-26251	KYT-5	4.6	shell	III	3555	±20	3648	-	3264	
	Beta-374982	KYT-5	4.4	shell	III	3620	±30	3741	-	3344	
	PLD-26257	KYT-7	5.2	plant	III	1155	±20	1178	(9.8)	1162	
								1124	(43.8)	1047	
								1036	(41.8)	975	
	Beta-374983	KYT-8	5.2	shell	III	3880	±30	4084	-	3648	
	PLD-26258	KYT-9	6.6	plant	III	4790	±20	5586	-	5477	
	Beta-374984	KYT-9	6.2	shell	III	4950	±30	5459	-	5023	
Tomiura	TM0101	TM01	2.5	plant	III	1760	±40	1725	-	1546	Shishikura
	TM0102	TM01	2.2	charcoal	III	2460	±40	2707	(26.4)	2627	et al. (2005)
								2622	(69.1)	2365	
	TM0201	TM02	1.7	wood	III	2520	±40	2745	-	2465	
	TM0202	TM02	0.4	leaf	III	2810	±50	3060	-	2782	
Heisa-ura	SNS06150	HSNS02	18.0	shell	II	3861	±36	4072	-	3625	This study
	SNS08038	HSNS04	16.2	shell	II	6810	±30	7439	-	7089	
	SNS01050	HSNS05	14.1	shell	II	4800	±30	5275	-	4853	
	SNS02045	HSNS05	14.1	shell	II	5350	±30	5885	-	5508	
	SNS10100	HSNS06	12.9	shell	II	4120	±30	4405	-	3971	
	SNS11065	HSNS06	13.3	shell	II	5060	±30	5575	-	5195	
	SNH02100A	HSNS07	12.4	shell	II	5300	±30	5842	-	5455	
	SNH02100B	HSNS07	12.4	shell	II	4610	±30	5037	-	4591	
	SNH01050A	HSNH01	14.7	shell	II	4180	±30	4495	-	4057	
	SNH01050B	HSNH01	14.7	shell	II	3890	±30	4100	-	3661	
	SNS16080	HSNS08	8.1	shell	III	7364	±28	7953	-	7619	
	SNS12060	HSNS09	7.3	shell	III	7471	±25	8060	-	7703	
	SNS13060	HSNS09	7.3	shell	III	8011	±29	8659	-	8286	
	SNS15060	HSNS10	7.0	shell	III	2462	±30	2320	-	1928	
	SNS14070	HSNS11	6.6	shell	III	3663	±26	3803	-	3399	
	SNS15050	HSNS10	7.1	shell	III	3293	±32	3347	-	2934	
	SNS14085	HSNS11	6.5	shell	III	4495	±29	4855	-	4451	
	SNH11020	HSNH02	3.8	shell	IV	7341	±35	7936	-	7596	
	SNH11100	HSNH02	3.0	shell	IV	3588	±45	3720	-	3284	
	SNH12050	HSNH03	3.5	shell	IV	4031	±55	4334	-	3827	
	HSU01120	ALH01	2	shell	IV	4370	±30	4770	-	4310	
	ALH01120	ALH01	2	shell	IV	6114	±47	6710	-	6299	
	ALH01140	ALH01	1.8	shell	IV	892	±23	624	-	319	
	ALH01150	ALH01	1.7	shell	IV	983	±36	698	-	411	
	ALH02080	ALH02	2.3	shell	IV	817	±38	560	-	250	
	ALH02120	ALH02	1.9	shell	IV	644	±36	441	-	56	
	ALH02130	ALH02	1.8	shell	IV	4555	±32	4954	-	4524	
	ALH03110A	ALH03	1.6	shell	IV	10361	±41	11844	-	11291	
	ALH03110B	ALH03	1.6	shell	IV	9440	±32	10518	-	10118	
	ALH03135	ALH03	1.3	shell	IV	8926	±30	9840	-	9426	
	ALH03165	ALH03	1	shell	IV	9122	±32	10130	-	9630	

	HSU03180	HSNH15	1.7	shell	IV	4480	±30	4841	-	4441	
Onjuku	PLD-26259	ONJ-1	2.2	shell		3900	±20	4102	-	3683	Shishikura
	PLD-26260	ONJ-2	2	shell		3970	±20	4213	-	3780	et al. (2014a)
	PLD-26261	ONJ-7	3	plant		1715	±20	1695	(24.1)	1665	
								1625	(71.4)	1542	
	PLD-26262	ONJ-7	1.4	plant		2140	±25	2298	(16.9)	2260	
								2155	(71.9)	2039	
								2029	(6.6)	2002	
Iwai	IW0101	IW01	4.2	shell		2870	±40	2822	-	2399	Shishikura
	IW0201	IW02	10.5	plant		170	±40	294	(18.4)	240	et al. (2005)
								233	(42.6)	128	
								119	(16.4)	57	
								45	(18.1)	modern	
	IW0202	IW02	8.6	shell		6330	±50	6975	-	6522	
	IW0203	IW02	8.5	seeds		5200	±50	6178	(5.2)	6145	
								6117	(13.2)	6042	
								6027	(74.3)	5893	
								5805	(2.8)	5766	
	IW0204	IW02	8.4	shell		6450	±50	7126	-	6670	
	IW0205	IW02	8.1	shell		6530	±40	7179	-	6755	

* parenthetic numbers indicate probability of each interval

** Not reported

*** Calibration curve and parameters are different from this study

Table S-3. Recalibrated dating results for outcrop samples

Region	Sample_name	Sampling_point	River	material	13C uncorrected		14C age			Calibrated age		
Tateyama	I-18315	Loc. 8	Heguri River	shell	7240	140	7630	140	*	8392	-	7733
	GX-20387	Loc. 12		shell	7465	NR	7860	240	*	8972	-	7801
	I-18022	Loc. 12		shell	6290	120	6680	120	*	7424	-	6813
	I-18023	Loc. 12		shell	6150	120	6540	120	*	7294	-	6662
	I-17529	Loc. 12		shell	6430	110	6820	110	*	7548	-	6995
	I-18021	Loc. 17		shell	6010	120	6400	120	*	7159	-	6497
	GX-20380-AMS	Loc. 12		shell	6350	NR	6736	57		7407	-	6986
	I-18024	Loc. 12		shell	5880	120	6270	120	*	7015	-	6349
	GX-20386	Loc. 20		shell	6570	NR	6960	250		7942	-	6868
	I-17988	Loc. 20		shell	4770	110	5160	110	*	5812	-	5176
	GX-20385	Loc. 20		shell	6735	NR	7165	100		7859	-	7360
	I-17980	Loc. 22		shell	4390	110	4780	110	*	5380	-	4706
	GX-20375-AMS	Loc. 22		shell	4840	NR	5242	80		5828	-	5320
	GX-20376	Loc. 22		shell	4700	NR	5100	180		5868	-	4942
	GX-20379	Loc. 22		shell	6620	NR	7010	315		8146	-	6789
	I-17987	Loc. 22		shell	4500	110	4890	110	*	5475	-	4837
	I-17989	Loc. 22		shell	4500	110	4890	110	*	5475	-	4837
	GX-20384-AMS	Loc. 22		shell	4945	NR	5346	58		5895	-	5475
	I-17981	Loc. 22		shell	4420	110	4810	110	*	5430	-	4775
	GX-20377	Loc. 22		shell	5000	NR	5385	250		6309	-	5136
	I-17982	Loc. 22		shell	4450	110	4840	110	*	5442	-	4805
	I-17983	Loc. 22		shell	4390	110	4780	110	*	5380	-	4706
	I-17984	Loc. 22		shell	4430	110	4820	110	*	5434	-	4786
	I-17985	Loc. 22		shell	4490	110	4880	110	*	5467	-	4832
	GX-20378-AMS	Loc. 22		shell	4425	NR	4823	51		5306	-	4851
	I-17986	Loc. 22		shell	4410	110	4800	110	*	5421	-	4759
	I-17530	Loc. 22		shell	4130	110	4520	110	*	5055	-	4354
	I-18316	Loc. 25		shell	4610	120	5000	120	*	5606	-	4926
	I-18317	Loc. 26		shell	4180	110	4570	110	*	5134	-	4415
	I-18318	Loc. 26		shell	4000	100	4390	100	*	4849	-	4217
	I-18319	Loc. 26		shell	4220	110	4610	110	*	5211	-	4486
	I-18337	Loc. 26		shell	4140	110	4530	110	*	5074	-	4368
	I-18338	Loc. 26		shell	3660	100	4050	100	*	4425	-	3762
	I-18339	Loc. 26		shell	3810	100	4200	100	*	4635	-	3954
	I-18340	Loc. 26		shell	3670	100	4060	100	*	4435	-	3773
	GX-21473	TV-6		shell	7390	NR	7785	65		8419	-	7999
	GX-21474	TV-6		shell	6235	NR	6585	60		7255	-	6804
Heisa-ura	I-18025	Loc. 37	Tomoe River	shell	6890	130	7280	130	*	8005	-	7425
	I-18026	Loc. 37		shell	6820	130	7210	130	*	7946	-	7365
	I-18027	Loc. 37		shell	7010	130	7400	130	*	8158	-	7547
	I-18029	Loc. 37		shell	6870	130	7260	130	*	7992	-	7415

|												
	I-18028	Loc. 37		shell	7340	130	7730	130	*	8490	-	7852
	I-18351	Loc. 34		shell	7380	120	7770	120	*	8520	-	7920
	I-18352	Loc. 34		shell	6860	120	7250	120	*	7961	-	7419
	I-18353	Loc. 34		shell	7100	120	7490	120	*	8217	-	7620
	I-18354	Loc. 34		shell	6610	120	7000	120	*	7720	-	7165
	I-18355	Loc. 34		shell	6650	120	7040	120	*	7775	-	7216
	I-18356	Loc. 33		shell	6760	120	7150	120	*	7875	-	7315
Tateyama	GaK5457	Loc. 23	Heguri River	shell	4840	120	5230	120	*	5890	-	5265
	N-3087	Loc. 23		shell	4440	110	4830	110	*	5438	-	4796
	N-3086	Loc. 23		shell	5880	110	6270	110	*	7001	-	6372
	N-3085	Loc. 23		shell	7330	120	7720	120	*	8450	-	7855
	GaK3758	Loc. 23		shell	4490	120	4880	120	*	5487	-	4817
	GaK2969	Loc. 23		coral	6340	140	6730	140	*	7505	-	6834
	GaK2968	Loc. 23		shell	6410	130	6800	130	*	7557	-	6939
	GaK3757	Loc. 23		shell	6600	150	6990	150	*	7784	-	7110
	NHC-12	Loc. 23		shell	5260	60	5680	60		6272	-	5841
	NHC-11	Loc. 23		shell	6310	50	6740	50		7405	-	6996
	NHC-10	Loc. 23		coral	6640	60	7000	60		7630	-	7258
Heisa-ura	NTC-5	Loc. 34	Tomoe River	shell	6420	60	6870	60		7528	-	7140
	NTC-4	Loc. 34		shell	6420	50	6780	50		7425	-	7032
	NTC-2	Loc. 34		shell	7260	60	7700	60		8340	-	7938

* Corrected by artificial δ13C value (pre-AMS samples)

Table S-4. Recalibrated dating results of the dataset by Nakata et al. (1980)

Region	Sample_name	Level	elevation	material	13C uncorrected		Conventional age*		Calibrated age**		
Tateyama	GaK-254	I	19	coral	6160	120	6547	120	7300		6669
	TH-085	I	17	shell	5970	180	6357	180	7227		6360
	TH-086	I	17	coral	6000	180	6387	180	7250		6389
	TH-110	I	17	coral	5365	170	5752	170	6536		5706
Koyatsu	TK-7	I	16	coral	7870	70	8257	70	9056		8508
	N-3088	I	14	shell	7840	110	8227	110	9085		8407
	TH-218	I	8.3	shell	6370	165	6757	165	7569		6815
	TH-219	III	10	coral	4010	135	4397	135	4943		4142
	TH-272	III	11.6	shell	5090	120	5477	120	6166		5531
Heisa-ura	GaK-5459	IV	2.8	shell	820	80	1207	80	957		542
	TH-109	IV	5.5	shell	2685	130	3072	130	3256		2501
	GaK-2995	IV	6	shell	2440	100	2827	100	2870		2284
	GaK-5458	I	10.5	shell	7690	190	8077	190	9108		8108
	TH-215	I	14.8	shell	6280	165	6667	165	7486		6721
	TH-216	II	13.9	shell	5440	155	5827	155	6605		5834
	TH-217	II	18.7	shell	4760	140	5147	140	5846		5084
Shirahama	TH-284	III	10.3	shell	3360	100	3747	100	4020		3385
Chikura	TH-278	II	12.5	shell	5510	130	5897	130	6612		5938
	TH-279	II	13.6	shell	4560	115	4947	115	5554		4890
	GaK-3068	II	15	shell	3610	120	3997	120	4406		3660
	GaK-3070	III	10	shell	2860	100	3247	100	3371		2778
	TH-107	II	15.3	shell	5325	170	5712	170	6479		5658
	TH-108	III	10	shell	4315	145	4702	145	5340		4514
	TH-280	II	10.7	shell	4920	120	5307	120	5940		5316
	TH-281	I	5.1	shell	6430	140	6817	140	7580		6930
	GaK-5374	II	18	shell	4740	100	5127	100	5733		5139
	TH-214	II	18.9	shell	4280	130	4667	130	5287		4519
	N-2565	II	12	shell	4640	90	5027	90	5591		5029
	N-2566	I	10	shell	7810	110	8197	110	9039		8376
	TH-273	I	4.5	shell	7450	155	7837	155	8705		7915
	TH-274	I	5.4	shell	7340	150	7727	150	8536		7816
	TH-275	I	7.5	shell	7290	150	7677	150	8470		7756
	TH-276	II	16.9	shell	3230	105	3617	105	3867		3226
	TH-277	I	23	shell	6530	140	6917	140	7675		7035
	TH-282	I	23.5	peat	6200	135	6587	135	7689	(94.3)	7251
									7201	(1.2)	7173
	TH-106	I	22.5	shell	6910	200	7297	200	8176		7327

* Corrected by artificial δ13C value

** parenthetic numbers indicate probability of each interval
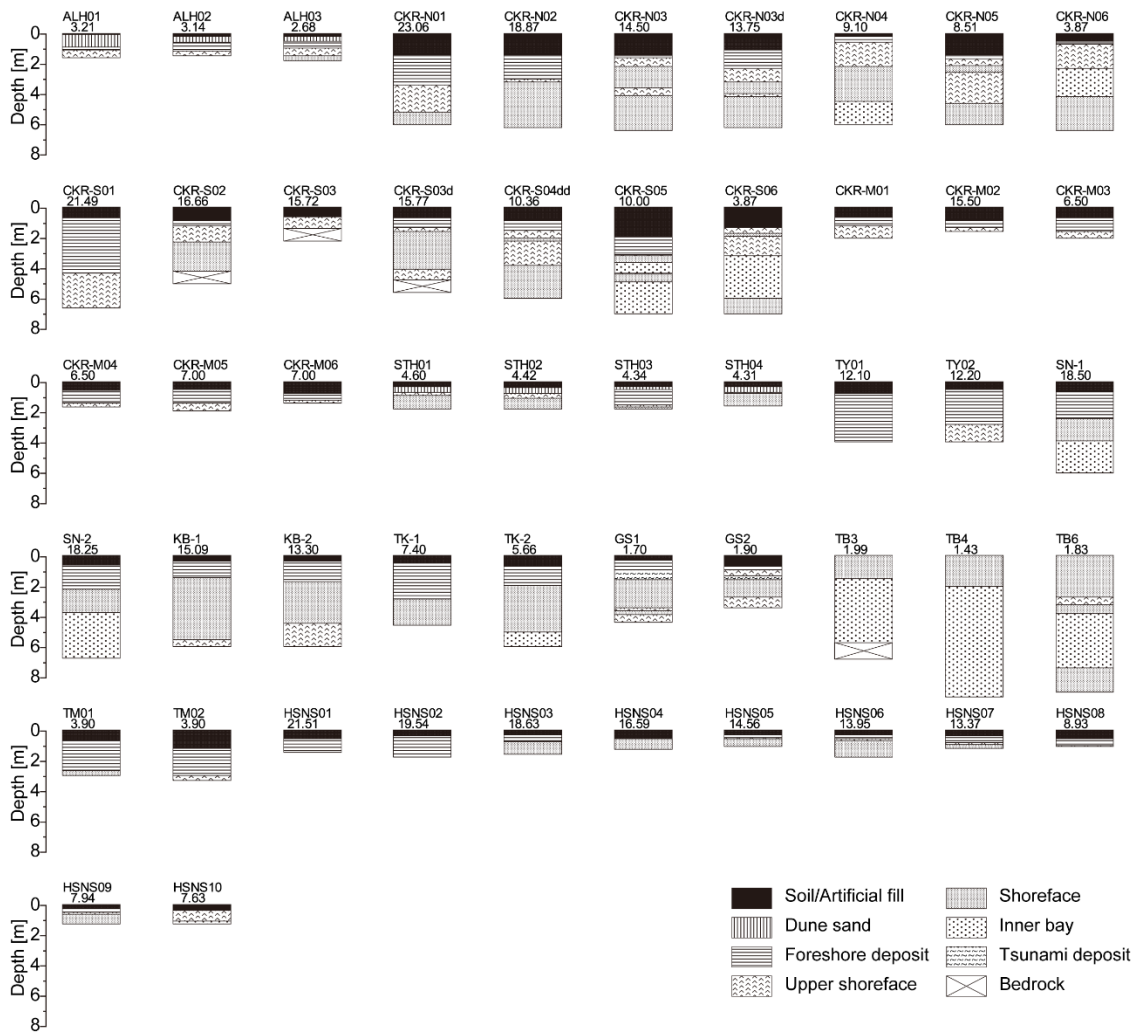
Figure S-1. Columnar sections of the sediment samples in this study and the previous investigations. The sedimentary layer classification is based on Komori et al. (2017). The number above each columnar section is the surface elevation of the sampling point (meter a.s.l.). The numbers displayed next to each columnar section indicate the dating results (yBP). Refer to Table S-1 for detailed information about each sampling point.

References

Aida, I. (1993). Historical tsunamis and their numerical models which occurred in the north-western part of Sagami Bay, *Journal of Geography (Chigaku zasshi)*, **102**, 427-436, (in Japanese with English abstract and figure captions). https://doi.org/10.5026/jgeography.102.4_427

Amante C., Eakins, B.W. (2009). ETOPO1 1 arc-minute global relief model: Procedures, data sources and analysis. NOAA Technical Memorandum NESDIS NGDC-24. http://doi:10.7289/V5C8276M

Anderson, R.S., Menking, K.M. (1994). The Quaternary marine terraces of Santa Cruz, California: Evidence for coseismic uplift on two faults. *Geological Society of America Bulletin*, **106**, 649–664. https://doi.org/10.1130/0016-7606(1994)106<0649:TQMTOS>2.3.CO;2

Ando, M. (1971). A fault-origin model of the Great Kanto earthquake of 1923 as deduced from geodetic data, *Bulletin of Earthquake Research Institute, University of Tokyo*, **49**, 19– 32. http://hdl.handle.net/2261/12576

Ando, M. (1974), Seismo-tectonics of the 1923 Kanto earthquake, *Journal of Physics of the Earth*, **22**, 263– 277. https://doi.org/10.4294/jpe1952.22.263

Atwater, B.F., Furukawa, R., Hemphill-Haley, E., Ikeda, Y., Kashima, K., Kawase, K., et al. (2004). Seventeenth-century uplift in eastern Hokkaido, Japan. *Holocene*, **14**, 487–501. https://doi.org/10.1191/0959683604hl726rp

Berryman, K. (1993), Age, height, and deformation of Holocene marine terraces at Mahia Peninsula, Hikurangi Subduction Margin, New Zealand, *Tectonics*, **12**, 1347–1364, doi:10.1029/93TC01542.

Berryman, K., Clark, K., Cochran, U., Beu, A., Irwin, S. (2018). A geomorphic and tectonic model for the formation of the flight of Holocene marine terraces at Mahia Peninsula, New Zealand. *Geomorphology*, **307**, 77–92. https://doi.org/10.1016/j.geomorph.2017.10.014

Bishop, C.M. (2006). Pattern recognition and machine learning. Springer.

Bowles, C.J., Cowgill, E. (2012). Discovering marine terraces using airborne LiDAR along the Mendocino-Sonoma coast, northern California. *Geosphere*, **8**, 386–402. https://doi.org/10.1130/GES00702.1

Bradley, W.C., Griggs, G.B. (1976). Form, genesis, and deformation of central California wave-cut platforms. *Geological Society of America Bulletin*, **87**, 433–449. https://doi.org/10.1130/0016-7606(1976)87<433:FGADOC>2.0.CO;2

Carver, G., Plafker, G. (2008). Paleoseismicity and neotectonics of the Aleutian Subduction Zone---An overview. *In: Active tectonics and Seismic potential of Alaska, Geophysical Monograph Series 179*, American Geophysical Union, Washington. http://doi.org/10.1029/179GM03

Chappell, J. (1974). Geology of coral terraces, Huon Peninsula, New Guinea: a study of Quaternary tectonic movements and sea-level changes. *Geological Society of America Bulletin*, **85**, 553–570. https://doi.org/10.1016/0025-3227(79)90095-1

Chiba, T., Kaneta, S.-I., Suzuki, Y. (2008). Red relief image map: new visualization method for three dimensional data. The International Archives of the Photogrammetry, *Remote Sensing and Spatial Information Sciences*, **37**, 1071-1076

Chiba, T., Sugihara, S., Matsushima, Y., Arai, Y., Endo, K. (2016). Reconstruction of Holocene relative sea-level change and residual uplift in the Lake Inba area, Japan. *Palaeogeography Palaeoclimatology*, **441**, 982–996. https://doi.org/10.1016/j.palaeo.2015.10.042

Clark, K. J., Nissen, E. K., Howarth, J. D., Hamling I. J., Mountjoy J. J., Ries, W. F., et al., (2017). Highly variable coastal deformation in the 2016 MW7.8 Kaikōura earthquake reflects rupture complexity along a transpressional plate boundary. *Earth and Planetary Science Letters*, **474**, 334–344. https://doi.org/10.1016/j.epsl.2017.06.048

Clark, K., Howarth, J., Litchfield, N., Cochran, U., Turnbull, J., Dowling, L., et al. (2019). Geological evidence for past large earthquakes and tsunamis along the Hikurangi subduction margin, New Zealand. *Marine Geology,* **412**, 139-172. https://doi.org/10.1016/j.margeo.2019.03.004

Cummins, P., R., Kaneda, Y. (2000). Possible splay fault slip during the 1946 Nankai earthquake. *Geophysical Research Letters*, **27**, 2725−2728. https://doi.org/10.1029/1999GL011139

Dasgupta, A., Raftery, A.E. (1998). Detecting features in spatial point processes with clutter via model-based clustering. *Journal of the American Statistical Association,* **93**, 294–302. https://doi.org/10.2307/2669625

DeMets, C. R., Gordon, G., Argus, D. F., Stein, S. (1994). Effect of recent revisions to the geomagnetic reversal time scale on estimates of current plate motions. *Geophysical Research Letters*, **21**, 2191–2194. https://doi.org/10.1029/94GL02118

van Dinther, Y., Preiswerk, L.E., Gerya, T.V. (2019). A secondary zone of uplift due to megathrust earthquakes. Pure and Applied Geophysics. **176**, 4043–4068. https://doi.org/10.1007/s00024-019-02250-z

Dominguez, S., Lallemand, S. E., Malavieille, J., von Huene, R., (1998). Upper plate deformation associated with seamount subduction, *Tectonophysics*, **293**, 207–224. https://doi.org/10.1016/S0040-1951(98)00086-9

Dominguez, S., Malavielle, J., Lallemand, S. E. (2000). Deformation of accretionary wedges in response to seamount subduction- Insights from sandbox experiments, *Tectonics*, **19**, 182–196. https://doi.org/10.1029/1999TC900055

Eymold, W.K., Jordan, T. H. (2019). Tectonic regionalization of the Southern California crust from tomographic cluster analysis. *Journal of Geophysical Research: Solid Earth*, **124**. https://doi.org/10.1029/2019JB018423

Fang, Z., Dunham, M. (2013). Additional shear resistance from fault roughness and stress levels on geometrically complex faults. *Journal of Geophysical Research: Solid Earth*, **118**, 3642–3654. https://doi:10.1002/jgrb.50262

Fujiwara, O., Masuda, F., Sakai, T., Fuse, K., Saito, A. (1997). Tsunami deposits in Holocene bay-floor muds and the uplift history of the Boso and Miura Peninsulas, *The Quaternary Research (Daiyonki-Kenkyu)*, **36**, 73–86 (in Japanese with English abstract), https://doi.org/10.4116/jaqua.36.73

Fujiwara, O., Masuda, F., Sakai, T., Irizuki, T., Fuse, K. (1999). Holocene tsunami deposits detected by drilling in drowned valleys of the Boso and Miura Peninsulas, *The Quaternary Research (Daiyonki-Kenkyu)*, **38**, pp. 41–58 (in Japanese with English abstract and figure captions), https://doi.org/10.4116/jaqua.38.489

Fujiwara, O., Masuda, F., Sakai, T., Irizuki, T., Fuse, K. (2000). Tsunami deposits in Holocene bay mud in southern Kanto region, Pacific coast of central Japan, *Sedimentary Geology*, **135**, 219–230. https://doi.org/10.1016/S0037-0738(00)00073-7

Fujiwara, O., Hirakawa, K., Irizuki, T., Kamataki, T., Uchida, J., Abe, K., et al., (2006). Progradation of Tateyama strand plain system, SW coast of Boso Peninsula, central Japan, triggered by coseismic uplifts during the historical Kanto earthquakes. *The Quaternary Research (Daiyonki-Kenkyu)*, **45**, pp. 235–247, (in Japanese with English abstract and figure captions), https://doi.org/10.4116/jaqua.45.235

Fujiwara, O., Sawai, Y., Fujino, S., Namegaya, Y., Okamura, Y. (2010). Study of subduction zone paleoearthquakes. *Annual report on active fault and paleoearthquake researches*, 11–31 (in Japanese with English abstract and figure captions).

Fujiwara, S., Yarai, H., Kobayashi, T., Morishita, Y., Nakano, T., Miyahara, B., et al. (2016). Small-displacement linear surface ruptures of the 2016 Kumamoto earthquake sequence detected by ALOS-2 SAR interferometry. *Earth, Planets and Space*, **68**, 160. https://doi.org/10.1186/s40623-016-0534-x

Fukahata, Y., Matsu'ura, M. (2016). Deformation of island-arc lithosphere due to steady plate subduction. *Geophysical Journal International*, **204**, 825–840, https://doi: 10.1093/gji/ggv482

Gardner, T., Marshall, J., Merritts, D., Bee, B., Burgette, R., Burton, E., et al. (2001). Holocene forearc block rotation in response to seamount subduction, southeastern Península de Nicoya, Costa Rica, *Geology*, **29**, 151–154. https://doi.org/10.1130/0091-7613(2001)029<0151:HFBRIR>2.0.CO;2

Grant, L.B., Sieh, K. (1994). Paleoseismic evidence of clustered earthquakes on the San Andreas Fault in the Carrizo Plain, California. *Journal of Geophysical Research*, **99**, 6819e6841. https://doi.org/10.1029/94JB00125.

Hashimoto C., Fukui K., Matsu'ura M. (2004). 3-D modelling of plate interfaces and numerical simulation of long-term crustal deformation in and around Japan. *Pure and Applied Geophysics*, **161**, 2053–2068, https://doi.org/10.1007/s00024-004-2548-8

Hatori, T., Aida, I., Kajiura, K. (1973). Tsunamis in the South-Kanto district, *in*

Publications for the 50th Anniversary of the Great Kanto Earthquake, pp. 57–66, Earthquake Research Institute, Tokyo, (in Japanese with English abstract).

Hatori, T. (1975a). Tsunami source off Boso peninsula -estimation of tsunami source area and magnitude of Enpo (1677), Genroku (1703) and 1953 Boso-oki tsunami-. *Bulletin of Earthquake Research Institute, University of Tokyo,* **50**, 83–91. (in Japanese with English abstract and figure captions) http://hdl.handle.net/2261/12588

Hatori, T. (1975b). Sources of large tsunamis generated in the Boso, Tokai and Nankai regions in 1498 and 1605, *Bulletin of Earthquake Research Institute, University of Tokyo*, **50**, 171-185. (in Japanese with English abstract and figure captions). http://hdl.handle.net/2261/12593

Hatori, T. (1975c). Monuments of the tsunami of 1703 and 1923 in the South-Kanto district, *Bulletin of Earthquake Research Institute, University of Tokyo*, **50**, 385-395, (in Japanese with English abstract and figure captions). http://hdl.handle.net/2261/12603

Hatori, T. (1976). Monuments of the 1703 Genroku tsunami along the south Boso Peninsula: wave height of the 1703 tsunami and its comparison with the 1923 Kanto tsunami, *Bulletin of Earthquake Research Institute, University of Tokyo*, **51**, 63-81, (in Japanese with English abstract and figure captions). http://hdl.handle.net/2261/12610

Headquarters for Earthquake Research Promotion. (2004). Long term evaluation of seismic activities along the Sagami Trough, p. 57, (in Japanese).

Heaton, T., Köhler, P., Butzin, M., Bard, E., Reimer, R., Austin, W., Bronk Ramsey, C., Grootes, P., Hughen, K., Kromer, B., Reimer, P., Adkins, J., Burke, A., Cook, M., Olsen, J., & Skinner, L. (2020). Marine20 - the marine radiocarbon age calibration curve (0–55,000 cal BP). *Radiocarbon*, **62**. https://doi.org/10.1017/RDC.2020.68

Herman, M. W., Furlong, K. P., Govers, R. (2018). The Accumulation of Slip Deficit in Subduction Zones in the Absence of Mechanical Coupling: Implications for the Behavior of Megathrust Earthquakes. *Journal of Geophysical Research: Solid Earth*, **123**, 8260–8278. https://doi.org/10.1029/2018JB016336

Herman, M. W., & Govers, R. (2020). Locating fully locked asperities along the South America subduction megathrust: A new physical interseismic inversion approach in a Bayesian framework. *Geochemistry, Geophysics, Geosystems*, **21**, e2020GC009063. https://doi.org/10.1029/2020GC009063

Hirabayashi, S., Yokoyama, Y., Suzuki, A., Miyairi, Y., Aze, T. (2017). Short-term fluctuations in regional radiocarbon reservoir age recorded in coral skeletons from the Ryukyu Islands in the north-western Pacific, *Journal of Quaternary Science*, **32**, 1–6. https://doi.org/10.1002/jqs.2923

Hirose, F., Nakajima, J., Hasegawa, A. (2008) Three-dimensional velocity structure and configuration of the Philippine Sea slab beneath Kanto District, central Japan, estimated by double-difference tomography: *Zisin*, **60**, p. 128–138, https://doi.org/10.4294/zisin.60.123 (in Japanese with English abstract).

Hori, T., Miyazaki, S. (2011). A possible mechanism of M 9 earthquake generation

cycles in the area of repeating M 7~8 earthquakes surrounded by aseismic sliding. *Earth, Planets, and Space*, **63**, 48. https://doi.org/10.5047/eps.2011.06.022

Imamura, A. (1925). The great Kwanto (S.E. Japan) earthquake on September 1, 1923, *in Reports of the Imperial Earthquake Investigation committee*, No. 100A, 21-66, Tokyo. (in Japanese)

Imamura, A. (1925). Change of the coast-line in Boso Peninsula, *in Reports of the Imperial Earthquake Investigation Committee*, No. 100B, 91-93, Tokyo. (in Japanese)

Imamura, A., Hasegawa, K. (1928). List of the after-shocks of the great Kwanto earthquake, *Bulletin of the Imperial Earthquake Investigation Committee*, **11**, 64–92.

Imamura, A. (1930). Fault Systems in Relation to the Multiple Sources of the Kwanto Earthquake. *Geographical Review of Japan*, **6**, 599–610. (in Japanese). https://doi.org/10.4157/grj.6.599

Ishibashi, K. (1977). Source region of the 1703 Genroku Kanto Earthquake and recurrence time of major earthquakes in Sagami Bay, Japan (1), *Zishin 2*, **30**, 369-374, (in Japanese with English figure captions). https://doi.org/10.4294/zisin1948.30.3_369

Ishibashi, K. (2020). Ancient and Medieval Events and Recurrence Interval of Great Kanto Earthquakes along the Sagami Trough, Central Japan, as Inferred from Historiographical Seismology, *Seismological Research Letters*, **91**, 2579–2589, https://doi.org/10.1785/0220200073.

Ishida, M., (1992). Geometry and Relative Motion of the Philippine Sea Plate and Pacific Plate Beneath the Kanto-Tokai District, Japan, *Journal of Geophysical Research*, **97**, 489–513, https://doi.org/10.1029/91JB02567

Ishida, D., Hirota, M., Yoneda, M., Shibata, Y., Morita, M., Endo, K. (2002). Ages of the Holocene former shoreline deduced from emerged erosional landforms along the southern coast of the Boso Peninsula, Central Japan. *In: Annual Report of NIES-TERRA*, pp. 75–80.

Ito, A., Tonegawa, T., Uchida, N., Yamamoto, Y., Suetsugu, D., Hino, R., et al. (2019). Configuration and structure of the Philippine Sea Plate off Boso, Japan: constraints on the shallow subduction kinematics, seismicity, and slow slip events, *Earth Planets Space,* **71**, 111. https://doi.org/10.1186/s40623-019-1090-y

JAMSTEC (2012). KAIREI KR09-07 Cruise Data. JAMSTEC. https://doi.org/10.17596/0001110 (accessed 2020-12-21)

Johnson, K. M., Segall, P. (2004). Viscoelastic earthquake cycle models with deep stress-driven creep along the San Andreas fault system. *Journal of Geophysical Research*, **109**, B10403, https://doi:10.1029/2004JB003096

Kanamori, H., Miyamura, S. (1970). Seismometrical Re-Evaluation of the Great Kanto, Earthquake of September 1, 1923, *Bulletin of Earthquake Research Institute, University of Tokyo*. **48**, 115-125. http://hdl.handle.net/2261/12506

Kanamori, H. (1971). Faulting of the great Kanto earthquake of 1923 as revealed by seismological data, *Bulletin of Earthquake Research Institute, University of Tokyo*.

49, 13-18. http://hdl.handle.net/2261/12575

Kanda, R. V. S., Simons, M. (2010). An elastic plate model for interseismic deformation in subduction zones, *Journal of Geophysical Research*, **115**, B03405, doi:10.1029/2009JB006611

Kanda, R. V. S., Simons, M. (2012). Practical implications of the geometrical sensitivity of elastic dislocation models for field geologic surveys, *Tectonophysics*, **560–561**, 94–104. https://doi.org/10.1016/j.tecto.2012.06.040

Kasahara, K., Yamada, J., Ando, M. (1973). Crustal movements in the South Kanto district, and a related working hypothesis, *in Publications for the 50th anniversary of the great Kanto earthquake*, pp. 103-116, Earthquake Research Institute, Tokyo, (in Japanese with English abstract and figure captions).

Kawakami, S., Shishikura, M. (2006). Geological Map 1:50,000. Tateyama, Geological Survey of Japan, (in Japanese with English abstract).

Kayanne, H., Yoshikawa, T. (1986). Comparative study between present and emergent erosional landforms on the southeast coast of Boso Peninsula, central Japan. *Geographical review of Japan, Series A*, **59**, 18-36. (in Japanese with English abstract and figure captions).

Keller, E.A., Pinter, N. (2002). Active tectonics: earthquakes, uplift, and landscape. Prentice-Hall, Upper Saddle River.

Kimura, H., Takeda, T., Obara, K., Kasahara, K. (2010). Seismic Evidence for Active Underplating Below the Megathrust Earthquake Zone in Japan, *Science*, **329**, 210–212, DOI: 10.1126/science.1187115

Kobayashi, R., Koketsu, K. (2005). Source process of the 1923 Kanto earthquake inferred from historical geodetic, teleseismic, and strong motion data, *Earth, Planets, and Space*, **57**, 261– 270. https://doi.org/10.1186/BF03352562

Kodama, K., Oka, S., Mitsunashi, T. (1980). Geological Map 1:50,000. Misaki, *Geological Survey of Japan*, (in Japanese with English abstract).

Kumaki, Y. (1985). The deformations of Holocene marine terraces in southern Kanto, central Japan, *Geographical Review of Japan, Series B*, **58**, 49–60. https://doi.org/10.4157/grj1984b.58.49

Komori, J., Shishikura, M., Ando, R., Yokoyama, Y., Miyairi, Y. (2017). History of the great Kanto earthquakes inferred from the ages of Holocene marine terraces revealed by a comprehensive drilling survey. *Earth and Planetary Science Letters*, **471**, 74–84. https://doi.org/10.1016/j.epsl.2017.04.044

Lajoie, K.R. (1986). Coastal tectonics. Active tectonics 95–124. https://doi.org/10.1130/0091-7613(1989)017<1020:IQURAT>2.3.CO;2

Land Survey Department (1926). The change of elevation of land caused by the great earthquake of September 1st, 1923. *Bulletin of Earthquake Research Institute, University of Tokyo*, **1**, 65–68. (in Japanese with English abstract) http://hdl.handle.net/2261/9856

Land Survey Department (1930). Re-survey of the Kwanto district after the great earthquake of 1923, *Bulletin of the Imperial Earthquake Investigation Committee*, **11**, 1–6.

Litchfield N. J., Clark, K. J., Cochran, U. A., Palmer, A. S., Mountjoy, J., Mueller, C., et al., (2020). Marine terraces reveal complex near-shore upper-plate faulting in the northern Hikurangi margin, New Zealand. *Bulletin of the Seismological Society of America*, **110**, 825–849, https://doi.org/10.1785/0120190208

Lloyd, S. (1982). Least squares quantization in PCM. *IEEE Transactions on Information Theory*, **28**, 129–137. https://doi.org/10.1109/TIT.1982.1056489

Maemoku, H. (2001). Reexamination of coseismic uplift of Cape Muroto, Southwestern Japan, using AMS14C ages of raised sessile organisms. *Journal of Geography (Chigaku Zasshi),* **110**, 479–490. https://doi.org/10.5026/jgeography.110.4_479

Małoszewski, P., Rauert, R., Stichler, W., Herrmann, A. (1983). Application of flow models in an alpine catchment area using tritium and deuterium data, *Journal of Hydrology*, **66**, 319–330. https://doi.org/10.1016/0022-1694(83)90193-2

Mannen, K., Yoong, K. H., Suzuki, S., Matsushima, Y., Ota, Y., Kain, C. L., Goff, J. (2018). History of ancient megathrust earthquakes beneath metropolitan Tokyo inferred from coastal lowland deposits, *Sedimentary Geology*, **364**, 258–275. https://doi.org/10.1016/j.sedgeo.2017.11.014

Maruyama, T. (1964). Statical Elastic Dislocations in an Infinite and Semi-Infinite Medium, *Bulletin of Earthquake Research Institute, University of Tokyo*, **42**, 289–368. http://hdl.handle.net/2261/12159

Matsuda, T., Ota, Y., Ando, M., Yonekura, N. (1974). Geological study for the 1703 Genroku Earthquake. *In Earthquakes and crustal deformation in the Kanto district*, pp. 175-192, Lattice, Tokyo. (in Japanese).

Matsuda, T., Ota, Y., Ando, M., Yonekura, N. (1978). Fault mechanism and recurrence time of major earthquakes in southern Kanto district, Japan, as deduced from coastal terrace data. *Geological Society of America Bulletin*, **89**, 1610-1618. https://doi.org/10.1130/0016-7606(1978)89%3C1610:FMARTO%3E2.0.CO;2

Matsuda, T., Mizumoto, T., Tajikara, M., Matsuura, R., S. (2014). Was the Oiso coast uplifted in time of the 1703 Genroku earthquake? —Discussion on the marine terrace—, *Zishin 2*, **67**, 35–39. (in Japanese). https://doi.org/10.4294/zisin.67.35

Matsuda, T., Matsu'ura, R. S., Mizumoto, T., Tajikara, M. (2015). Emerged Abrasion Platforms on Enoshima Island, Kanagawa Prefecture and Uplift Associated with the 1703 Genroku Kanto Earthquake, *Journal of Geography (Chigaku Zasshi)*, **124**, 657–664. (in Japanese with English abstract). http://doi:10.5026/jgeography.124.657

Matsu'ura, M., Iwasaki T., Suzuki, Y., Sato R. (1980). Statical and dynamical study on faulting mechanism of the 1923 Kanto earthquake, *Journal of the Physics of the Earth*, **28**, 119–143. https://doi.org/10.4294/jpe1952.28.119

Matsu'ura, M., Iwasaki T. (1983). Study on coseismic and postseismic crustal movements associated with the 1923 Kanto earthquake, *Tectonophysics*, **97**, 201–215. https://doi.org/10.1016/0040-1951(83)90148-8

Matsu'ura, M, Sato, T. (1989). A dislocation model for the earthquake cycle at convergent plate boundaries. Geophysical Journal International, **96**, 23–32, https://doi.org/10.1111/j.1365-246X.1989.tb05247.x

Matsu'ura, M., Noda, A., Fukahata, Y. (2007). Geodetic data inversion based on Bayesian formulation with direct and indirect prior information. *Geophysical Journal International*, **171**:1342–1351, https://doi.org/10.1111/j.1365-246X.2007.03578.x

Matsu'ura, T. (2015). Late Quaternary uplift rate inferred from marine terraces, Muroto Peninsula, southwest Japan: Forearc deformation in an oblique subduction zone. *Geomorphology*, **234**, 133-150. https://doi.org/10.1016/j.geomorph.2015.01.012

McSaveney, M.J., Graham, I.J., Begg, J.G., Beu, A.G., Hull, A.G., Kim, K., Zondervan, A. (2006). Late Holocene uplift of beach ridges at Turakirae Head, south Wellington coast, New Zealand, *New Zealand Journal of Geology and Geophysics*, **49**, 337-358, https://doi:10.1080/00288306.2006.9515172

Meade, B. J. (2007). Algorithms for the calculation of exact displacements, strains, and stresses for triangular dislocation elements in a uniform elastic half space. *Computers and Geosciences,* **33**, 1064-1075, https://doi:10.1016/j.cageo.2006.12.003

Meltzner, A.J., Sieh, K., Chiang, H.-W., Wu, C.-C., Tsang, L.L.H., Shen, C.-C., et al. (2015). Time-varying interseismic strain rates and similar seismic ruptures on the Nias–Simeulue patch of the Sunda megathrust. *Quaternary Science Reviews*, **122**, 258-281. https://doi.org/10.1016/j.quascirev.2015.06.003

Miura, S., Yamashita, M., Fujie, G., No, T., Takahashi, N., Kodaira, S., Kobayashi, R. (2011). Comparison deep structure from marine reflection seismic profiles with seismicity off Boso region, *In: Geological Society of Japan annual meeting 2011*, S3-O-3. https://doi.org/10.14863/geosocabst.2011.0.17.0

Miyabe, N. (1931). On the vertical earth movements in Kwanto districts, *Bulletin of Earthquake Research Institute, the University of Tokyo*, **9**, 1-21. http://hdl.handle.net/2261/9977

Mochizuki, K., Yamada, T., Shinohara, M., Yamanaka, Y., Kanazawa, T. (2008). Weak Interplate Coupling by Seamounts and Repeating M ~ 7 Earthquakes, Science, 321, 1194-1197, https://doi.org/10.1126/science.1160250

Mori, H., Abe, S., Arai, R, Ito, T. (2015). Spatial distribution and activity of faults in the offshore extension of the Kamogawa-teichi fault zone. *Annual Report on Active Fault and Paleoearthquake Researches*, **15**, 109-141, (in Japanese with English abstract and figure captions).

Nakano, S., Nishiki, K., Takarada, S., Hoshizumi, H., Ishizuka, Y., Itoh, J. et al. (2013). Volcanoes of Japan, *In 1: 2,000,000 map series 11, Geological Survey of Japan, AIST.*

Nakata, T., Koba, M., Imaizumi, T., Jo, W., Matsumoto, H. Suganuma, T. (1980). Holocene marine terraces and seismic crustal movements in the southern part of Boso Peninsula, Kanto, Japan. *Geographical Review of Japan, Series A*, **53**, 29-44, (in Japanese with English abstract and figure captions). https://doi.org/10.4157/grj.53.29

Nakata, T., Shimazaki, K. (1997). Geoslicer, a newly invented soil sampler, for high-resolution active fault studies, *Journal of Geography*, **106**, 59–69, (in Japanese with English abstract and figure captions). doi:10.5026/jgeography.106.59

Namegaya, Y., Satake, K., Shishikura, M. (2011). Fault models of the 1703 Genroku and 1923 Taisho Kanto earthquakes inferred from coastal movements in the southern Kanto area. In: *Annual Report on Active Fault and Paleoearthquake Researches*, **11**, 107–120 (in Japanese with English abstract and figure captions).

Nishimura, T., Sagiya, T., Stein, R.S. (2007). Crustal block kinematics and seismic potential of the northernmost Philippine Sea plate and Izu microplate, central Japan, inferred from GPS and leveling data. *Journal of Geophysical Research: Solid Earth,* **112**. https://doi.org/10.1029/2005JB004102

Noda, A., Hashimoto, C., Fukahata, Y., Matsu'ura, M. (2013). Interseismic GPS strain data inversion to estimate slip-deficit rates at plate interfaces: application to the Kanto region, central Japan, *Geophysical Journal International*, **193**, 61–77, https://doi.org/10.1093/gji/ggs129

Noda, A., Miyauchi, T., Sato, T., Matsu'ura, M. (2018). Modelling and simulation of Holocene marine terrace development in Boso Peninsula, central Japan. *Tectonophysics*, **731**, 139–154. https://doi.org/10.1016/j.tecto.2018.03.008

Nyst, M., Pollitz, F. F., Nishimura, T., Thatcher, W. (2006). The 1923 Kanto earthquake reevaluated using a newly augmented geodetic data set, *Journal of Geophysical Research*, **111**, B11306, doi:10.1029/2005JB003628.

Oguchi, T., Aoki, T., Matsuta, N. (2003). Identification of an active fault in the Japanese Alps from DEM-based hill shading. *Computers & Geosciences*, **29**, 885–891. https://doi.org/10.1016/S0098-3004(03)00083-9

Okada, Y. (1985). Surface deformation due to shear and tensile faults in a half space, *Bulletin of Seismological Society of America*, **75**, 1135–1154.

Okada, Y. (1992), Internal deformation due to shear and tensile faults in a half-space, *Bulletin of Seismological Society of America*, **82**, 1018–1040.

Okamura, Y., Shishikura, M. (2020). New hypothesis to explain Quaternary forearc deformation and the variety of plate boundary earthquakes along the Suruga–Nankai Trough by oblique subduction of undulations on the Philippine Sea Plate. *Earth, Planets and Space*, **72**, 55. https://doi.org/10.1186/s40623-020-01183-5

Okuno, J., Nakada, M., Ishii, M., Miura, H. (2014). Vertical tectonic crustal movements along the Japanese coastlines inferred from late Quaternary and recent relative sea-level changes, *Quaternary Science Reviews*, **91**, 42-61. https://doi.org/10.1016/j.quascirev.2014.03.010

Ozawa, S., Hashimoto, M., Tada, T. (1997) Vertical crustal movements in the coastal areas of Japan estimated from tidal observations. *Bulletin of Geographical Survey Institute*, **43**,1-21. http://doi.org/10.11501/10290986

Park, J., Tsuru, T., Kaneda, Y., Kono, Y., Kodaira, S., Takahashi, N., Kinoshita, H. (1999). A subducting seamount beneath the Nankai Accretionary Prism off Shikoku,

southwestern Japan, *Geophysical Research Letters*, **26**, 931-934. https://doi.org/10.1029/1999GL900134

Park, J., Tsuru, T., Kodaira, S., Nakanishi, A., Miura, S., Kaneda, Y., Kono, Y. (2000). Out-of-sequence thrust faults developed in the coseismic slip zone of the 1946 Nankai earthquake (Mw=8.2) off Shikoku, southwest Japan. *Geophysical Research Letters*, **27**, 1033-1036, https://doi.org/10.1029/1999GL008443

Perol, T., Gharbi, M., Denolle, M. (2018). Convolutional neural network for earthquake detection and location. *Science Advances*, **4**, e1700578. DOI: 10.1126/sciadv.1700578

Philibosian, B., Sieh, K., Avouac, J.-P., Natawidjaja, D.H., Chiang, H.-W., Wu, C.-C., et al., (2017). Earthquake supercycles on the Mentawai segment of the Sunda megathrust in the seventeenth century and earlier. *Jounal of Geophysical Research: Solid Earth,* **122**, 642–676. https://doi.org/10.1002/2016JB013560.

Philibosian, B., Meltzner, A. J. (2020). Segmentation and supercycles: A catalog of earthquake rupture patterns from the Sumatran Sunda Megathrust and other well-studied faults worldwide. *Quaternary Science Reviews*, **241**, 106390. https://doi.org/10.1016/j.quascirev.2020.106390

Pirazzoli, P.A., Radtke, U., Hantoro, W.S., Jouannic, C., Hoang, C.T., Causse, C., Best, M.B. (1993). A one million-year-long sequence of marine terraces on Sumba Island, Indonesia. *Marine Geology*, **109**, 221–236. https://doi.org/10.1016/0025-3227(93)90062-Z

Plafker, G. (1969), Tectonics of the March 17, 1964 Alaska Earthquake, *US Geological Survey Professional Paper*, 543 I, 74.

Plafker, G. (1972). Alaskan earthquake of 1964 and Chilean earthquake of 1960—implications for arc tectonics, *Journal of Geophysical Research*, **77**, 901–925. https://doi.org/10.1029/JB077i005p00901

Pollitz, F. F., Pichon, X. Le, Lallemant, S. J. (1996). Shear partitioning near the central Japan triple junction: The 1923 Great Kanto earthquake revisited: II, *Geophysical Journal International*, **126**, 882–892. https://doi.org/10.1111/j.1365-246X.1996.tb04710.x

Ramsey, C.B., Lee, S. (2013). Recent and planned developments of the program Oxcal. *Radiocarbon*, **55**, 720–730. https://doi.org/10.2458/azu_js_rc.55.16215

Reimer, P.J., Bard, E., Bayliss, A., Beck, J.W., Blackwell, P.G., Ramsey, C.B., et al. (2013). Int-cal13 and Marine13 radiocarbon age calibration curves 0–50,000 years cal BP. *Radiocarbon*, **55**, 1869–1887. https://doi.org/10.2458/azu_js_rc.55.16947

Romanet, P., Sato, D. S. K., Ando, R. (2020). Curvature, a mechanical link between the geometrical complexities of a fault: application to bends, kinks and rough faults. *Geophysical Journal International*, **223**, 211–232. https://doi: 10.1093/gji/ggaa308

Sagiya, T. (2004). Interplate coupling in the Kanto District, central Japan, and the Boso Silent earthquake in May 1996, *Pure and Applied Geophysics*, **161**, 11-12, 2601-2616. https://doi.org/10.1007/s00024-004-2566-6

Satake, K., Shishikura, M., Namegaya, Y., Fuji, R. Takeuchi, H. (2008). Fault models of the Genroku (1703) Kanto Earthquake and Tsunami along the eastern coast of Boso Peninsula, *Historical Earthquakes (Rekishi Jishin)*, **23**, 81-90, (in Japanese with English abstract).

Sato, H., Ichihara, M. (1971). On the Rivision Triangulation after the Great Kanto Earthquake, *Journal of Geodetic Society of Japan*, **17**, 178–186, (in Japanese with English abstract and figure captions) https://doi.org/10.11366/sokuchi1954.17.178

Sato, T., Matsu'ura, M. (1988) A kinematic model for deformation of the lithosphere at subduction zones, *Journal of Geophysical Research*, **93**, 6410–6418. https://doi.org/10.1029/JB093iB06p06410

Sato, H., Hirata, N., Koketsu, K., Okaya, D., Abe, S., Kobayashi, R., et al. (2005). Earthquake source fault beneath Tokyo. *Science*, **309**, 462–464. DOI: 10.1126/science.1110489

Sato, T., Higuchi, H., Miyauchi, T., Endo, K., Tsumura, N., Ito, T., et al. (2016). The source model and recurrence interval of Genroku-type Kanto earthquakes estimated from paleo-shoreline data. *Earth, Planets and Space*, **68**, 1–17. https://doi.org/10.1186/s40623-016-0395-3

Savage, J. C. (1983). A dislocation model of strain accumulation and release at a subduction zone. *Journal of Geophysical Research*, **88**, 4984–4996. https://doi.org/10.1029/JB088iB06p04984

Savage, J. C. (1995), Interseismic uplift at the Nankai subduction zone, southwest Japan, 1951 – 1990, *Journal of Geophysical Research*, **100**, 6339–6350, doi:10.1029/95JB00242

Savage, J. C. (1998), Displacement field for an edge dislocation in a layered half-space, *Journal of Geophysical Research*, **103**, 2439–2446, doi:10.1029/97JB02562

Scholz, C. (2019). The Mechanics of Earthquakes and Faulting (3rd ed.). Cambridge: Cambridge University Press. doi:10.1017/9781316681473

Scott, A.T., Pinter, N. (2003). Extraction of coastal terraces and shoreline-angle elevations from digital terrain models, Santa Cruz and Anacapa Islands, California. *Physical Geography*, **24**, 271–294. https://doi.org/10.2747/0272-3646.24.4.271

Shikakura, Y., Fukahata, Y., Matsu'ura, M. (2012). Spatial relationship between topography and rock uplift patterns in asymmetric mountain ranges based on a stream erosion model. *Geomorphology*, **138**, 162–170. https://doi.org/10.1016/j.geomorph.2011.09.002

Shimazaki, K., Nakata, T. (1980). Time-predictable recurrence model for large earthquakes. *Geophysical Research Letters*, **7**, 279–282. https://doi.org/10.1029/GL007i004p00279

Shimazaki, K., Kim, H. Y., Chiba, T., Satake, K. (2011). Geological evidence of recurrent great Kanto earthquakes at the Miura Peninsula, Japan, *Journal of Geophysical Research*, **116**, B12408, http://doi:10.1029/2011JB008639

References
_____

Shimpson, R.W., Thatcher, W., Savage, J.C. (2012). Using cluster analysis to organize and explore regional GPS velocities. *Geophysical Research Letters*, **39**, L18307, doi:10.1029/2012GL052755

Shishikuira, M. (1999). Holocene marine terraces and seismic crustal movements in Hota lowland in the southern part of the Boso Peninsula, central Japan, *The Quaternary Research (Daiyonki-Kenkyu)*, **38**, 17-28, (in Japanese with English abstract). https://doi.org/10.4116/jaqua.38.17

Shishikura, M. (2000). Coseismic vertical displacement in the Boso Peninsula during the 1703 Genroku Kanto Earthquake, deduced from emerged shoreline topography. *Historical Earthquakes (Rekishi Jishin)*, **16**, 113-122. (in Japanese with English abstract).

Shishikuira, M. (2001). Crustal movements in the Boso Peninsula, analyzing the height distribution of Holocene highest paleo-shoreline, *Annual Report on Active Fault and Paleoearthquake Researches*, **1**, 273-285, (in Japanese with English abstract and figure captions).

Shishikura, M. and Echigo, T. (2001). Coseismic vertical displacement during the 1703 Genroku Kanto earthquake in the southern part of the Miura Peninsula, analyzing height distribution of emerged wave-cut benches and fossilized sessile assemblages, *Historical Earthquakes (Rekishi Jishin)*, **17**, 32-38, (in Japanese with English abstract).

Shishikura, M., Miyauchi, T. (2001). Holocene geomorphic development related to seismotectonics in coastal lowlands of the Boso Peninsula, Central Japan. *The Quaternary Research (Daiyonki-Kenkyu),* **40**, 235–242. https://doi.org/10.4116/jaqua.40.235

Shishikura, M., Haraguchi, T., Miyauchi, T. (2001). Timing and recurrence interval of the Taisho-type Kanto Earthquake, analyzing Holocene emerged shoreline topography in the Iwai Lowland, the southwestern part of the Boso Peninsula, central Japan, *Zishin 2*, **53**, 357-372, (in Japanese with English abstract and figure captions). https://doi.org/10.4294/zisin1948.53.4_357

Shishikura, M. (2003). Cycle of interplate earthquake along the Sagami Trough, deduced from tectonic geomorphology, *Bulletin of Earthquake Research Institute, the University of Tokyo*, **78**, 245-254. http://hdl.handle.net/2261/5749

Shishikura, M., Kamataki, T., Takada, K., Suzuki, K., Okamura, Y. (2005). Survey report of emerged beach ridges in the southwestern part of Boso Peninsula - Timing of the Taisho-type Kanto earthquake. *Annual report on active fault and paleoearthquake researches*, **5**, 51–68, (in Japanese with English abstract and figure captions).

Shishikura, M., Echigo, T., Kaneda, H. (2007). Marine reservoir correction for the Pacific coast of central Japan using C-14 ages of marine mollusks uplifted during historical earthquakes. *Quaternary Research*. **67**, 286–291. https://doi.org/10.1016/j.yqres.2006.09.003

Shishikura, M. (2014). History of the paleo-earthquakes along the Sagami Trough, central Japan: Review of coastal paleo-seismological studies in the Kanto region.

Episodes, **37**, 246–257. https://doi.org/10.18814/epiiugs/2014/v37i4/004

Shishikura, M., Fujiwara, O., Namegaya, Y., Matsumoto, D. (2014a). Study of subduction zone paleoearthquakes. *Geological Survey of Japan Interim Report*. **65**, 111–131 (in Japanese with English abstract and figure captions).

Shishikura, M., Namegaya, Y., Ono, N., Kanda, H. (2014b). Detailed topographic measurement and ^{14}C dating for the marine terraces in the Kenbutsu coast, the southern part of the Boso Peninsula, central Japan. *Annual report on active fault and paleoearthquake researches*, **14**, 1–38, (in Japanese with English abstract and figure captions).

Shyu, J.B.H., Wang, C.-C., Wang, Y., Shen, C.-C., Chiang, H.-W., Liu, S.-C., et al. (2018). Upper-plate splay fault earthquakes along the Arakan subduction belt recorded by uplifted coral microatolls on northern Ramree Island, western Myanmar (Burma). *Earth and Planetary Science Letters*, **484**, 241-252. https://doi.org/10.1016/j.epsl.2017.12.033

Sieh, K.E., Jahns, R.H. (1984). Holocene activity of the San Andreas fault at Wallace Creek, California. *Geological Society of America Bulletin*, **95**, 883–896. https://doi.org/10.1130/0016-7606(1984)95<883:HAOTSA>2.0.CO;2

Sieh, K., Ward, S.N., Natawidjaja, D., Suwargadi, B.W. (1999). Crustal deformation at the Sumatran Subduction Zone revealed by coral rings. *Geophysical Research Letters*, **26**, 3141-3144. 10.1029/1999gl005409

Stuiver, M., Braziunas, T. F. (1993). Modeling atmospheric 14 C influences and 14 C ages of marine samples to 10,000 BC. *Radiocarbon*, **35**, 137-189. https://doi.org/10.1017/S0033822200013874

Sugimura, A., Naruse, Y. (1954). Changes in sea level, seismic upheavals, and terraces in the southern Kanto region, Japan (I). *Japanese journal of geology and geography*, **24**, 101–113.

Sugimura, A., Naruse, Y. (1955). Changes in sea level, seismic upheavals, and terraces in the southern Kanto region, Japan (II). *Japanese journal of geology and geography*, **26**, 165–176.

Sun, T., Saffer, D., Ellis, S. (2020). Mechanical and hydrological effects of seamount subduction on megathrust stress and slip, *Nature Geoscience*, **13**, 249–255, https://doi.org/10.1038/s41561-020-0542-0

Suzuki, Y., Kodama, K., Mitsunashi, T. (1990). Geology of the Nago district. With Geological Sheet Map at 1 : 50,000, Geological Survey of Japan. (in Japanese with English abstract)

Takada, K., Nakata, T., Miyagi, T., Haraguchi, T., Nishitani, Y. (2002). Handy Geoslicer–New soil sampler for Quaternary geologist, *Chishitsu News*, **579**, 12–18 (in Japanese).

Takahashi, A., Hashimoto, M., Hu, J.-C., Takeuchi, K., Tsai, M.-C., & Fukahata, Y. (2019). Hierarchical cluster analysis of dense GPS data and examination of the nature of the clusters associated with regional tectonics in Taiwan. *Journal of Geophysical Research: Solid Earth*, **124**, 5174– 5191. https://doi.org/10.1029/2018JB016995

Takemura, M. (1994). Aftershock activities for two days after the 1923 Kanto earthquake (M=7.9) inferred from seismograms at Gifu Observatory, *Zisin 2*, **46**, 439–455. (in Japanese with English abstract). https://doi.org/10.4294/zisin1948.46.4_439

Takemura, M., Ikeura, T. (1994a). Strong motion records from the 1923 Kanto earthquake observed at the Gifu Observatory, *Zishin 2*, **47**, 193–200, https://doi.org/10.4294/zisin1948.47.2_193

Takemura, M., Ikeura, T. (1994b) Source characteristics of the 1923 Kanto earthquake as deduced from data in short-period range -Interpretation of personal experiences, and a short-period seismogram-, *Zishin 2*, **47**, 351–364, https://doi.org/10.4294/zisin1948.47.4_351

Thatcher, W. (1984). The earthquake deformation cycle at the Nankai Trough, southwest Japan. *Journal of Geophysical Research: Solid Earth*, **89**, 3087–3101., https://doi.org/10.1029/JB089iB05p03087

Tibshirani, R., Walther, G., Hastie, T. (2001). Estimating the number of clusters in a data set via the gap statistic. *Journal of the Royal Statistical Society*, **B. 63**, 411–423. https://doi.org/10.1111/1467-9868.00293

Trenhaile, A. (2000). Modeling the development of wave-cut shore platforms. *Marine Geology*, **166**, 163–178. https://doi.org/10.1016/S0025-3227(00)00013-X

Tsumura, N., Komada, N., Sano, J., Kikuchi, S., Yamamoto, S., Ito, T., et al. (2009). A bump on the upper surface of the Philippine Sea plate beneath the Boso Peninsula, Japan inferred from seismic reflection surveys: A possible asperity of the 1703 Genroku earthquake. *Tectonophysics*, **472**, 39–50. https://doi.org/10.1016/j.tecto.2008.05.009

Uesawa, S., Miyakawa, A. (2015). A recursion model to calculate the original widths of narrow terraces and their backwearing rates in a coastal area subjected to regular uplift during the late Holocene. *Geomorphology*, **246**, 407-412. https://doi.org/10.1016/j.geomorph.2015.06.042

Uno, T., Miyauchi, T., Shishikura, M. (2007). Reexamination of earthquakes occurring along the Sagami Trough, analyzed by Holocene marine terraces in the Boso Peninsula. *In: Japan Geoscience Union Meeting, 2007.*S141-007.

Usami, T., Ishi, H., Imamura, T., Takemura, M., Matsuura, R. (2013). Materials for comprehensive list of destructive earthquakes in Japan. Univ. Tokyo Press (in Japanese).

Wald, D. J., Somerville, P. G. (1995). Variable-slip rupture model of the Great 1923 Kanto, Japan, earthquake: Geodetic and body-waveform analysis, *Bulletin of Seismological Society of America*, **85**, 159–177.

Wang, R. (2005), The dislocation theory: A consistent way for including the gravity effect in (visco)elastic plane-earth models, *Geophysical Journal International*, **161**, 191– 196, doi:10.1111/j.1365-246X.2005.02614.x

Wang, K., Bilek, S. L. (2011). Do subducting seamounts generate or stop large earthquakes? *Geology*, **39**, 819–822. http://doi:10.1130/G31856.1

Wang, Y., Shyu, J.B.H., Sieh, K., Chiang, H.-W., Wang, C.-C., Aung, T., et al. (2013). Permanent upper plate deformation in western Myanmar during the great 1762 earthquake: Implications for neotectonic behavior of the northern Sunda megathrust. *Journal of Geophysical Research: Solid Earth*, **118**, 1277-1303. 10.1002/jgrb.50121

Watanabe, A. (1929). Preliminary Note on the Coastal Terraces of the Southern Parts of Bôsô Peninsula, *Geographical review of Japan*, **5**, 119–126. https://doi.org/10.4157/grj.5.119

Yamasaki, N. (1926). Physiographical studies of the great earthquake of Kwanto district, 1923. *Journal of Faculty of Science, Imperial University of Tokyo, Section II*, **2**, 77-119. (in Japanese).

Yanagisawa, H., Goto, K. (2017) Source model of the 1703 Genroku Kanto earthquake tsunami based on historical documents and numerical simulations: modeling of an offshore fault along the Sagami Trough. *Earth Planets, and Space*, **69**, 136. https://doi.org/10.1186/s40623-017-0713-4

Yokota, K. (1978). Holocene coastal terraces on the southern coast of the Boso Peninsula, *Geographical Review of Japan, Series A*, **51**, 349-364, (in Japanese with English abstract). https://doi.org/10.4157/grj.51.349

Yokota, H., Kataoka, S., Tanaka, T., Yoshizawa, S. (1989). Estimation of long-period ground motion of the 1923 great Kanto earthquake, *Journal of Structure and Construction Engineering*, (Transactions of the Architectural Institute of Japan), **401**, 35–45. (in Japanese). https://doi.org/10.3130/aijsx.401.0_35

Yokoyama, Y., Koizumi, M., Matsuzaki, H., Miyairi, Y., & Ohkouchi, N. (2010). Developing ultra small-scale radiocarbon sample measurement at the University of Tokyo. *Radiocarbon*, **52**, 310-318. https://doi.org/10.1017/S0033822200045355

Yonekura, N. (1975). Quaternary tectonic movements in the outer arc of Southwest Japan with special reference to seismic crustal deformation, *Bulletin of the Department of Geography, University of Tokyo*, **7**, 19-71.